



**FACULTY  
OF MATHEMATICS  
AND PHYSICS**  
Charles University

## **DOCTORAL THESIS**

Mykhailo Vaidulych

### **Plasma Treatment of Porous Structures**

Department of Macromolecular Physics

Supervisor of the doctoral thesis: Prof. Assist. Jan Hanuš, PhD

Study programme: Physics

Specialization: Biophysics, Chemical and Macromolecular Physics

Prague 2019

I declare that I carried out this doctoral thesis independently, and only with the cited sources, literature and other professional sources.

I understand that my work relates to the rights and obligations under the Act No. 121/2000 Coll., the Copyright Act, as amended, in particular the fact that the Charles University has the right to conclude a license agreement on the use of this work as a school work pursuant to Section 60 paragraph 1 of the Copyright Act.

In..... date.....

signature

## Acknowledgments

I would like to express my gratitude to colleagues and friends who helped and supported me during my Ph.D. study. I am grateful to my supervisor Dr. Jan Hanuš for his willingness to help, useful advice and support with the experimental activity and data interpretation. Special thanks to Doc. Ondřej Kylián, Doc. Andrei Choukourov, Doc. Danka Slavínská, Prof. Hynek Biederman for sharing valuable knowledge. I am thankful to my colleagues Dr. Jaroslav Kousal, Dr. Pavel Solař, Dr. Anna Kuzminova, Dr. Artem Ryabov, Mgr. Marcela Búryová, Dr. Iurii Melnichuk for advice and support in various aspects of scientific activity. I would like to thank my colleagues Ph.D. students Mgr. Daniil Nikitin, Mgr. Pavel Pleskunov, Mgr. Renata Tafiichuck, Mgr. Suren Ali-Ogly, Mgr. Jiří Kratochvíl for their help and an excellent working atmosphere.

I am thankful to Dr. Kiyoshi Kobayashi and Dr. Tohru Suzuki who provided me with all the necessary information and support during my stay as a host researcher in the Ceramics Processing Group at NIMS, Japan.

Also, I would like to thank Dr. Ivan Khalakhan for help and flexibility with SEM measurements. I am grateful to Dr. Artem Shelemin for motivation and useful discussions. My thanks to Dr. Mykhailo Vorokhta who inspired me to fall in this world of continues discovery – physics.

**Title:** Plasma treatment of porous structures

**Author:** Mykhailo Vaidulych

**Department / Institute:** Department of Macromolecular Physics

**Supervisor of the doctoral thesis:** Prof. Assist. Jan Hanuš, Ph.D., Department of Macromolecular Physics

**Abstract:** The thesis is focused on the implementation of low-temperature plasma for the modification of porous materials. Two main strategies are involved: functionalization through the deposition of functional nanocomposite coatings and low-pressure plasma etching. In the first case, a gas-phase step-by-step deposition process based on the combination of deposition of nanoparticles and thin films was developed to obtain super-wettable nanocomposite coatings on filtration membranes. It was shown that the deposition parameters of thin films and particles of plasma polymer can tune the wetting characteristic of the membranes whereas embedding copper nanoparticles endows them with antibacterial properties. As a result, highly efficient superhydrophobic/superoleophilic and smart superamphiphilic membranes were successfully fabricated for oil/water separation.

Plasma processing in the atmosphere of argon, oxygen or nitrogen was utilized to modify hard metal/polymer nanocomposites (Ag/a-C:H) with potential to be used as functional coatings for bone implants. An anisotropic etching resulted in an exposure of higher amount of the metal NPs initially buried beneath the surface. This allows to enhance the short term antibacterial efficiency and preserve mechanical properties of the produced coatings.

As a part of the study, fundamental aspects of the formation of metallic NPs by GAS and thin films deposition by PECVD were studied.

**Keywords:** plasma treatment, nanocomposite coatings, filtration membranes, antibacterial properties, nanoparticles

**Název práce:** Plazmové opracování porézních povrchů

**Autor:** Mykhailo Vaidulych

**Katedra:** Katedra makromolekulární fyziky

**Vedoucí doktorské práce:** Prof. Assist. Jan Hanuš, Ph.D., Katedra makromolekulární fyziky

**Abstrakt:** Disertační práce je zaměřena na modifikaci porézních materiálů pomocí nízkoteplotního plazmatu. V rámci této práce jsou studovány dva hlavní přístupy: funkcionalizace prostřednictvím nanášení funkčních nanokompozitních vrstev a nízkotlaké plazmové leptání. V prvním případě bylo využito střídavé depozice tenkých vrstev z plynné fáze a nanášení nanočástic. Tak byly připraveny nanokompozitní vrstvy na filtračních membránách, které mají extrémní rozsah smáčivosti. Bylo ukázáno, že depoziční parametry tenkých vrstev a polymerních nanočástic umožňují upravit smáčivost membrán, zatímco zabudování měděných nanočástic jim poskytuje antibakteriální vlastnosti. Výsledkem byla úspěšná příprava vysoce efektivních superhydrofobních/superoleofilních a chytrých superamphiphilních membrán, které byly použity pro separaci směsi olej/voda.

Plazmové opracování v atmosféře argonu, kyslíku nebo dusíku bylo použito k úpravě tvrdých nanokompozitů kov/polymer (Ag/a-C: H) s potenciálem využití jako funkční povlaky pro kostní implantáty. Anizotropní leptání vede k expozici většího množství kovových nanočástic původně zabudovaných pod povrchem. Toto umožňuje zvýšit krátkodobou antibakteriální účinnost a zachovat mechanické vlastnosti nanášených povlaků.

V rámci práce byly také studovány základní aspekty tvorby kovových nanočástic pomocí GAS a depozice tenkých vrstev pomocí PECVD.

**Klíčová slova:** plazmové opracování, nanokompozitní povlaky, filtrační membrány, antibakteriální vlastnosti, nanočástice

## **Aims of the Doctoral Thesis**

The main goal of the thesis is the development and implementation of low-temperature plasma-based methods for the modification of porous substrates with the specific focus on applications in the field of wastewater purification and biomedicine.

The main objectives of the thesis include the following topics:

- Study the fundamental aspects of the thin films deposition by PECVD and formation and growth of the metallic NPs by GAS for the fabrication of metal/polymer nanocomposite coatings.
- Development of multifunctional nanocomposite coatings with the wettability ranging from superhydrophilic to superhydrophobic.
- Study the effect of plasma etching on metal/polymer nanocomposites, their chemical composition, structure and antibacterial characteristics.
- Implementation of super-wettable nanocomposites on the porous textiles with potential to be used in the field of waste (oily) water purification and biomedicine.

# Contents

<b>Acknowledgments</b> .....	iii
<b>Aims of the Doctoral Thesis</b> .....	vi
<b>1. Introduction</b> .....	1
1.1. <i>Porous materials &amp; plasma treatment</i> .....	1
<b>2. Background</b> .....	3
2.1. <i>Plasma</i> .....	3
2.2. <i>Plasma processing</i> .....	11
2.2.1. Physical etching.....	11
2.2.2. Reactive ion etching (RIE).....	12
2.3. <i>Coating deposition</i> .....	13
2.3.1. Sputtering deposition.....	14
2.3.2. Magnetron sputtering.....	15
2.3.3. Plasma-enhanced CVD (PECVD).....	16
2.4. <i>Nanoparticles fabrication by gas aggregation source</i> .....	19
2.5. <i>Nanocomposite films</i> .....	22
2.6. <i>Application perspectives</i> .....	25
2.6.1. Water purification from non-polar organic contaminants.....	25
2.6.2. Biomedical applications.....	27
<b>3. Experimental techniques</b> .....	28
3.1. <i>Deposition techniques and plasma treatment</i> .....	28
3.1.1. Deposition of plasma polymer thin films.....	28
3.1.2. Plasma etching.....	29
3.1.3. Gas Aggregation Source (GAS) of nanoparticles.....	30
3.1.4. Fabrication of functional nanocomposite coatings.....	32
3.2. <i>Characterization methods</i> .....	34
3.2.1. Quartz Crystal Microbalance (QCM).....	34

3.2.2.	Optical Emission Spectroscopy (OES).....	35
3.2.3.	Atomic Force Microscopy (AFM).....	36
3.2.4.	Scanning Electron Microscopy (SEM).....	38
3.2.5.	Transmission Electron Microscopy (TEM).....	41
3.2.6.	X-Ray Photoelectron Spectroscopy (XPS).....	42
3.2.7.	Fourier Transformer Infrared spectroscopy (FTIR) .....	44
3.2.8.	Ultraviolet-Visible Spectrophotometry (UV–Vis) .....	45
3.2.9.	Spectroscopic Ellipsometry .....	46
3.2.10.	Measurements of wettability .....	47
3.2.11.	Antibacterial properties .....	50
3.3.	<b><i>Oil/water separation</i></b> .....	51
3.3.1.	Materials .....	51
3.3.2.	Selective absorption.....	51
3.3.3.	Separation of water/oil mixture .....	52
4.	<b>Results and Discussion</b> .....	53
4.1.	<b><i>Optimization of the deposition process of Cu NPs.</i></b> .....	53
4.1.1.	Magnetic field optimization.....	54
4.1.2.	Deposition rate and size distribution of nanoparticles.....	55
4.1.3.	Shape of the nanoparticles .....	66
4.2.	<b><i>Deposition of Ag/a-C:H nanocomposite coatings with surface enrichment</i></b> .....	68
4.2.1.	Ag/a-C:H nanocomposites.....	68
4.2.2.	Plasma etching for Ag surface enrichment of nanocomposites.	76
4.2.3.	Antibacterial activity of Ag/a-C:H nanocomposites.....	80
4.3.	<b><i>Functional nanocomposite coatings for facile oil/water separation and biomedical applications.</i></b> .....	81
4.3.1.	Thin film deposition and nanoparticles fabrication.....	82

4.3.2.	Fabrication of the super- hydrophobic/amphiphilic membranes	84
4.3.3.	Selective absorption.....	90
4.3.4.	Switchable separation.....	93
4.3.5.	Antibacterial activity of filtration membranes.....	97
4.4.	<b><i>Interlanthanide perovskites</i></b> .....	99
4.4.1.	LSYO perovskites.....	99
5.	<b>Conclusions</b> .....	102
	<b>Bibliography</b> .....	105
	<b>List of Abbreviations</b> .....	112
	<b>List of Publications</b> .....	113

# 1. Introduction

## 1.1. Porous materials & plasma treatment

The porous material is a medium containing regular pores or voids in its structure. The skeletal part consists of an organic or inorganic solid framework supporting a porous structure and is often called “matrix”. The pores are normally filled with a fluid that could be either gas or liquid. In general, porous materials could be characterized by low weight, high surface to volume ratio, good mechanical properties, enhance transport and diffusion capabilities, good permeability, etc. The functional characteristics of such materials are strongly dependent on the development of their porous structure. Hence, the basic parameters for porous materials are related to the pores such as porosity, specific surface area, pores size, shape and morphology [1].

According to International Union of Pure and Applied Chemistry (IUPAC), porous materials could be classified into 3 main types regarding pore size: microporous ( $d < 2$  nm), mesoporous ( $2 < d < 50$  nm) and macroporous with pore size above 50 nm [2]. Typical examples of microporous materials include natural zeolites and metal-organic frameworks; mesoporous materials are presented by different kinds of silica, alumina, activated carbon, etc.; and popular examples of macroporous materials are textiles, paper, etc. Attractive bulk characteristics determine a widespread use of such materials in various fields, including catalysis, chemical energy conversion, photocatalytic hydrogen production, hydrogen storage, medicine, sorption, sensing, photovoltaics as well as in everyday life [3].

Obviously, porous materials provide a facile and low-cost solution for potential applications. However, it often happens that the surface characteristics of the material should be properly optimized before use. Within the last decade, a number of approaches have been established to modify surface chemistry, micro- and nano-architecture or wettability of porous materials [4]. Among many others, methods based on the low-temperature low-pressure plasma discharge such as plasma etching (PE), plasma-enhanced chemical vapor deposition (PECVD), physical vapor deposition (PVD) were extensively studied. In comparison with conventional approaches, these methods provide several advantages. First, plasma can penetrate deeply into the

structure of the material, modify it, and at the same time preserve the bulk characteristics. Second, plasma processing/deposition is almost independent on the type of substrate, thus different types of materials could be modified. Third, plasma-based methods could be easily adjusted by tailoring a wide range of process parameters such as power, pressure, working gas mixture, etc. Forth, low-pressure plasma processing is an environmentally friendly approach with low consumption of materials and a minimal exhaust of by-products. Moreover, compatibility with other vacuum-based techniques makes it easier to implement plasma methods into the already established technological processes. For example, thin film deposition by PECVD in combination with Gas Aggregation Source (GAS) of nanoparticles provides a flexible solution for the production of nanostructured and nanocomposite functional materials [5,6].

At the Department of Macromolecular Physics of Charles University, the study and development of the plasma processes date back to the 80<sup>th</sup> of the last century. A great deal of work was done in the field of coatings deposition and NPs fabrication [7–13]. In this thesis, the Author studied new perspectives of plasma-based methods for the fabrication of multifunctional nanocomposite coatings and modification of porous substrates with the specific focus on application in the field of wastewater purification and biomedicine. The thesis covers the following topics:

- *Deposition processes.* The fundamental aspects of the thin films (hydrocarbon, organosilicon) deposition, the formation and growth of the metallic NPs by GAS, and the fabrication of functional nanocomposites were investigated.
- *Surface enrichment by plasma etching.* Plasma treatment in the atmosphere of oxygen or nitrogen was utilized for plasma processing of metal/polymer nanocomposites.
- *Wettability control.* The step-by-step deposition process was used for the fabrication of nanostructured coatings with the wettability ranging from superhydrophilic to superhydrophobic.
- *Filtration membranes.* Super-wettable nanocomposite coatings were deposited on porous textiles (viscose fabric or carbon fabric) and then used as filtration membranes for water/oil separation.

## 2. Background

### 2.1. Plasma

Plasma is the fourth state of matter – an ionized gas consisting of a mixture of electrons, ions, neutral atoms and radicals, photons. Ionized gas is usually called plasma when it is electrically neutral or quasineutral. The first mention of this phenomenon dates back to 1927 when Irving Langmuir wrote:

*“...the ionized gas contains ions and electrons in about equal numbers so that the resultant space charge is very small. We shall use the name plasma to describe this region containing balanced charges of ions and electrons.”* [14]

Based on the relative temperatures of the plasma species, one can be classified as thermal (equilibrium) or non-thermal (non-equilibrium) plasma [15,16]. A thermal plasma is a plasma in thermodynamic equilibrium when electrons temperature balance with the temperature of heavy species ( $T_{electrons} = T_{ions} = T_{gas}$ ). The degree of ionization in such a plasma is high or full, and the temperature of electrons and ions can reach  $10^4$  eV (fusion reactors, star cores, etc.). An object inserted into the thermal plasma undergoes an intense bombardment with the highly-energetic species. This can lead to various effects such as the bond breaking, degradation or complete destruction of the material. In fact, thermal plasma is not suitable for the treatment of temperature sensitive materials (polymers, etc.). In non-thermal or non-equilibrium plasma electrons temperature could reach several eV ( $\sim 10^4$  K), while ions and neutrals remain at ambient temperature ( $T_{electrons} \gg T_{ions} = T_{gas}$ ). In this case, the degree of plasma ionization is small, typically 1 charge carrier per  $10^6$  neutrals. Usually, such a plasma is used for non-destructive processing of materials, what is the main focus of this work.

In non-thermal plasma, the predominant carriers of negative charge are electrons and carriers of the positive charge are ions. In the electric field, electrons gain energy much faster than ions, at least on a factor of  $\sqrt{m_i/m_e}$ , where  $m_i$  and  $m_e$  are the mass of ion and electron respectively. Such electrons undergo various collisions with plasma species delivering energy for ionization, excitation or other plasma

processes. The probability that a given type of collision will occur under given conditions is known as a collision cross section ( $\sigma$ ). In the case of elastic collisions  $\sigma$  could be define as  $\pi(r_A + r_B)^2$ , where  $r_A$  and  $r_B$  are the radii of the particle A and B respectively. For inelastic collisions, the total cross-section  $\sigma_{total}$  is define as a sum of individual cross-section constituents involved in the collision such as elastic  $\sigma_{el}$ , excitation  $\sigma_{ex}$ , ionization  $\sigma_{ion}$  etc.:

$$\sigma_{total} = \sigma_{el} + \sigma_{ex} + \sigma_{ion} \quad (1)$$

The average distance traveled by the particle A between the collisions with particle B is known as the mean free path  $\lambda_B$  and can be defined as follows:

$$\lambda_B = \frac{1}{n_B \sigma} \quad (2)$$

where  $n_B$  is the number density of the particles B,  $\sigma$  is the collision cross-section.

Another important parameter is the interaction or collision frequency  $\nu_B$ . In the case of electron/heavy particle interaction, the heavy particle are assumed to be immobile and  $\nu_B$  can be calculated as the product of the average velocity of electrons ( $v_e$ ) to the inverse mean free path  $\lambda_B$ :

$$\nu_B = n_B \sigma v_e \quad (3)$$

Plasma is characterized by a collective behavior that is given by the attractive and repelling forces between the charged species. Thus a charge introduced into the plasma induces polarization of the plasma and the charge separation occurs. The length which characterizes electrical screening of Coulomb potential is called Debye length ( $\Lambda_D$ ) and can be calculated as follows:

$$\Lambda_D = \left( \frac{\epsilon_0 k_B T_e}{n_e q e^2} \right)^{\frac{1}{2}} \quad (4)$$

where  $\epsilon_0$  is the permittivity of free space,  $k_B$  - the Boltzmann's constant,  $T_e$  - the temperature of the electrons,  $n_e$  - the density of electrons,  $q_e$  - the charge of an electron.

When electrons gain energy in electrostatic interactions, one can be easily triggered from its steady state and the charge imbalance on the scale of the Debye length occurs. Since the interaction between electrons is strong this leads to the rapid oscillation of the electron density at a frequency known as plasma frequency:

$$\omega = \left( \frac{n_e q_e^2}{\epsilon_0 m_e} \right)^{\frac{1}{2}} \quad (5)$$

An example of non-thermal plasma is a glow discharge in a low-pressure environment. Typically, a bell type reactor with two parallel electrodes is used. The air within the chamber is evacuated to high or ultra-high vacuum and then working gas is fed into the chamber at low pressure (0.01 – 10 Pa). The charge carriers are generated through the gas ionization when the potential difference between two electrodes is applied. A minimum voltage necessary to ignite self-sustained discharge is called breakdown voltage. Current-voltage characteristic of electric-breakdown is presented in Figure 1. In the dark region under a low voltage, the number of free charged carriers is low and no or little glow can be observed. When the voltage reaches or exceeds a breakdown voltage, free electrons are accelerated in the electric field gaining enough energy to freed additional electrons through the collisions with gas molecules. These electrons are accelerated as well, contributing to the ionization process. As a result, self-sustained discharge is established. The phenomenon is known as Townsend avalanche or multiplication process.

A decrease in the external resistance or increase of the electromotive force leads to a further increase in the current flow. This is accompanied by a gradual decrease of voltage until it reaches a steady state in a wide range of currents corresponding to the sub-normal and normal regions of the glow discharge. When the entire surface of the cathode is involved in the glow, abnormal glow discharge is realized and the voltage increase rapidly. In the glow discharge region, the discharge is maintained by secondary electrons predominantly generated by ions impact during

the target bombardment. Further current increase results in arc discharge, when electrons leave the cathode surface termionically.

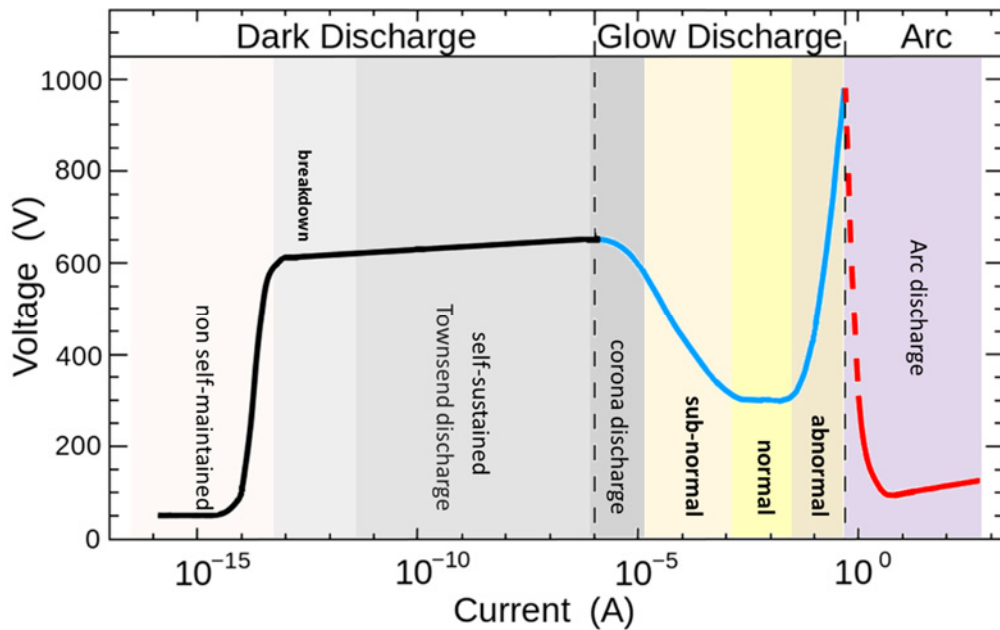


**Figure 1.** Voltage-current characteristics of electrical breakdown in neon at 133 Pa with the formation of a glow discharge.

In practice, the electric-breakdown of gas in the mentioned configuration depends on the pressure in the chamber and the inter-electrode (cathode-to-anode) distance (Figure 2). The relation between the parameters is known as a Paschen's law and can be defined experimentally [17].

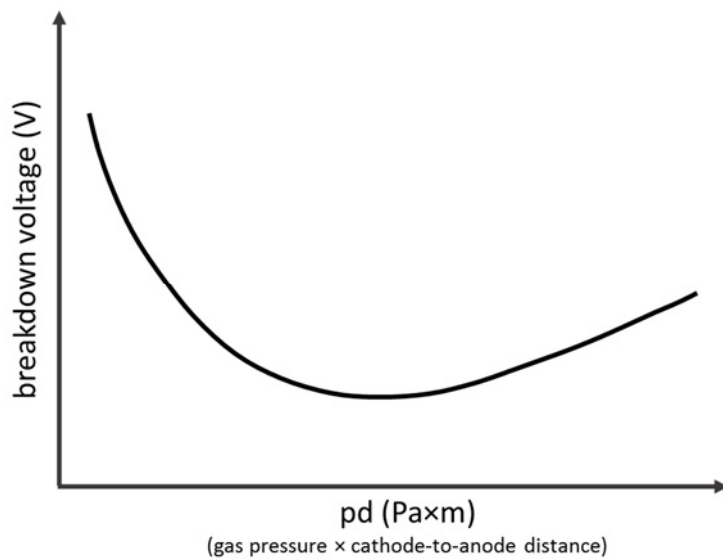


**Figure 2.** Paschen's law.

Considering a glow discharge in the glass tube, one can observe a sequence of the dark and luminous spaces along the tube (Figure 3). In general, four main regions can be defined: cathode region, negative glow region, positive column region and anode region. The cathode region plays a substantial role to provide a self-sustaining discharge. The large potential drop over the region accelerates positive ions toward the cathode surface and is responsible for the emission of secondary electrons (SE). Such SE leave the cathode surface with energies around 1 eV that is not sufficient for atoms or molecules excitation. Thus there is no light observed in the close vicinity to cathode corresponding to Aston dark space. On the way to anode, electrons gain enough energy from the electric field for electronic excitations resulting in the cathode glow space. With further acceleration in the cathode dark space, electrons impact leads to the ionization rather than excitation and the number of free electrons increase. This explains a little glow in the region. The increasing electron density leads to decrease in the electric field and deceleration of charged species. Consequently, the electrons and ions are recombined, accompanied by a bright negative glow. Subsequent distribution of positive column region and anode region is given by the excitation and recombination processes in plasma. A more detailed description of glow regions in the glow discharge can be found elsewhere [18].

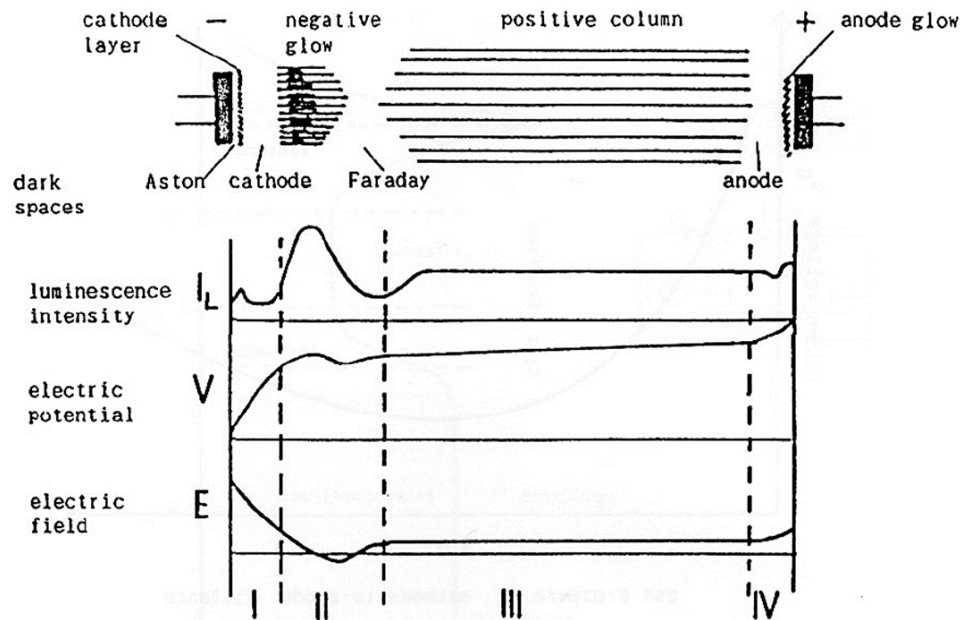


**Figure 3.** The glowing regions in the normal glow discharge (adapted from [18]).

In practice, the external power supply is used to deliver energy to atoms or molecules. Depending on the generator type, the glow discharge can be driven by direct current (DC) or alternating current (usually radio-frequency [RF]). As it was discussed, in the DC regime, the electric field accelerates positive ions towards the cathode, whereas the electrons are moving within the same field towards the anode. At this point, an important parameter is the energy of species that bombard the surface exposed to the plasma. The mechanism can be explained considering the potential distribution in a glow discharge (Figure 4). Plasma potential ( $V_p$ ) is the potential of the plasma with respect to the walls of the chamber. Since electrons escape plasma region much faster than ions, plasma potential is always several volts higher relative to the walls of the chamber. When an electrically isolated object is adjacent to plasma, the potential of the surface adjusts in such a way that the current of ions to the surface balance that of electrons. As a result, any object inserted into the plasma, established with floating potential ( $V_f$ ) that is negative with respect to the plasma. In practice, a tiny positively charge region called sheath is formed on the interface plasma/object. Normally the sheath extends over the distance of several Debye lengths where the potential drop occurs. When the pressure in the chamber is low enough, i.e. the mean free path of ions is similar or higher as compared to sheath thickness, the energy of ions bombardment of the surface corresponds to the potential drop over the sheath region.

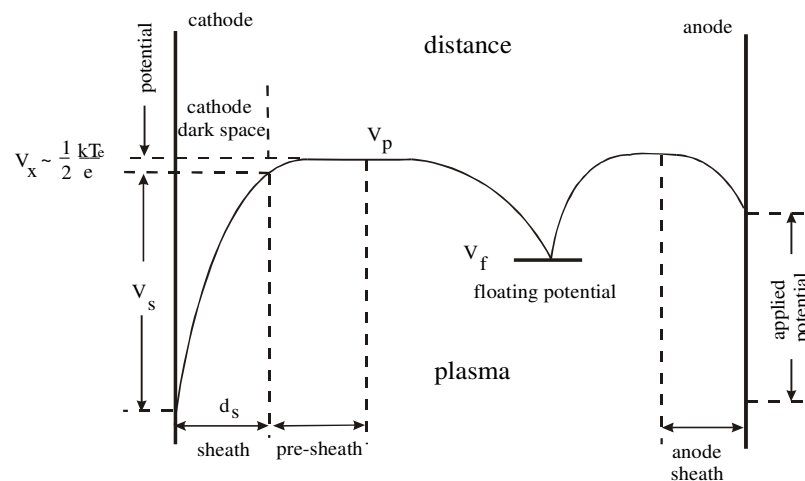


**Figure 4.** Potential variation in a real glow discharge (after Ref. [19]).

According to the above, the highest potential drop is in the cathode dark space. In the DC regime, bombardment of the cathode with the highly energetic ions leads to the knocking out atoms from the surface of the cathode. This effect is widely used in the field of sputtering deposition when the cathode is covered with material to be sputtered. Sputtering is more in detail discussed in the next sections. However, DC driven discharge is not applicable to the dielectric materials. In this case, the positive charge accumulates on the surface of non-conducting material. Latter prevents the release of secondary electrons from the cathode surface that is vital to sustain the discharge [18].

At the radio frequency discharge, the sign of the potential on the cathode and anode is alternating at a high rate (100 kHz-30 MHz). At these conditions, “heavy” ions remain almost immobile, while light electrons oscillate between the electrodes. This determines high electron and low ion currents to the electrodes during the oscillation cycle (Figure 5 left). The discharge is retained through the electron-impact ionization when electrons undergo numerous collisions with neutral molecules in the glow region. It follows, RF discharge does not depend on the processes at the electrode and one could be covered with any material (e.g. insulator).

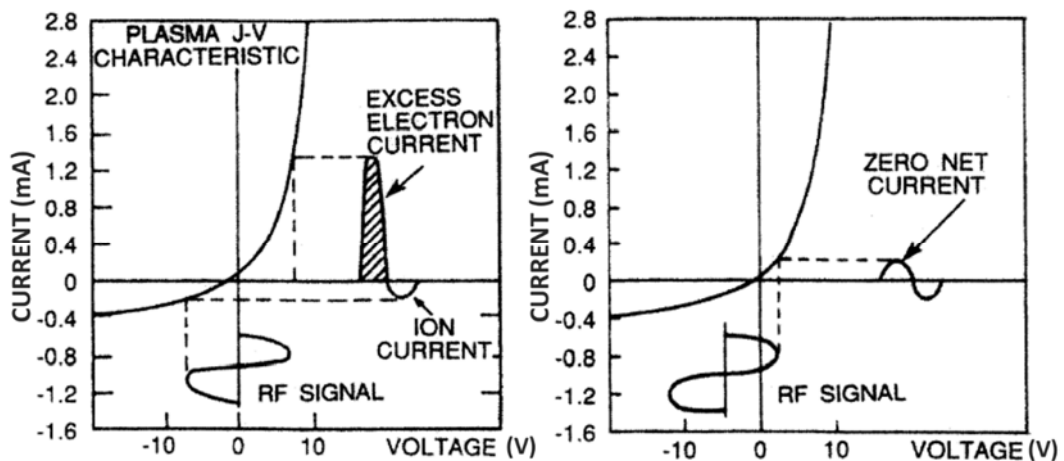


**Figure 5.** Negative self-bias formation on a capacitively coupled electrode in an RF discharge (adapted from [20])

If one of the electrodes is a capacitive coupled (through the impedance matching box) to RF power supply, a pulsing negative potential will establish on the electrode. In this case, the total flow of electrons and ions to the electrode surface is set to zero. Since the electrons possess much higher mobility in comparison to ions, the electrode is self-biased to a negative potential and the balance between electron and ion currents is achieved (Figure 5 right). The presence of the negative voltage on the electrode determines the DC-like character of the discharge, and thus RF sputtering is possible.

In RF discharge both electrodes are involved in the sputtering process. The voltage drop near each electrode depends on the area of electrodes according to the Child-Langmuir equation (Equation 6). To provide the highest voltage drop near the cathode (RF electrode) and avoid contamination from the sputtering of the anode (grounded electrode) the effective area of the electrodes should be set properly. In practice, the anode is connected to the chamber walls providing a large area, while the cathode remains relatively small.

$$\frac{V_{RF}}{V_{GND}} = \left( \frac{A_{GND}}{A_{RF}} \right)^4 \quad (6)$$

where,  $A_{GND}$  is the area of the grounded electrode,  $A_{RF}$  is the area of RF electrode,  $V_{RF}$  is the voltage drop on the RF electrode,  $V_{GND}$  – voltage drop on the grounded electrode.

## **2.2. Plasma processing.**

Any object inserted into the glow or afterglow region of the plasma experience intense bombardment with the ionized species. Such interaction usually leads to the modification of the material surface, with changes in its chemical, physical or bio-responsive properties, and is commonly known as plasma processing. Depending on the treatment conditions and desirable effects plasma processing could be separated into three main classes: physical etching or sputtering, reactive ion etching (RIE) and coating deposition [15].

### **2.2.1. Physical etching.**

Obviously, a proper selection of the working gas mixture (inert or chemically active gas, organic vapors etc.) plays a key role to obtain desirable effects during the plasma processing. Plasma discharge (DC or RF) in the atmosphere of inert gases (usually noble gases: Ar, Ne, He) leads to the physical etching or sputtering of the material. Such plasma treatment is based on the bombardment of the material with ions accelerated in the electric field. When incident ions reach the surface with the sufficient energy, the surface atoms can be ejected leading to the removal of the material exposed to the plasma (Figure 6 left). Such a process depends on the angle of incidence of ion, thus physical etching is anisotropic. The number of atoms sputtered per incident ion is called a sputtering yield. The parameter strongly depends on the energy and mass of the incident ions and is one of the main characteristics of etching (sputtering) process.

Since the non-reactive gases do not undergo chemical reactions, the physical etching is primarily used for the surface cleaning and sputtering of the material. However, some other effects can be achieved, e.g. the Ar etching can improve the wettability of the surface by the removal of fatty hydrophobic layers [21,22].

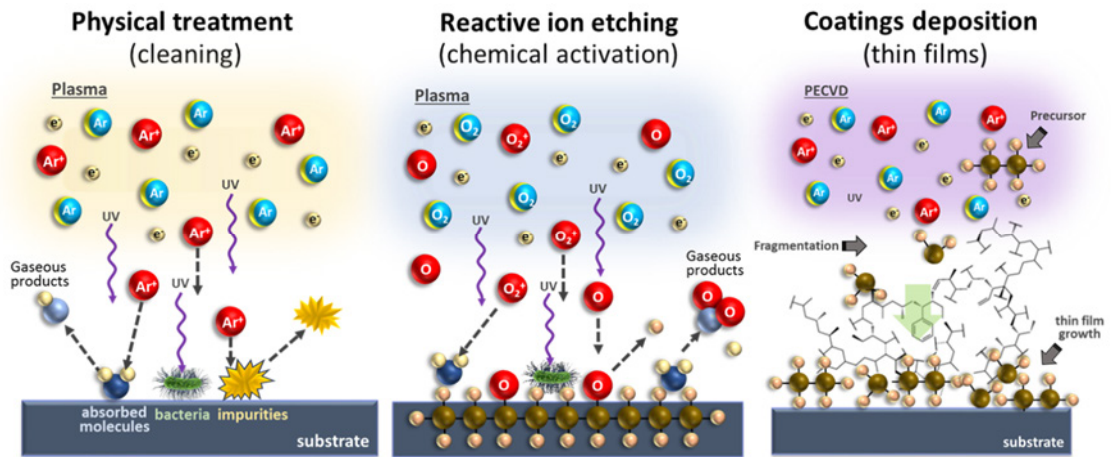


**Figure 6.** Schematic representation of the three types of plasma processing: physical etching (left), reactive ion etching (center) and coating deposition (right).

### 2.2.2. Reactive ion etching (RIE).

RIE is a plasma treatment technique that combines both chemical and physical etching to remove, activate or functionalize material. The principle is based on the plasma discharge in the atmosphere of chemically active gases. Common examples are O<sub>2</sub>, F<sub>2</sub>, Cl<sub>2</sub>, halogen-containing gases (CF<sub>4</sub>, CCl<sub>4</sub>, CF<sub>3</sub>Cl, COF<sub>4</sub>, SF<sub>6</sub>, and NF<sub>3</sub>) and their mixtures. Being ionized, such gases produce chemically aggressive species (etchants) that easily react with the adjacent surface thus leading to the material removal in the form of gaseous by-products like CO, CO<sub>2</sub>, H<sub>2</sub>O (see Figure 6 center). Such a chemical process could be also enhanced by physical etching. In the strong electric field, the incident etchants can gain enough energy to eject atoms from the surface without chemical reaction. A chemical etching is highly selective and isotropic, whereas a physical component contributes to the etching process anisotropically (similarly to sputtering). Since the REI induce the isotropic and anisotropic processes simultaneously, the resulting shape of the etching profile could be adjusted by changing the plasma conditions, i.e. altering the etchants/ions ratio.

In addition to the cleaning effect, the RIE could activate and functionalize the surface through the introduction of new functional groups. Reactive etchants can easily incorporate into the organic or inorganic structure of the material forming new chemical bonds. Eventually, the chemical composition of the solid material could be completely modified. Since chemical composition is directly related to the wettability

of material, many of interfacial characteristics can be affected, such as adhesion, absorption, chemical reactivity, permeability etc. For example, O<sub>2</sub> and N<sub>2</sub> plasma etching is widely used to improve the wettability of various materials through the introduction of hydrophilic -COOH, -OH or NH<sub>x</sub> functional groups [4,21].

It is worth mentioning, that plasma etching could significantly modify the topography of the surface. Wohlfart et.al used O<sub>2</sub> plasma to increase the roughness of the PET substrates (Figure 7) [23]. Also, plasma discharge is a source of highly intense UV radiation due to the recombination of excited species. This feature is widely used for sterilization purposes.

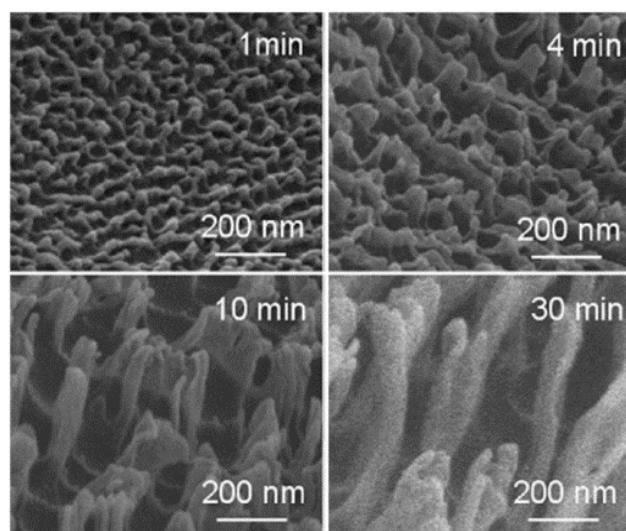


**Figure 7.** Scanning electron microscopy (SEM) images of polyethylene terephthalate treated with oxygen plasma for different treatment times (adapted from [23]).

### **2.3. Coating deposition.**

Another possibility is the surface modification of material by covering it with thin organic or inorganic films. Such coatings could endow materials with unique properties and serve as protective or barrier layers. Essentially, two types of techniques associated with plasma deposition could be distinguished: sputtering deposition and PECVD.

### 2.3.1. Sputtering deposition.

As previously mentioned, physical etching is realized through the bombardment of material with positive ions. In the case of sputtering deposition, the cathode is covered with material to be sputtered - so called target. Target is bombarded by ions accelerated in the cathode sheath. When the energy of incident ions is similar or higher than the binding energy of target material, atoms or clusters are ejected from the target surface. Under the sufficiently low pressure sputtered material spreads out linearly from the target in all direction. Hence, the adjacent surface will be covered with sputtered material forming a thin film. The deposition rate depends on the energy of the incident ions and target material. The structure, density and roughness of the resulting film strongly depend on the pressure in the deposition chamber and the temperature of the substrate. The effect can be presented on the example of Thornton diagram (Figure 8). The details description can be found elsewhere [24].

Sputtering is widely used for deposition of metal films in a DC, RF or high-power impulse magnetron sputtering (HIPIMS) mode. Interestingly the technique can be used for the deposition of thin films of plasma polymers. In this case, polymeric solid target instead of a metallic target is used in the RF discharge.

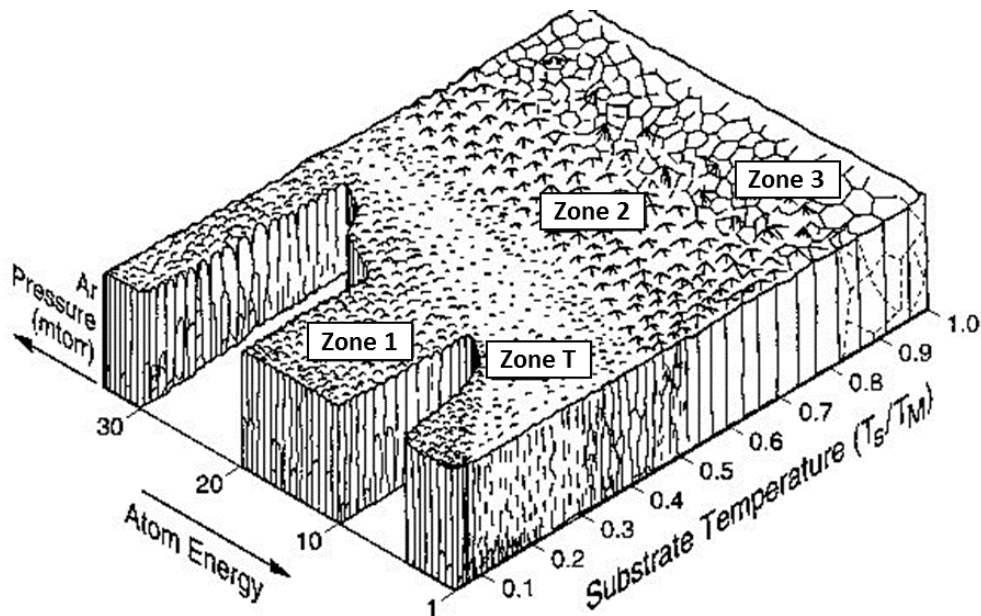


**Figure 8.** Structural zone model proposed by Thornton for sputtered metal coatings (after Ref. [24]).

### 2.3.2. Magnetron sputtering.

Magnetron sputtering is a well-known technique for thin film deposition [25–27]. In comparison with conventional sputtering deposition, the technique allows to achieve a much higher sputtering rate by using a magnetic field. Magnetic field increase electron confinement and local density of the plasma and thus generate more incident ions to bombard the target surface. As a result, discharge with higher current density and lower voltage can be obtained [28–31].

In practice, a magnetic circuit with a set of permanent magnets is installed on the bottom side of the electrode (Figure 9). Superposition of magnetic and electric fields above the magnetron surface creates electromagnetic trap which effectively confines electrons in a position where E⊥B. Thus, electrons emitted from the cathode surface in addition to electric field force experienced Lorentz force that triggered them gyrating with cycloidal motion. The E×B drift increases electrons lifetime in cathode dark space enhancing the efficiency of plasma ionization processes [30,32]. As a result, the increasing number of incident ions provides more intense sputtering of the target material. For example, sputtering efficiency (integrated energy efficiency factor) of a copper target increases with magnetic field growing up to 140 mT and remains relatively stable at higher values [33].

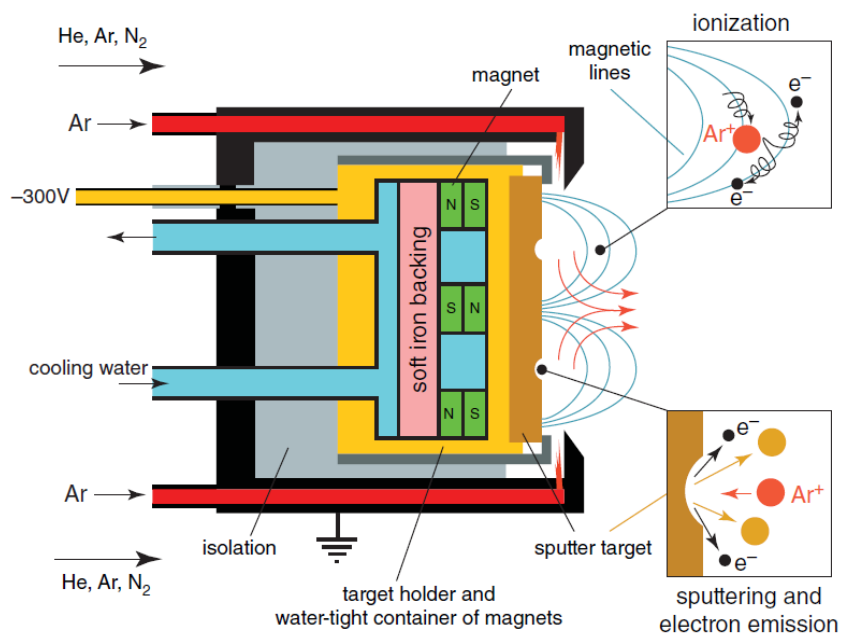


**Figure 9.** Schematic representation of the magnetron setup (adapted from [25])

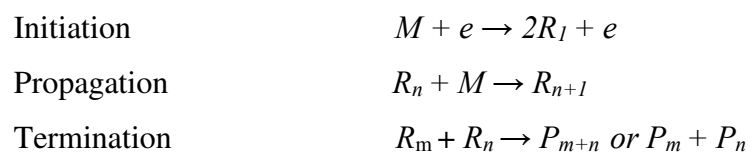
### 2.3.3. Plasma-enhanced CVD (PECVD).

Along with the sputtering deposition, PECVD belongs to the group of coating deposition techniques where the plasma discharge is used to initiate the deposition process [18]. The schematic illustration of the deposition process is depicted in Figure 6 (right). The addition of a small amount of vaporous or gaseous precursors (hexamethyldisiloxane, n-hexane, styrene, acetylene, methacrylate, titanium tetrachloride etc.) to the RF discharge leads to the fragmentation of the precursor molecules with the subsequent formation of chemically active radicals [34]. Thin films are then deposited on the cathode (typically RF electrode) or any object exposed to the plasma region. Either grounded holder or isolated holder which is at the floating potential can be used [35,36].

The properties of deposited films depend on the nature of the precursor, working gas mixture and the intensity of ion bombardment of the growing film. As an example can serve organosilicon coatings prepared by PECVD in the atmosphere of hexamethyldisiloxane (HMDSO). Such coatings exhibit good biocompatibility and unique possibility to adjust the wettability of the deposited coatings. Simply, varying the mixture of working gases (HMDSO with Ar or O<sub>2</sub>) during the deposition process, hydrophobic and amphiphilic films can be obtained [8].

Plasma discharge in the atmosphere of organic monomers is a quiet complex mixture of electrons, ions, neutrals, radicals and their derivatives. Various mechanisms for the formation and growth of plasma polymers were suggested including electrons or ions impact initiation [21,37], cationic polymerization [38], chain-growth polymerization [39] etc. In such case the term plasma polymerization (PP) instead of PECVD is often used.

In the early studies, the mechanism of plasma polymerization was considered to be quite similar to the conventional polymerization process, where the initiation of the process was triggered by the electrons impact. For example, Lam et al. [40] and Tibbit et al. [39] suggested a three-step mechanism of plasma polymerization:



where  $M$  is monomer molecule,  $e$  – electron,  $R$  – radical,  $P$  – neutral mol. or polymer.

A more detail description of the plasma polymerization was proposed by Yasuda et.al [41]. The schematic diagram of such a polymerization route is shown in Figure 10. The mechanism is based on the principle of the simultaneous ablation and polymerization during the deposition process. In this case, polymerization includes two possible pathways either the plasma state or plasma induced. Plasma-state polymerization occurs when the plasma activates or fragments the monomer molecules to obtain chemically reactive radicals so that the plasma polymerization takes place. In plasma-induced polymerization, the precursor molecule can chemically interact with radicals on the growing surface without initial activation (much less common pathway). In turn, ablation process leads to the loss of plasma polymer in gas form due to the ion bombardment or UV irradiation.

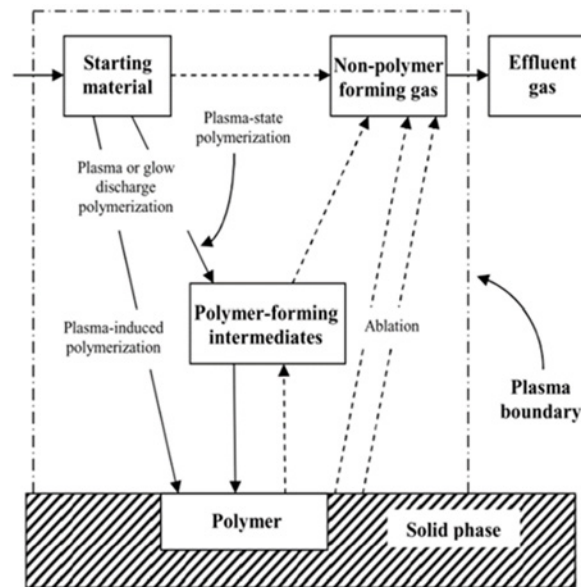


**Figure 10.** Schematic representation of the plasma polymerization process and possible route during the plasma polymerization (after Ref. [41]).

Another classical view on the plasma polymerization is a rapid step-growth polymerization – a bicyclic mechanism with multiple pathways [42,43]. In this case, mono and difunctional radicals are considered as the only growing species while the growth is propagated by multiple directions and pathways (see details in Figure 11).

One of the most advanced models that describes the deposition mechanism for PECVD is the activated growth model proposed by P. Favia [16]. In this model, along with the plasma processes in the gas phase, the ion bombardment and temperature of the substrate during the deposition of the coating are taken into account.

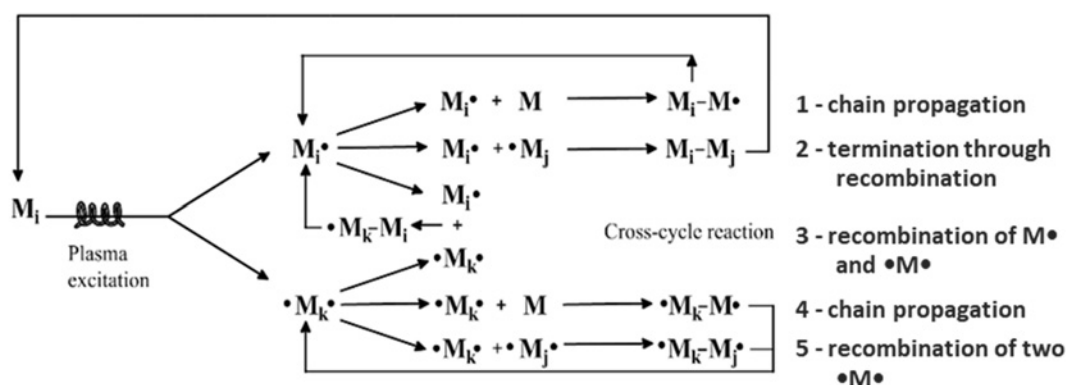


**Figure 11.** Schematic representation of the bicyclic step-growth mechanism of plasma polymerization. Here  $M^\bullet$  and  $\bullet M^\bullet$  are mono- and difunctional molecules. (adapted from [41])

Unlike conventional polymers, plasma polymers do not contain regular repeating units and could be characterized by a high degree of cross-linking and branching. Produced plasma polymers are pinhole free and normally demonstrate good adhesion to surface. The chemical composition or structural characteristic of the plasma polymers can be well adjusted by choosing a monomer type and the energy density per monomer. Such a relation is known as Yasuda parameter and can be written as  $W/FM$ , where  $W$  is power of discharge,  $F$  – molar flow rate of the monomer,  $M$  – molar mass of the monomer.

According to the above, the hardness and density of plasma polymers can be adjusted in wide range by varying the energy flux into the growing films. In the RF discharge the energy of incident species is given by the electrode negative self-bias. Under the low energy flux, the bombardment of the plasma polymer surface is low resulting in the soft thin films. In turn, high energy flux leads to the formation of very compact and hard coatings. As the example can serve plasma polymerized hydrocarbon coatings with different ratios of  $sp^3$  and  $sp^2$  hybridized carbon-carbon bonds and varying hydrogen content (Figure 12). In dependence on the negative self-bias and the energy density applied per monomer (Yasuda parameter), graphite-like (soft) or diamond-like (hard) hydrocarbon thin film can be prepared [16].

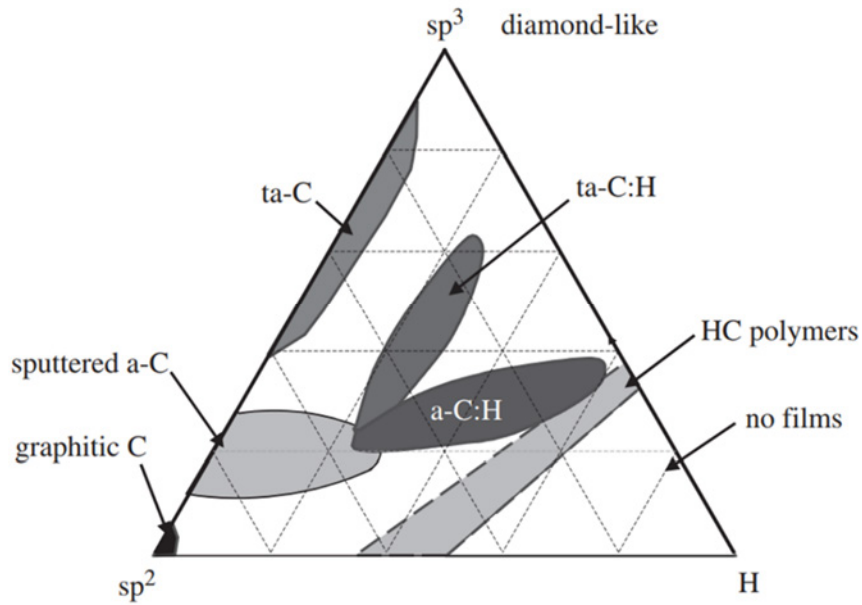


**Figure 12.** Ternary phase diagram of amorphous carbons. The three corners correspond to diamond, graphite and hydrocarbons respectively (adapted from [44]).

One more possibility is the deposition of thin films on the grounded substrate directly in the plasma or afterglow region. In this case, the potential drop on the interface plasma/sample is low. Thus, under low values of the Yasuda parameter, soft polymer films with the structure similar to those of the original monomer molecule can be obtained.

## 2.4. Nanoparticles fabrication by gas aggregation source

Within the last two decades, effective preparation of NPs by means of gas aggregation cluster source (GAS) has found a considerable interest [45,46]. Despite expensive and to some extent sophisticated tools (in comparison with wet chemistry), such a physical route offers several advantages: environmental friendliness; low materials consumption; possibility to prepare alloy or core-shell NPs; precise control of their size, shape, structure or chemical composition [47,48]. In addition, GAS makes it easy to deliver NPs onto the specific substrate that along with compatibility with other vacuum-based techniques provide a flexible solution for the production of nanostructured and nanocomposite functional materials [5,49,50].

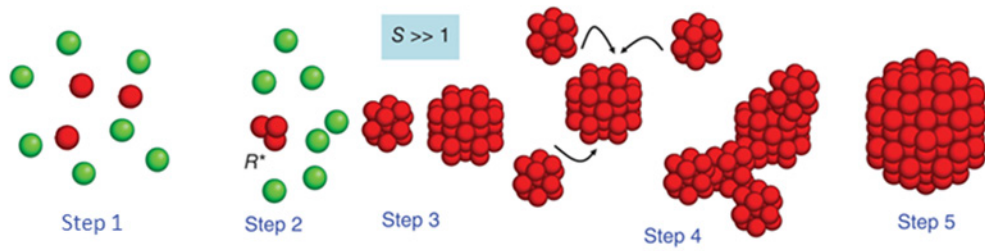


**Figure 13.** Schematic representation of the mechanism of metal nanoparticle formation in GAS, where step 1 is metal atoms and buffer gas in adiabatic expansion; step 2 – nucleation; step 3 – rapid growth through condensation; step 4 – coalescence of clusters; step 5 – rearrangement of the inner structure (adopted from [25]).

In general, condensation of the metal atoms from the gas phase and the following nanoparticle formation can be described by 5 main steps as could be seen in Figure 13. Step1. Magnetron sputtering of the metal target was used as a source of metal atoms. Step 2. Nucleation is rather a complex process that depends on numerous elemental processes in the plasma. The primary embryo is formed under the three-body collision process as follows:



where A is an atom and X is third body (usually neutral atom: Ar, Ne).

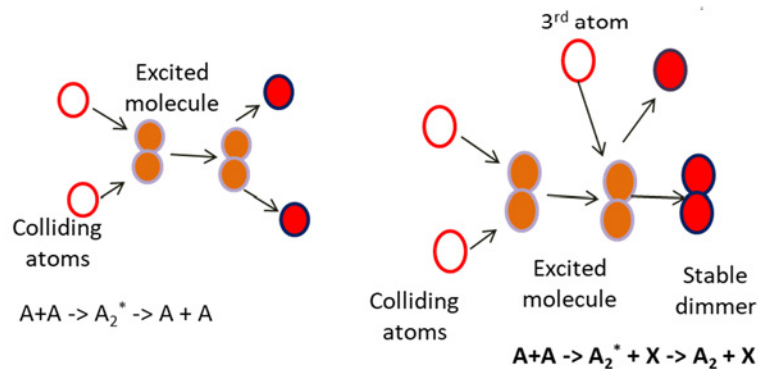


**Figure 14.** Schematic representation of the dimer formation mechanism.

The dimer formation through the excited molecule is illustrated in Figure 14. When two atoms collide together, an excited molecule is formed. However, such a molecule is unstable. The heat releasing during the bond formation causes the dimer destruction. In contrast, during three-body collision, the third atom takes away excessive heat and momentum from the excited molecule that provides a formation of

the stable dimer. In general, atoms of noble gases (Ar, He, etc.) used for the sputtering act as a buffer gas to provide a cooling effect. Therefore external cooling of the aggregation chamber using liquid nitrogen or water is used to lower the temperature.

Step 3. Consequently, obtained dimers start acting as critical seeds for condensation of sputtered atoms. If the deposition rate (DR) of the sputtered atoms on the surface of the cluster is higher than the evaporation rate, the nanoparticle growth mode is reached. Essentially, NP growth can be devoted to surface growth characterized by the addition of single atoms on NP surface. In a next step growth by coagulation with further coalescence of NPs is reached - step 4. Coagulation happens in the presence of a large number of nanoparticles in the aggregation zone leading to inelastic collisions between them. Step 5 – the rearrangement of inner structure of the nanoparticle. More information on NPs formation and growth mechanisms can be found elsewhere [51–54].

Such a mechanism implies that growing NP undergoes multiple collisions with atoms, electrons, ions and other species in the ionized environment and numerous forces (drag force of gas, electrostatic force, thermophoretic etc.) are acting on it during its way to the exit orifice. Therefore, the efficiency of the NPs formation, their final size, shape, and crystal structure are highly dependent on a specific combination of elemental processes involved in NP formation and growth mechanism. A fine-tuning of such processes can be realized through the adjustment of the macroscopic conditions in GAS. Formation of many types of metallic nanoparticles (Pt, Ag, Cu, Ti, etc.) were studied in our group in dependence on working parameters such as DC magnetron current, pressure and flow rate of a working gas, composition of gas mixture, aggregation length, residence time of NPs in aggregation zone etc. [25,45].

Many different types of GASes were proposed. The main difference between them is a source of metal vapours [55]. One of the most popular GAS is based on magnetron sputtering and it was originally designed by Haberland et al. [56]. In this type of the GAS, magnetron sputtering act as a material source for NPs formation. Compared to evaporation based cluster sources the use of a planar magnetron enabled significant increase of the deposition rate (DR) and production of charged NPs which also improved control capabilities of the process [25–27]. Similar to conventional magnetron sputtering, using stronger magnets increases electrons confinement [57]. Hence, provide a higher number of sputtered atoms for NPs growth [58].

## 2.5. Nanocomposite films

The nanocomposite is a multiphase solid material where one of the individual components or structural repeating blocks is in a nanometer scale (normally less than 100 nm). The idea is to combine two or more materials with different chemo-physical properties to fabricate a new generation of materials with unique structural or functional properties.

The rapid development of the plasma deposition (PECVD or PP) in the second half of 20<sup>th</sup> century and its compatibility with other techniques contribute to the formation of the new class of nanocomposite materials – metal/polymer films [59–61]. Since the first reports in the 1970<sup>th</sup>, a number of methods were designed for fabrication of such a metal/polymer nanocomposites, for example:[16]

- ✓ Magnetron sputtering and simultaneous plasma polymerization
- ✓ Co-sputtering from two targets
- ✓ Magnetron sputtering and simultaneous “evaporation” of a polymer
- ✓ Simultaneous plasma polymerization of organic gas and evaporation of a metal
- ✓ Plasma polymerization of metal-organic compounds

Recently, a new approach based on the combination of the plasma deposition and GAS was developed offering several advantages as compared to conventional methods, namely: independent control of the deposition process of matrix and nanoparticles; possibility to be used in a simultaneous or step-by-step regime; and last but not least, such an approach prevents degradation of the resulting coatings as NPs by GAS reach the matrix completely formed. The technique allows to obtain nanostructured composite coatings in a wide range of wettability endowed with unique properties, for example, antibacterial activity [12,49,62]. The surface energy could be tailored by the thin film deposition during the PECVD [63]. Whereas, the surface roughness could be adjusted independently by introducing a specific number of nanoparticles.

One of the key parameters to characterize the nanocomposite materials is a filling factor  $f$  that determines the volume fraction of metal embedded in the composite:

$$f = \frac{V_{metal}}{V_{composite}} \quad (8)$$

where  $V_{metal}$  is the volume of metal inclusions and  $V_{composite}$  is the volume of nanocomposite.

Changes in the filling factor have a strong effect on the nanocomposite properties. For example, optical characteristic of the metal/polymer nanocomposites can be adjusted by tailoring the Ag content in the polymeric matrix. Since Ag nanoparticles exhibit a characteristic absorbance in the visible range of spectra, the intensity and shape of the absorbance peak can be modified significantly increasing the Ag concentration, i.e. filling factor (Figure 15).

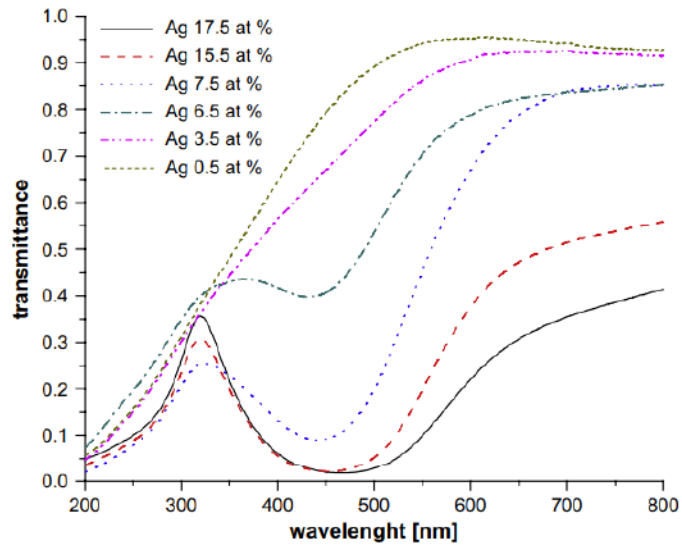


**Figure 15.** UV–Vis transmittance of Ag/C:H films as a function of Ag content (adopted from [7]).

In general, nanocomposite properties change smoothly with increasing filling factor. However, in the case of thermal conductivity or electrical properties, the dependence is more complex. In Figure 16 the resistivity is presented as a function of the metal volume fraction. In this case, a small amount of filler has negligible effect on the electrical properties and the resistivity remains high. This happens until a so-called percolation threshold is reached – the point where an abrupt reduction in the resistivity occurs. Further increase of filler fraction leads only to equalize conductivity [16].

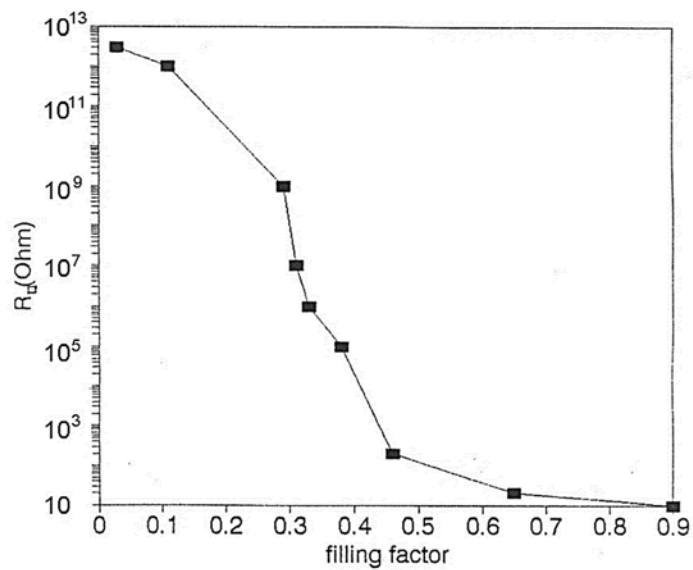


**Figure 16.** Dependence of resistivity on the filling factor for Ag/C:H (adopted from [16]).

## 2.6. Application perspectives

In this chapter are described two applications where plasma treatment of porous structures plays important role and which were motivation for the research presented in this thesis.

### 2.6.1. Water purification from non-polar organic contaminants

Widespread usage of organic chemical compounds in industry, agriculture, food sector as well as increasing consumption of fossil fuels causes significant growth of water pollutions. Such oily wastewater has a harmful effect on the environment and human health [64,65]. Hence, the development of new, effective and inexpensive solutions for oily water purification is necessary.

Over the past few decades, membrane-based methods for oil/water separation have found a considerable research interest [66–68]. Ones demonstrate high separation efficiency, sufficient durability and recyclability, easy integration into existing purification systems and provide a low-cost solution, simply being driven by gravity. Four main types of the membranes could be distinguished: superhydrophobic/superoleophilic [69–71], superhydrophilic with underwater superoleophobicity [72–74], superhydrophilic with superoleophobicity both in air and underwater [75], and special types of smart membranes [76].

Superhydrophobic/superoleophilic or so-called oil-removing membranes are probably the most studied group of materials in terms of their application for oily water purification [77–86]. Since the surface tension of water is predominantly higher than those of oils, such a wetting behavior is inherent to the solid interfaces with the tension between those of water and oil. With typical water contact angle (WCA) above  $150^\circ$ , superhydrophobic materials completely repel water and exhibit a strong affinity (oleophilicity) to non-polar chemical compounds – oils, and thus provide an effective solution for selective adsorption of various oils from water. On the other hand, the separation ability of oil-removing membranes is rather limited, i.e. suitable only for filtration of heavy oils ( $\rho_{oil} > \rho_{water}$ ). In the case of light oil/water mixture ( $\rho_{water} > \rho_{oil}$ ),

water settles beneath the oil due to the phase separation and simply prevent oil contact with membrane thus terminate the separation process.

In recent years, the water-removing type of membranes found a considerable interest to be used for water/oil separation [87–92]. Such superhydrophilic/underwater superoleophobic materials allow water to easily penetrate the membrane whereas oil is effectively repelled out. The basic principle utilizes the advantage of materials with high surface energy to adsorb water and the fact that formed solid-water interface exhibit superoleophobicity. In addition, several authors managed to obtain superhydrophilic/superoleophobic materials both in air and underwater [74,93–98]. This is not very common wetting behavior since superoleophobic materials usually exhibit superhydrophobicity. To overcome this issue, a combination of hydrophilic and oleophobic constituents was employed. Along with high efficiency of the separation process, water-removing membranes allows overcome existing fouling issue with superhydrophobic coatings, thus essentially increase the membranes lifetime and recyclability. Obviously, such materials are not suitable for gravity-driven separation of heavy oils.

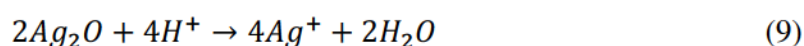
One of the promising trends in the field of water purification is the development of smart materials [99–102]. Recently, several scientific groups reported the fabrication of advanced membranes with switchable wetting behavior in response to various external stimuli such as electrical field, pH, light etc. [76,100]. Moreover, Lei Zhang et al. developed special multifunctional catalytic membranes that provide both decomposition of water-soluble organic compounds and effectively separate oil/water emulsions [103]. For sure, smart materials have a number of advantages, but at the moment their fabrication and usage are too sophisticated and usually less energetically efficient.

Fabrication of highly efficient membrane requires proper combination of the chemical composition of the surface, surface roughness and overall porosity of a membrane. While the surface energy and roughness determine a wetting regime of the membrane, the inner structure (porosity) defines the permeability and flow rate through the membrane. Taking into account aforementioned, the majority of the scientific work is focused on the surface modification of already available porous substrates (including textiles, foams, sponges, metal meshes, polymeric membranes etc.) to obtain super-wettable porous materials. Various approaches were applied such

as dip coating, spin coating, a salt-induced phase inversion, grafting, blending, chemical vapor deposition (CVD) etc. All of these methods are to some extent limited to the fabrication of a certain type of the membrane with specific wetting behavior. In this thesis presented plasma-based approach was developed to obtain both superhydrophobic and superamphiphilic membranes within the framework of the same modification process.

## 2.6.2. Biomedical applications

It is well known that some nanoparticles of metals like Ag, Cu etc. exhibit antibacterial properties [104]. The general mechanism is based on the ion release by the oxidative dissolution reaction when the NP is placed in the aqueous environment [40,105]. For Ag NPs such reaction could be described as follows [106]:



Consequently, free ions could be easily incorporated into the bacteria structure targeting some essential biomolecules (DNA, enzymes etc.). Such interaction causes inhibition of the metabolic pathways as well as the destruction of the membrane and eventually leads to the bacteria death [107].

Mixing metallic NPs with plasma polymer films provides a flexible solution for fabrication of nanocomposite coatings. Such metal/polymer nanocomposites are of great interest to be used in the field of biomedical applications. One exhibit excellent biocompatibility as well as antibacterial activity. The biocompatibility is determined by the properties of the plasma polymer films acting also as a diffusion barrier to control the release of metal ions, while the antibacterial activity depends on the number of metallic NPs embedded into the matrix [108,109].

One of the promising applications of metal/polymer nanocomposites is functional coatings for bone implants. In this case, nanocomposite properties, such as hardness or the time evolution of antibacterial effect should be properly tailored. Thus further study and development of nanocomposite coatings are of great importance and this topic is covered in this thesis.

### **3. Experimental techniques**

Most of the experiments involving preparation of samples and their plasma processing were carried out on the facilities of the Department of Macromolecular Physics, Charles University (MFF, UK). Due to the high number of deposition techniques and characterization methods used in this study and in order to keep a reasonable size of the work, only selected experimental techniques will be described in details.

#### **3.1. Deposition techniques and plasma treatment.**

##### **3.1.1. Deposition of plasma polymer thin films.**

The deposition of plasma polymer films was performed in high vacuum stainless steel deposition chamber equipped with a planar electrode powered by RF power supply (Dressler Cesar 133). The substrates were mounted on a grounded holder 5 cm apart from the RF electrode in case of soft film deposition or placed directly on the electrode for deposition of hard coatings (position 1 and 2 in Figure 17 respectively). The chamber was pumped by diffusion and rotary pumps to the base pressure better than  $1 \cdot 10^{-3}$  Pa. In order to provide flexible reconfiguration of the deposition setup, the chamber was equipped with a set of internal ports and flanges which enable easy connection of the electrodes, measurement probes, GAS etc. For the fast transfer and replacement of the samples, the chamber was equipped with a load-lock system with the additional diffusion/rotary pumps system. The continuous flow of working gas (Ar) and precursor into the deposition chamber was controlled by needle valves. The pressure in the deposition chamber was measured by means of baratron (1 Torr, MKS) connected to the two-channel digital readout (PDR2000A, MKS).

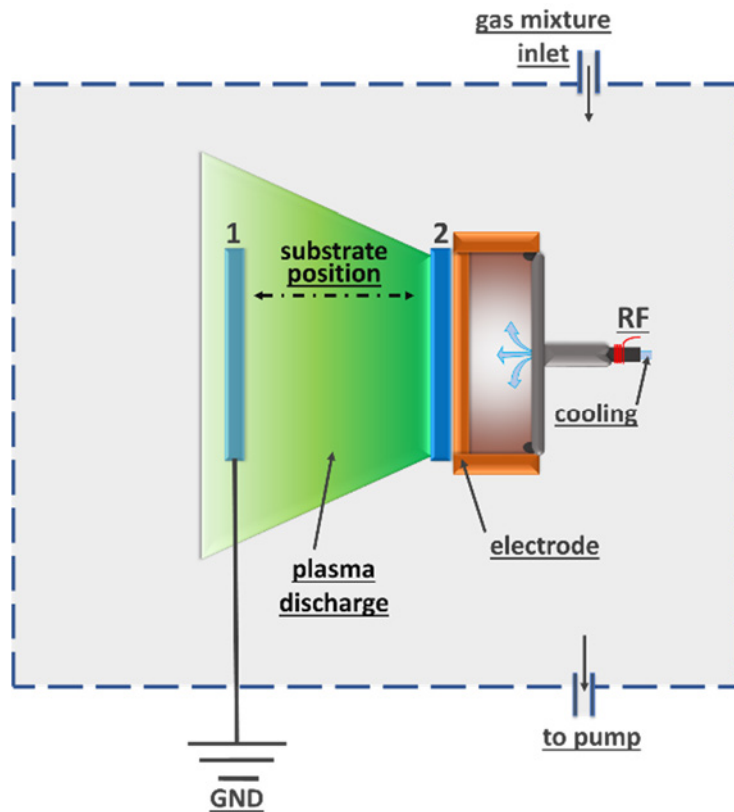


**Figure 17.** Schematic arrangement utilized for the deposition of thin films of plasma polymers and the plasma etching of Ag/a-C:H nanocomposite coatings.

### 3.1.2. Plasma etching

Nanocomposite films were etched in three different types of plasma in order to increase Ag surface concentration. The etching was carried out in the same vacuum chamber which was used for the deposition of thin films. Three different cases were investigated. In first two cases, samples were placed directly on the RF electrode (position 2 in Figure 17) and oxygen or nitrogen plasma was used to etch the surface. In the last case, the sample was placed on the grounded substrate holder 5 cm apart from the electrode with the coating facing it and oxygen plasma was used (position 1). The pressure was set to 2.5 Pa in all cases and the RF power was kept constant 16 W with corresponding negative self-bias around 150 V.

### 3.1.3. Gas Aggregation Source (GAS) of nanoparticles

Haberland type of gas aggregation source of nanoparticles [110] of our own construction was used for deposition of metallic and polymeric NPs. The schematic illustration of GAS is presented in Figure 18. The GAS consists of a tube-like chamber which ends by a cone with a 2 mm orifice connecting the GAS to the deposition chamber. The GAS was equipped with DC planar magnetron or RF electrode. The pressure difference in both chambers directed the beam of NPs into the deposition chamber providing the soft landing of NPs on the substrate holder 18 – 23 cm from the orifice. Both magnetron or electrode and GAS-chamber were externally water cooled.

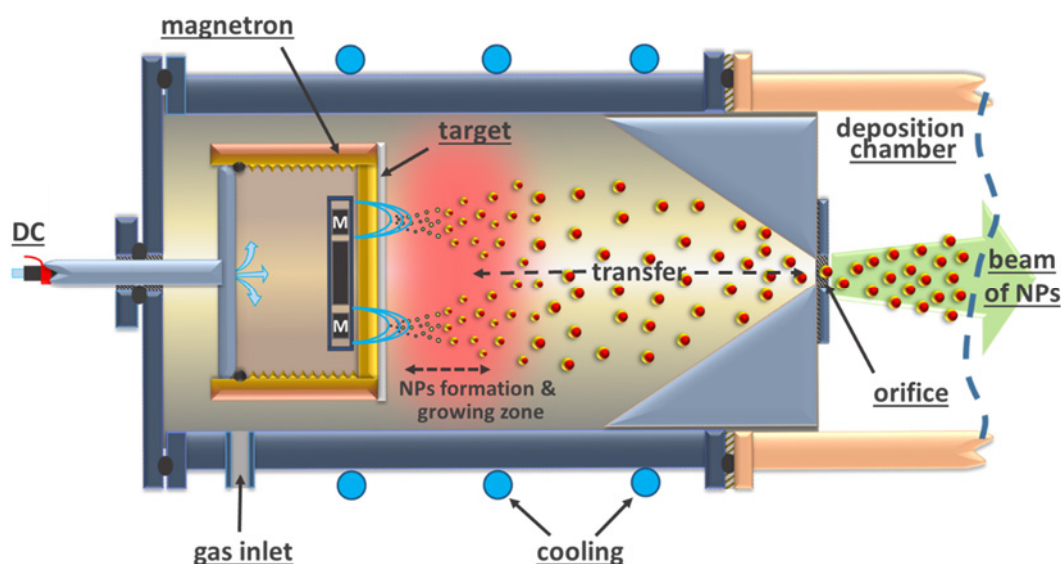


**Figure 18.** Schematic representation of the GAS implemented for the fabrication of metallic nanoparticles.

*Ag NPs.* In the case of Ag NPs fabrication, GAS was equipped with 81 mm planar magnetron with 3 mm thick Ag target (purity 99.99%). The magnetron was driven by DC power supply (Advanced Energy MDX 500 DC) operated in a constant current mode. The number of produced NPs was tailored varying the DC current from 100 to 500 mA. Argon (purity 99.99%) was used as a working gas and its pressure was kept in the range of 20 Pa to 100 Pa (corresponding flow rates 2.3 sccm – 15.7 sccm).

*Cu NPs.* GAS equipped with a specially constructed 81 mm planar magnetron that enabled the adjustment of the magnetic field above Cu target was used for deposition of Cu NPs. Intensity of magnetic field above 3 mm thick target (purity

99.99%) varied from 35 mT to 83 mT (Figure 19). Variation of the field was performed manually by changing the distance between the magnetic circuit and the electrode surface. A special circuit of permanent magnets (HVM plasma) was designed to provide the invariable shape of the magnetic field with different intensity (see Figure 20). The optimization of the magnetic field lines will be discussed more in detail in the section 4.1.1. Similar to Ag NPs, DC power supply was operated in constant current mode (100 mA – 500 mA) and the pressure of Argon (purity 99.99%) in the aggregation chamber was varied from 20 Pa to 100 Pa.

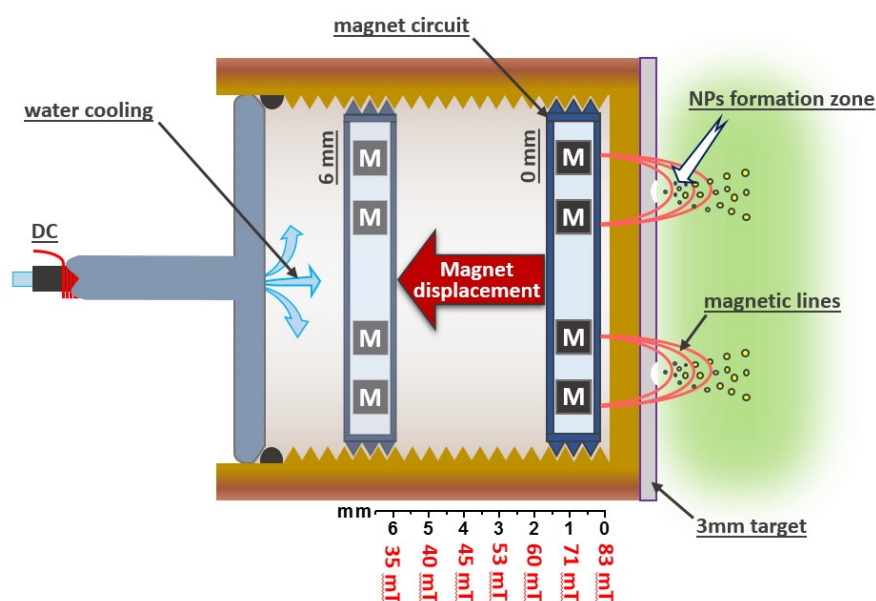


**Figure 19.** Schematic illustration of the magnetron with the adjustable magnetic field: displacement of the magnetic circuit from 0 to 6 mm corresponds to the changes in the intensity of the MF in the range of 83 mT – 35 mT above the target.

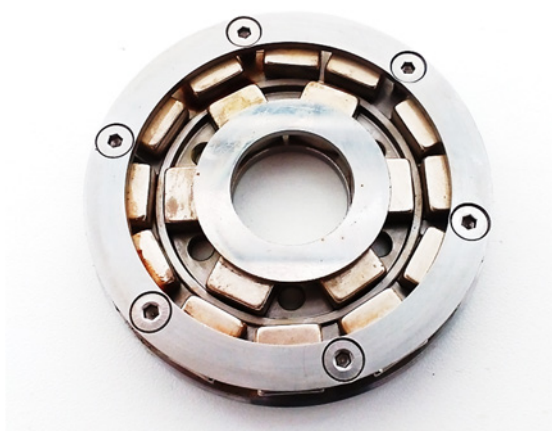


**Figure 20.** Photograph of the magnetic circuit used in the magnetron with the adjustable magnetic field.

*Polymeric nanoparticles.* The deposition of hydrocarbon (C:H) NPs was carried out in a GAS equipped with 81 mm in diameter RF electrode instead of the planar magnetron. The electrode was covered with 0.5 mm carbon foil to minimize its sputtering. The discharge was driven by RF power supply (Dressler Cesar 133) in the mixture of Ar and n-hexane (27:1) under the total pressure of 54 Pa. The applied RF power was 70 W. More details about the synthesis of the polymeric and metallic NPs by means of GAS will be discussed in the Results and Discussion chapter.

### 3.1.4. Fabrication of functional nanocomposite coatings.

*Hard Ag/a-C:H nanocomposite coatings* were prepared by simultaneous deposition of Ag nanoparticles (NPs) and plasma polymerization of n-hexane. The Ag NPs were fabricated by a GAS as it was discussed earlier. The beam of the NPs was directed onto the substrates (Si wafer, Ti disc) located on an electrode as it is depicted in Figure 21. The electrode was RF driven to sustain plasma in the mixture of Ar and n-hexane (10:1) at a pressure of 5.5 Pa. RF discharge was operated in the pulsed regime with the frequency of 1Hz and duty cycle of 50%. Under these conditions, the NPs reach the substrate only during  $T_{off}$ . The discharge power was varied from 30 W up to 90W with negative self-bias changing from 210 to 410 V respectively. This setup allowed independent control of the amount of the embedded Ag NPs and the properties of the a-C:H matrix.

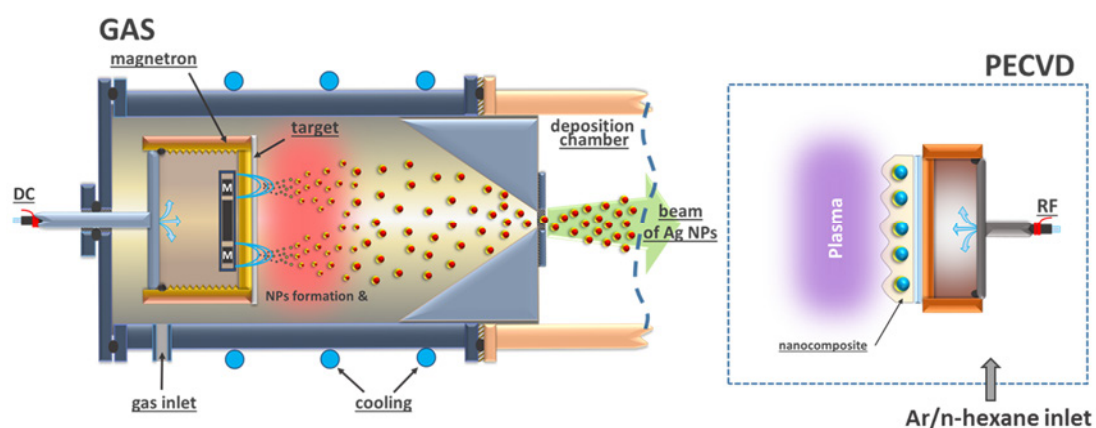


**Figure 21.** Schematic representation of the experimental setup for the fabrication of hard Ag/a-C:H nanocomposites.

*Fabrication of the Superhydrophobic and Superamphiphilic membranes.* Step-by-step deposition process was implemented to prepare nanostructured composite coatings with wide range of wettability. The experimental arrangement was based on two sources of NPs and RF electrode for plasma polymerization of thin films (see Figure 22). Metal and polymeric NPs sources were mounted on the main chamber so that the beam of NPs was directed towards the RF electrode. Sequential use of the GAS and PECVD resulted in a sandwich-like structure of the nanocomposite coating as follows: superhydrophobic – (C:H)SiO<sub>x</sub> (100 nm), C:H NPs (sub-monolayer), (C:H)SiO<sub>x</sub> (50 nm), Cu NPs (monolayer), (C:H)SiO<sub>x</sub> (10 nm); superamphiphilic – SiO<sub>x</sub> (100 nm), Cu NPs (monolayer), SiO<sub>x</sub> (10 nm). Prior to the modification process viscose fabric and carbon paper were cleaned with ethanol and deionized water for 5 min in an ultrasonic bath to wash out the impurities. After proper drying, clean textiles with the size of 20 × 70 mm were placed on the grounded substrate placed 5 cm apart from RF electrode in the main chamber where the modification process took place as described above.

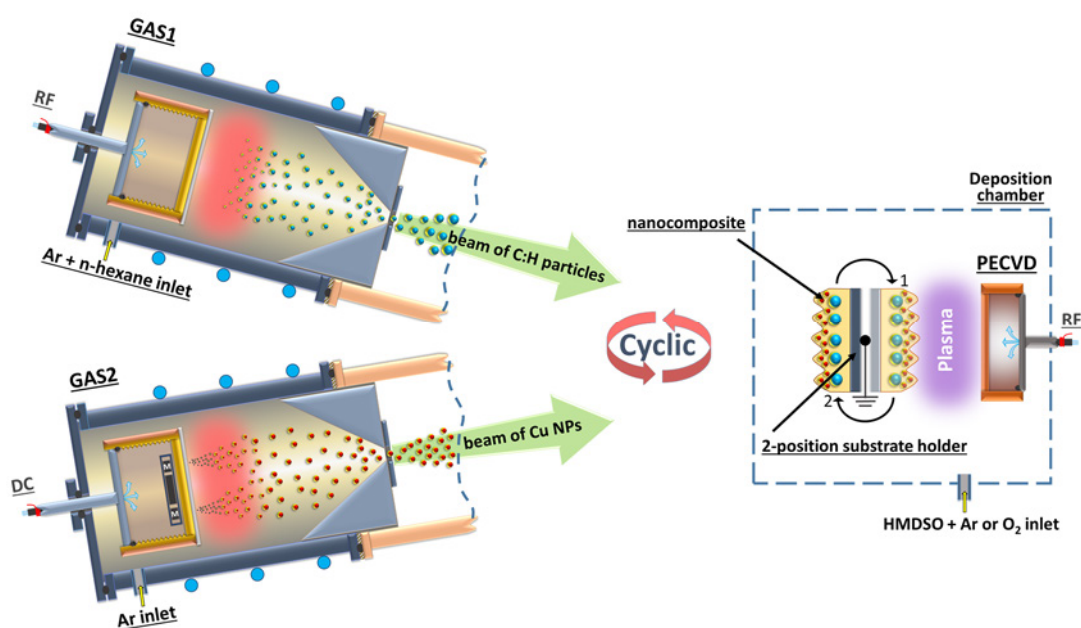


**Figure 22.** Schematic arrangement for the modification of filtration membranes.

## 3.2. Characterization methods

### 3.2.1. Quartz Crystal Microbalance (QCM)

Quartz crystal microbalance is an *in-situ* technique utilizing a piezoelectric effect to determine the mass deposited on a surface of a quartz crystal. QCM consist of a circular quartz crystal (AT or BT cut) with two metal electrodes on both sides connected to the power supply, frequency counter and computer interface (Figure 23).

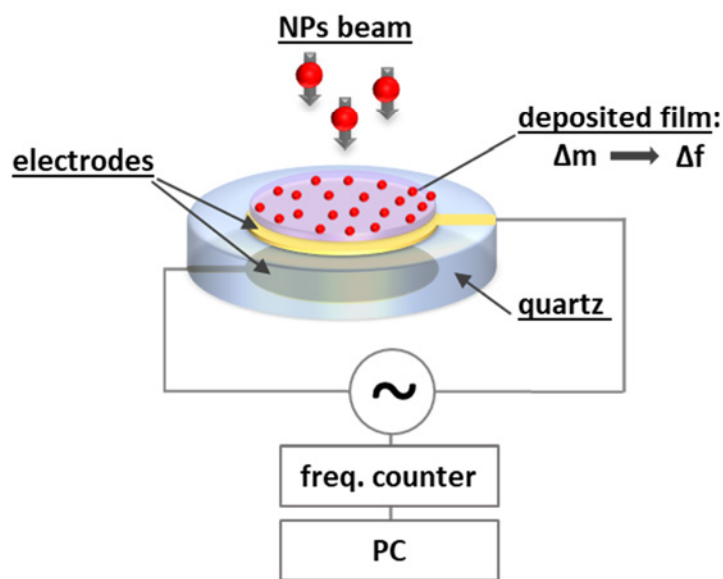


**Figure 23.** Schematic representation of the QCM.

The relation between the mechanical deformation of the quartz crystal, its thickness and applied current is well established. This allows adjusting an acoustic resonance by electrical means. When AC voltage is applied to the quartz, an acoustic shear waves propagate along the crystal at resonance frequency ( $f$ ):

$$f = \frac{v_p}{2t} = \frac{N}{t} \quad (11)$$

where  $v_p$  is the velocity of transverse elastic waves;  $t$  is the thickness of crystal; and  $N$  is the crystal frequency constant (1670 kHz mm for an AT crystal cut).

When the thin film (mass) is deposited into the crystal, the thickness increases and the resonance frequency decreases. The mass change ( $\Delta m$ ) per unit area could be easily determined by measuring the change in the frequency ( $\Delta f$ ) of the quartz resonator according to Sauerbrey equation:

$$\Delta f = -\frac{f_0^2 \Delta m}{A \sqrt{\rho_q \mu_q}} \quad (12)$$

where  $f_0$  - resonant frequency, A - area of the crystal,  $\rho_q$  - quartz density (2.648 g/cm<sup>3</sup>),  $\mu_q$  - shear modulus of quartz.

Herein, QCM (Maxtek) equipped with 5 MHz quartz crystal 12.7 mm in diameter was used for monitoring the deposition rate of metallic NPs. The QCM was situated 5 cm apart from the exit orifice of GAS so the entire beam of NPs could reach the crystal.

### 3.2.2. Optical Emission Spectroscopy (OES)

Optical emission spectrometer AvaSpec 3648 (Avantes) with CCD linear array detector was employed for plasma diagnostic during the deposition of copper NPs. The main principle is based on the detection of the optical radiation emitted by atoms/molecules during the transition from excited to low energy states. Since each element has its own characteristic spectrum, the qualitative and quantitative analysis could be performed based on the peaks position, their intensity and broadening.

In our study, the emission spectra were acquired through a quartz window in the range of 240 to 850 nm at 10 mm distance from the center of the magnetron surface. The relative concentration of copper atoms in plasma under different deposition conditions was calculated as the ratio between Cu 353,03 nm and Ar 826,45 nm spectral line intensities. The integration time was fixed at 50 ms in all experiments.

### 3.2.3. Atomic Force Microscopy (AFM)

Atomic force microscopy belongs to the family of scanning probe microscopy (SPM) techniques that reproduce a raster image of the surface morphology based on the physical interactions between the scanning tip and sample surface. Unlike SEM, AFM images are three-dimensional and carry detail information about the surface structure from which statistical parameters like root-mean-square roughness, correlation length, growth exponent etc. can be calculated. The AFM probe is a tiny tip placed on flexible cantilever.

The imaging process is based on the cantilever movement in a raster manner. Moving along the surface in the x-y plane, the probe undergoes numerous interaction with the surface and thus experience multiple forces (mechanical contact force, van der Waals force, capillary forces etc.) that lead to the cantilever deflection according to Hooke's law. Such deflections are monitored in the real-time by the laser beam which is directed onto the back side of the cantilever so that the reflected beam can be collected by photodiode detector (see Figure 24). Depending on the amplitude of the deflection an output signal is produced and hence the topography of the surface is measured.

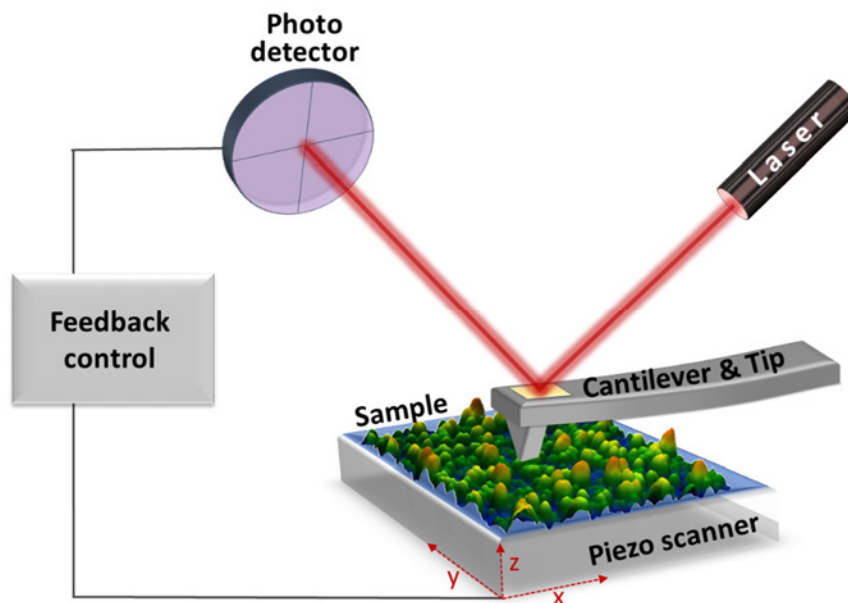


**Figure 24.** Schematic diagram of AFM operation.

Most commonly, the photodiode detector is connected to the piezo scanner through the electronic feedback loop. In this case, the cantilever deflection serves as an input signal for the feedback control, whereas its output adjusts the distance between the cantilever and substrate holder along the z-axis. Such scanning regime is called a constant force mode and the distance between the probe and sample (acting force) is adjusted by the setpoint defined by the user. Consequently, the information from the detector and the feedback system is analyzed by the software and the image of the scanning area is formed.

The above-mentioned mechanism represents the basic operational principle of the AFM. In practice, the instrument could operate in various working regimes. Three main modes could be distinguished: contact, semi-contact and non-contact – all correspond to the specific interaction between the probe and sample in dependence on the mutual distance. Acting atomic forces could be approximated by so-called Lenard-Jones potential as shown in Figure 25.

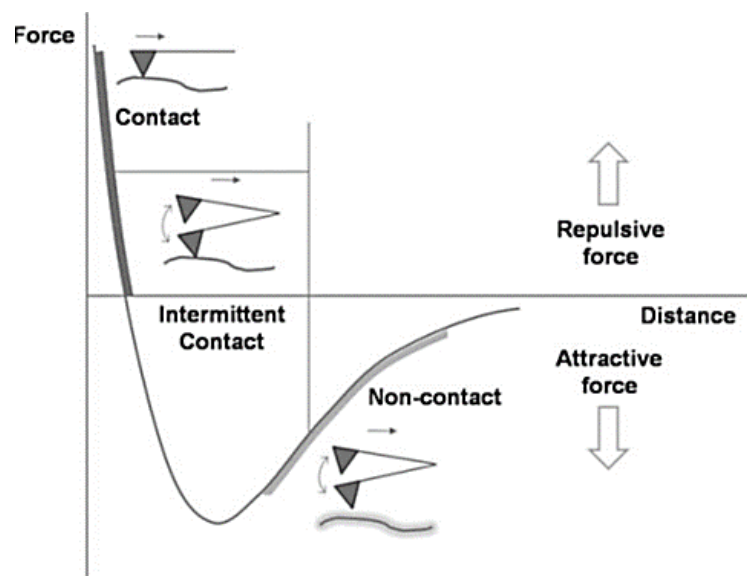


**Figure 25.** The force acting between the tip and the sample in dependence on the mutual distance (adapted from [111]).

The vertical resolution (z-axis) in the modern instruments is typically better than 0.1 nm and is given by the accuracy of the signal detection. In contrast, the resolution in a lateral direction (x-y plane) is on the order of nanometers and it is given by the accuracy of the piezoelectric elements. The lateral resolution is also worsen by the tip to surface convolution. The effect arises when the diameter of the tip is similar

or bigger to the topographical features of the surface being measured. As a result protrusions/holes on the surface appears to be wider/smaller.

In this work, thin film coatings were prepared on one-side polished Si substrates and the morphology of coatings was studied by atomic force microscopy (NTMDT Ntegra Prima). The AFM measurements for all samples were performed in a semi-contact mode using DLC coated tips with the radius better than 15 nm (Multi75DLC; Budget Sensors). Hysitron TS-75 nanoindenter with a nanoDMAIII module (Bruker) and PICODENTOR HM500 (Fischer Technology) were used to determine the mechanical properties of nanocomposites.

#### 3.2.4. Scanning Electron Microscopy (SEM)

Scanning electron microscope is an imaging technique to study the topography of a sample by scanning the surface with a focused beam of electrons. Modern instruments allow obtaining high-quality images with resolution better than 1 nm and a large depth of field providing near three-dimensional appearance. Typical SEM microscope consists of the electron gun, set of focusing lenses, deflective coils and a special combination of detectors (Figure 26). The electron beam is generated either thermionically or by field emission gun and the electrons are accelerated by high voltage to the energies in the range of 0.2 – 40 keV. Passing through the set of lenses, the beam is focused to a tiny spot of 0.4 – 5 nm in diameter. Subsequently, scanning of the sample is performed by means of pair of deflector plates or scanning coils that allows deflecting of the focused beam in the x- and y-axis. The interaction of highly energetic electrons with surface results in multiple effects: emission of secondary electrons (SE), backscattered electrons (BSE), generation of X-ray radiation etc. A resulting raster image is obtained as a combination of the beam position on the sample surface and the intensity of the acquired signal. The magnification of the image depends only on the scanning area on the sample and is controlled by the amplitude of the beam deflection. The resolution of electron microscopes is limited by the electron wavelength and focusing system producing the electron beam.

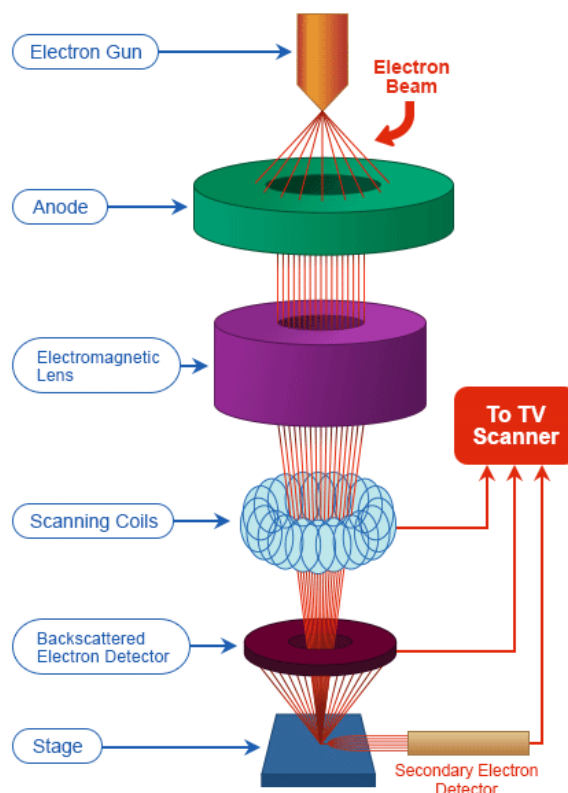


**Figure 26.** Schematic illustration of SEM (adapted from [www.nanoimages.com](http://www.nanoimages.com)).

Probably the most common SEM mode is the detection of secondary electrons ejected from the sample by inelastic collisions with the electron beam. Such electrons have low energy and are able to escape only from the tiny top layer (1-100 nm) of the sample. Thus, images from the SE detector carry detail information about surface topography. In general, the brightness of the image depends on the number of SE collected by the detector. In the case of a flat surface, the incident beam enters the sample perpendicular to the surface and a certain number of secondary electrons are emitted. When rough or tilted surface is exposed to the electron beam, the interaction area increases leading to the higher number of electrons being ejected. Thus, dark spots on the raster image correspond to the smooth surface while brighter spots indicate an increase in roughness.

BSE electrons arise as a result of elastic collisions of incident electrons with the atoms of the studied materials. Such electrons have high energy and could emerge from the inner parts of the sample. This leads to the loss of details of the surface topography. On the other hand, the number of BSE electrons highly depends on the atomic number of the interaction material. Thus, the resulting image can reveal the

distribution of different chemical elements in the sample. The collision cross-section of the nuclei with incident electron is directly proportional to the nuclei size. Hence, materials with higher atomic number generate more BS electrons. The areas with different chemical composition appear in contrast in the image.

Moreover, SEM instruments equipped with energy-dispersive X-ray spectroscopy (EDX) allow identifying the elemental composition and its distribution in the sample. The principle is based on the detection of the characteristic X-ray radiation as a result of electron transitions in ionized atoms. Under the interaction with the beam of highly energetic electrons, the atoms of target material lost the inner-shell electrons forming vacancies. When the vacancy is fulfilled with the electron from the outer-shell, the X-ray radiation is emitted on the characteristic wavelength that is equal to the difference of energy between two shells. Then the radiation is collected by the EDX detector and the intensity and energy of the X-ray radiation are measured. The size of the interaction volume extends from 10<sup>th</sup> of nanometers up to 5  $\mu\text{m}$  depending on the energy of incident electrons and the nature of studied material (Figure 27).

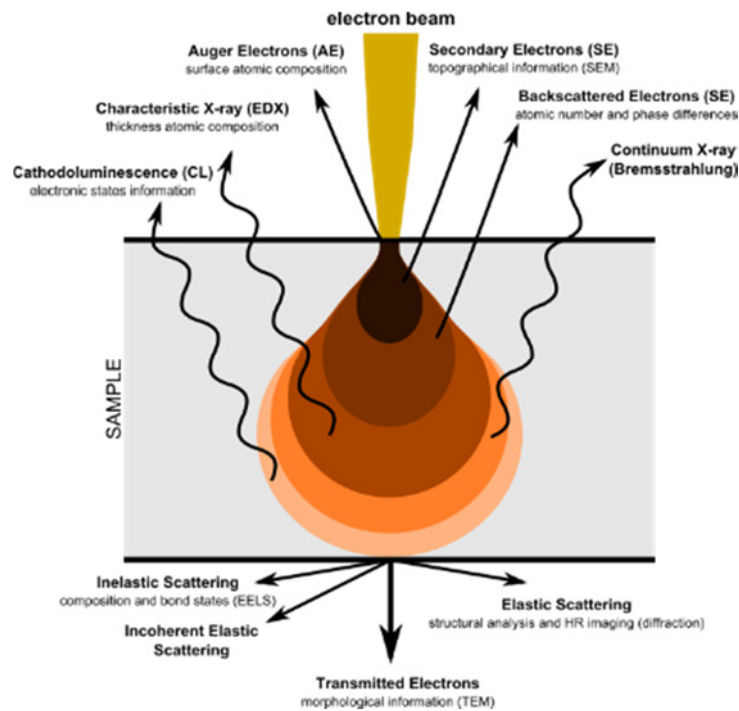


**Figure 27.** Interaction volume electron - matter and the different types of signals which are generated (adapted from phenom-world.com).

The scanning electron microscope (Tescan Mira III) was used to study the topography of prepared samples. The high-resolution images of the surface topography of metal/polymer nanocomposites, metallic and polymeric NPs were obtained by means of secondary electron detector. The BSE detector was applied to determine the spatial distribution of silver NPs in the polymeric matrix. The accelerating voltage was kept at 30 kV in all experiments, except of imaging of the polymeric NPs when 5kV was used. To avoid the charging effect of non-conducting specimens, viscose fabric and C:H NPs were coated with Pt thin film prior to the measurements. Solarius Particles software was utilized to evaluate the size distribution of NPs from SEM images.

### 3.2.5. Transmission Electron Microscopy (TEM)

Transmission electron microscopy (TEM), the first of electron microscopies developed in 1931, is a microscopy technique using a beam of electrons to obtain a high-resolution image of the specimen. The image is created when the electrons are transmitted through the sample. With a wavelength much less than that of visible light, TEM allows to obtain images with much higher resolution, so that the visualization of the atoms could be achieved. Since TEM operate at high voltage (100-300 kV) the ultra-high vacuum of the chamber should be provided. Also, the thickness of the sample should be less than 100 nm to provide its transparency to the beam of electrons. The ability of electrons to penetrate the matter decreases with the atomic number squared. Thus a specific thickness is necessary for different materials and the preliminary preparation may be needed.

Transmission electron microscope (TEM, Jeol 2200FS) equipped with Centurion Large Angle SDD-EDX detector was used to determine size and crystal structure of copper NPs. The samples were prepared on copper grids coated with a lacey or holey carbon film (SPI and Agar Scientific). High-resolution TEM images were analyzed by means of the free access software ImageJ.

### 3.2.6. X-Ray Photoelectron Spectroscopy (XPS)

X-ray photoelectron spectroscopy, known also as an Electron Spectroscopy for Chemical Analysis (ESCA), was introduced by Swedish physicist Kai Siegbahn in 1960s [112]. This technique uses monochromatic radiation in the x-ray range to generate photoelectrons which are then analyzed by their energy. XPS allows to determine the elemental composition, empirical formula of material as well as analyze the chemical or electronic state of the elements.

In a simplified representation, XPS consists of the X-ray source, electron optics, hemispherical analyzer, electron detector and UHV chamber. The operation principle could be explained as follow (see also Figure 28). The sample placed on the substrate holder is irradiated with monochromatic X-rays beam (typically, Al  $K\alpha$  [1486,7 eV] or Mg  $K\alpha$  [1253.6 eV]). The interaction of the photons with the specimen leads to the photoelectric effect when atoms lose electrons from the core levels. Such photoelectrons are emitted from the sample surface with characteristic kinetic energy ( $KE$ ):

$$KE = h\nu - BE - f \quad (13)$$

where  $h\nu$  is the energy of the incident photons,  $BE$  is the binding energy of the electron and  $f$  is a work function of the spectrometer.

The energy distribution of the electrons is measured by electron analyzer. It consists of electron optics which collects the electrons from the sample, retarded and focused them to the entrance slit of the hemispherical analyzer (HAS). Then the electrons with specific energy (pass energy) can pass through the HAS and reach the electron detector. This operation regime is known as a fixed analyzer transmission mode (FAT) and is the major mode for XPS operation. The pass energy for HAS is an important acquisition parameter, that determines the energy resolution and intensity of the acquired spectra. Increase in the energy of impinging electrons to the detector (i.e. higher pass energy) leads to the high increase in the signal/noise ratio but to the decrease of the spectral resolution. Therefore high pass energy is used for the acquisition of a wide spectrum where the high intensity is necessary for easy and fast

peak identification while low pass energy is used for measurement of high-resolution spectra in order to reach better spectral resolution.

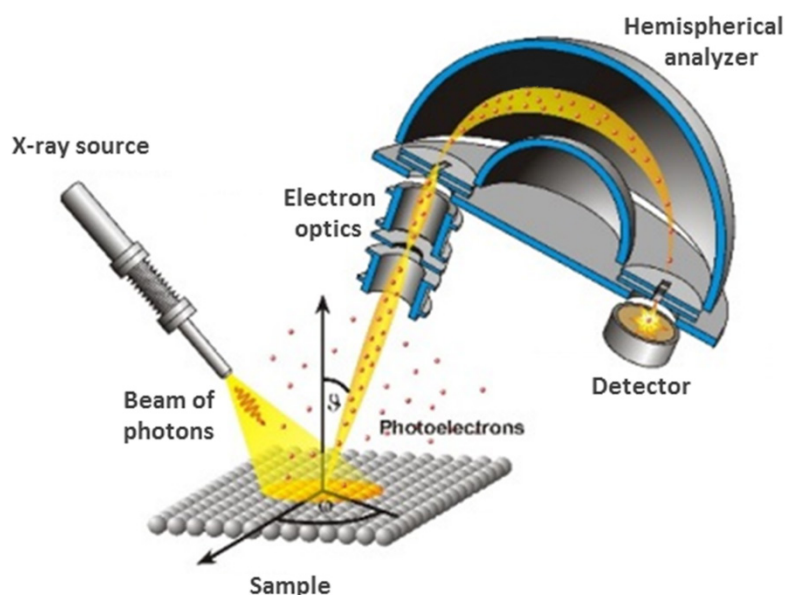


**Figure 28.** Schematic representation of the XPS (adapted from jacobs.physik.uni-saarland.de).

Quantitative information could be obtained by analyzing the position, width and specific area of the individual peaks of XPS spectra. To obtain an atomic percentage of elements within the measured material, the signal intensity (peak area) is always normalized by a relative sensitivity factor (RSF) that takes into account the probability of photoelectric effect for each chemical element.

XPS is a surface sensitive technique, i.e. photoelectrons without loss of the energy can escape from the top 1-10 nm of the material. The depth of analysis is determined by the inelastic mean free path ( $\lambda$ ) of the photoelectron in the material. Basically, 63 % of photoelectrons arise from one  $\lambda$  of depth, whereas 95 % of photoelectrons come from  $3 \lambda$ .

The emission of electrons from the surface, for example in insulator materials, can lead to the deterioration of the electrons resulting in an excessive positive charge at the surface. Consequently, the measured spectra appeared to be shifted to the region of higher BE. A special software processing tools are used to remove this shift.

The chemical composition of the selected samples was determined by X-ray photoelectron spectrometer equipped with X-ray source XR 50 (Al  $K\alpha$  1486.6 eV, Specs) and hemispherical electron analyzer Phoibos 100 (Specs). Wide spectra were

acquired for binding energies in the range of 0-1100 eV with pass energy 40 eV and energy step 0.5 eV. High resolution spectra were acquired with pass energy 10 eV and energy step 0.1 eV. Charging of acquired spectra was calibrated using C 1s peak with the position of 285 eV for C-C bonds. The data were processed using Casa XPS software.

### 3.2.7. Fourier Transformer Infrared spectroscopy (FTIR)

FTIR in so called attenuated total reflectance (ATR) mode is a technique utilizing the property of disturbed total internal reflection to study both liquid and solid specimens by infrared spectroscopy (IR or FTIR). In general, the evanescent wave occurs on the boundary of two materials with different refractive indexes. Schematically it could be represented by Figure 29 where the infrared beam is directed on the ATR crystal with high refractive index. Passing through the crystal under a certain angle, IR beam experienced multiple internal reflections leading to the formation of the evanescent wave on the boundary of the crystal and sample. Such a wave propagates beyond the crystal and extends a few micrometers (0.5-5  $\mu\text{m}$ ) into the sample. Depending on the nature of the studied material, the evanescent wave is attenuated in regions of the infrared spectrum where the sample absorbs energy. Subsequently, the altered IR beam is collected by a detector after exiting the crystal and infrared spectrum is generated.

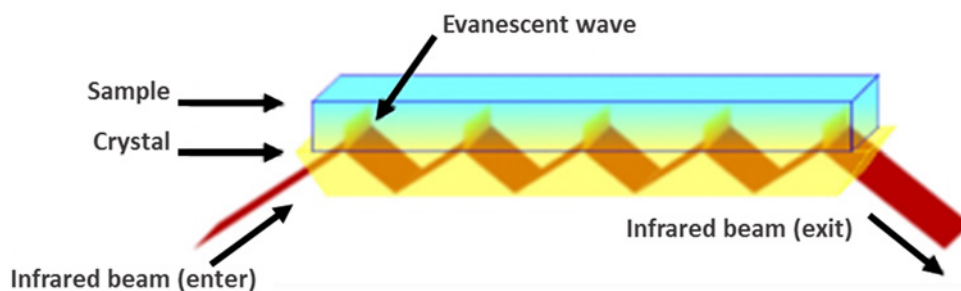


**Figure 29.** Schematic representation of the total internal reflection principle applicable in ATR.

Herein, ZnSe single ATR was used to determine water content in the collected oil after the water-oil separation process. Such an approach enables measurement of

the collected oil directly after the squeezing process without any prior preparation. Absorbance spectra were acquired in the range of 4000 – 600  $\text{cm}^{-1}$  with 64 scans and resolution 4  $\text{cm}^{-1}$ .

### 3.2.8. Ultraviolet-Visible Spectrophotometry (UV-Vis)

Ultraviolet-visible spectrophotometry belongs to the family of absorption spectroscopies and it is widely used in chemistry, biology and physics to determine the concentration of the absorbing material in a solution. The main principle is based on the study of electronic transitions when the low energy radiation interacts with specimen. Energy absorption is due to excitation of the electrons from ground states to higher excited states. In practice, light in the ultraviolet and visible regions of the spectra is passing through the sample and the transmittance (T) is measured as the ratio of the intensities of light after (I) and before ( $I_0$ ) passing through the sample as a function of a wavelength.

Applying simple mathematical transformation, UV-vis spectra could be expressed through the absorbance  $A = -\log_{10}(T)$  – a dimensionless quantity that measures the attenuation of light passing through the material. Absorbance can be caused by various physical processes including absorption, scattering, reflection etc. According to the Beer-Lambert Law, the absorbance of the sample (A) is directly proportional to the concentration of included absorber (c) and subsequent quantitative analyze could be easily performed as follows:

$$A = \log_{10} \left( \frac{I_0}{I} \right) = \epsilon lc \quad (14)$$

where  $l$  is path length through the sample,  $\epsilon$  - extinction coefficient of the material,  $I_0$  and  $I$  is the intensity of light before and after transmission through the sample.

Double Beam UV-Vis spectrophotometer (Hitachi U-2900) with wavelength range of 190 nm to 1100 nm was used as an easy and rapid method to monitor the number of metallic nanoparticles incorporated into the polymeric matrix during the nanocomposites preparation. Scanning over the range of wavelengths allows

identification of so-called surface plasmon resonance – a rapid oscillation of conductive electrons that appears at the interface of materials with different permeability (conductor/dielectric) under the light excitation. When the frequency of incident light matches the frequency of oscillating electrons, an abrupt absorption of the light occurs at certain wavelengths. The higher number of metallic NPs in nanocomposite structure, the stronger absorption peak could be detected. UV-Vis spectrophotometry was also applied to determine the concentration of the residual oil or water in the collected aliquots after the separation of a mixture of water with either light or heavy oil (see more in the section 3.3.3).

### 3.2.9. Spectroscopic Ellipsometry

Spectroscopic ellipsometry is a contact-free method widely used to determine optical constants and thickness of thin films. The technique can also bring further information about the specimen related to optical properties: composition, roughness, crystallinity etc. The main principle is based on measurements of changes of polarization state of light after the refraction from the material being investigated. The measured signal is given by the amplitude ratio of s and p polarized components ( $\tan \Psi$ ) and their phase shift ( $\Delta$ ). Both ellipsometric parameters depend on the optical properties of the material as well as its thickness.

The ellipsometry is indirect method, thus the collected data should be fitted according to the constructed model to obtain optical constants and thickness of the sample. For example, the refractive index ( $n$ ) and extinction coefficient ( $k$ ) can be estimated using the Cauchy relationship with free parameters.

In this study, spectroscopic ellipsometry (Woollam M-2000DI) was utilized to determine the thickness of the plasma polymer films (a-C:H, (C:H)SiO<sub>x</sub>, SiO<sub>x</sub>). The measurements were performed with a variable incidence angle ( $55 - 75^\circ$ ) and wavelength range  $\lambda = 192-1690$  nm. The coatings were deposited on one side polished silicon wafer in all experiments to provide the excellent refractive properties of the substrate. The ellipsometric data were fitted using a CompleteEASE software (J.A. Woollam) according to Cauchy model for Si substrate with 1.5 nm of native oxide.

### 3.2.10. Measurements of wettability

Considering a thermodynamic equilibrium in the three-phase solid-liquid-air interface, the wettability of a flat substrate by a liquid could be described by the Young equation. It claims that a single sessile drop placed on the solid will take the most energetically favorable shape with a characteristic contact angle (CA). Such a CA serve as an indicator of the wettability – the tendency of the liquid droplet spread out over the flat solid surface. The contact angle below  $90^\circ$  means that the surface tend to be easily wet with liquid, whereas  $\theta > 90^\circ$  indicates that wetting is unfavorable. For water, the surfaces with the above-mentioned characteristics refer as hydrophilic and hydrophobic and typically correspond to the materials with high and low surface free energy, respectively.

To obtain materials with an extreme wettability, whether superhydrophobic or superhydrophilic, a proper roughening of the surface should be provided. It is well known that micro- and nanostructured surfaces contribute to hydrophobicity in the case of hydrophobic materials and enhance wettability for hydrophilic one, as shown in Figure 30. Wetting behavior of such rough materials could be explained by two separate models: Wenzel's [113] (equation 15) and Cassie-Baxter's [114] (equation 16).

$$\cos(\theta^*) = r \cos(\theta) \quad (15)$$

where  $\theta^*$  and  $\theta$  are the equilibrium and Young water contact angles respectively,  $r$  is roughness ratio, that is define as the ration of true area of the solid surface to the apparent area.

$$\cos(\theta^*) = r_f f \cos(\theta) + f - 1 \quad (16)$$

where  $\theta^*$  and  $\theta$  are the equilibrium and Young water contact angles respectively,  $f$  is the area fraction of the surface, which is in contact with water,  $r_f$  is roughness ratio of the wet surface area.

According to Wenzel's model, the liquid could partly penetrate inside the surface irregularities forming a large contact area with solid, whereas Cassie-Baxter's model assumes that the water sits on the top of the protrusions keeping the air trapped underneath the drop.

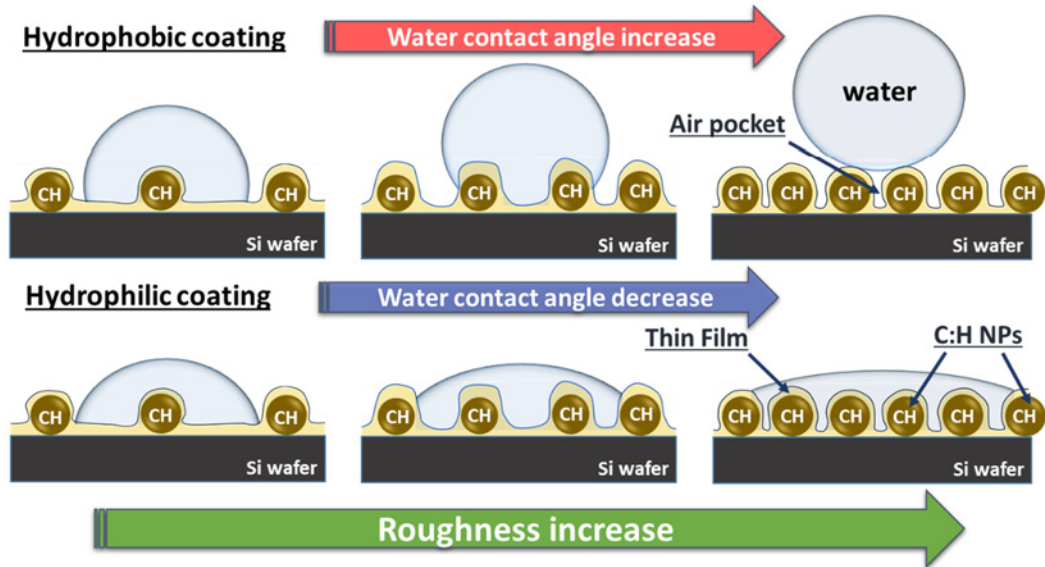


**Figure 30.** Schematic representation of the wetting behavior of materials in dependence on the surface roughness (upper Fig. central corresponds to Wenzel and upper right Cassie-Baxter wetting regime).

The above-mentioned statements are applicable to explain the underwater superoleophobicity or underoil superhydrophobicity. The general mechanism was proposed for the first time by Jiang et al. investigating the phenomenon that materials hydrophilic in air exhibit oleophobic properties in water. In their study, existing models were generalized for the solid-liquid<sub>1</sub>-liquid<sub>2</sub> interface when the air phase is replaced by second liquid (see Figure 31) [115]. The contact angle of oil in water on a flat solid substrate was derived through Young's equation as follows:

$$\cos\theta_{OW} = \frac{\gamma_{OA}\cos\theta_O - \gamma_{WA}\cos\theta_W}{\gamma_{OW}} \quad (17)$$

where  $\theta_{OW}$  is the contact angle of oil in water,  $\gamma_{OA}$ ,  $\gamma_{WA}$ , and  $\gamma_{OW}$  are the interfacial tensions of oil-air, water-air and oil-water interfaces,  $\theta_W$  and  $\theta_O$  are intrinsic water and oil contact angle in air.

For rough surfaces, underwater or underoil contact angles could be calculated by means of the derivatives of Wenzel and Cassie-Baxter models. For example, the contact angle of an oil droplet in the water on a slippery surface could be expressed through underwater Cassie-Baxter equation:

$$\cos\theta_{OW'} = f\cos\theta_{OW} + f - 1 \quad (18)$$

where  $\theta_{OW'}$  is the contact angle of an oil droplet on a rough surface in water,  $f$  is the area fraction of the surface, which is in contact with oil,  $\theta_{OW}$  is the underwater intrinsic contact angle of the oil.

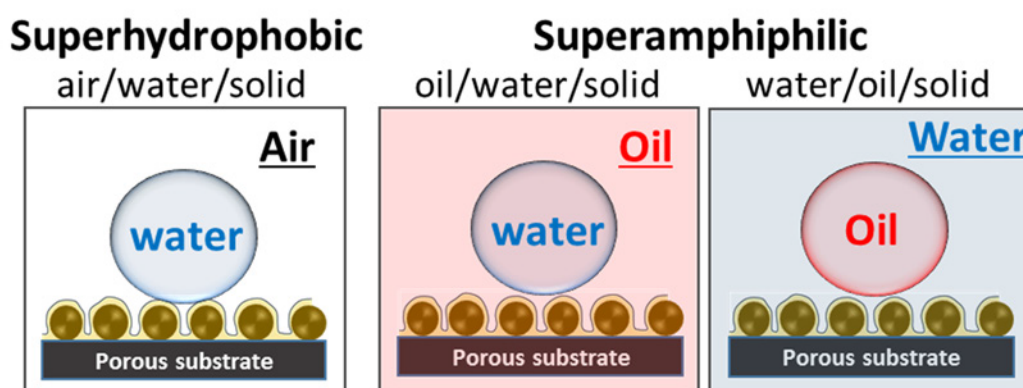


**Figure 31.** Schematic representation of the Cassie-Baxter wetting behavior in the air (left), underoil (center) and underwater (right).

The static and dynamic water contact angles for deposited coatings were evaluated using the goniometer of custom construction. Contact angles are given as the average of 3 measurements at the room temperature and the drop size was  $\sim 2 \mu\text{l}$ . In the case of filtration membranes, underwater and underoil CA were determined by immersion of the membrane into the Petri dish filled with oil or water respectively. Subsequently, the oil or water droplet ( $\sim 2 \mu\text{l}$ ) was introduced into the surface of the membranes.

### 3.2.11. Antibacterial properties

*Colony Forming Units (CFU).* Selected samples of nanocomposites (Ag/a-C:H) were studied for the antibacterial activity. The glass disks (12 mm in diameter) coated with nanocomposite films were incubated with 3 ml of bacterial suspension (*Escherichia coli* in Phosphate Buffered Saline (PBS),  $1.5 \times 10^6$  CFU\*ml<sup>-1</sup>) for 3h at 37 °C with shaking (150 rpm). Afterward, the aliquots of bacterial suspension were properly diluted, plated on Luria-Bertani agar plates and incubated for 24 h at 37 °C. The number of grown bacterial colonies was subsequently counted and a number of colony forming units was calculated. Uncoated glass discs were employed as a negative control. All tests reported here were performed in three replicas and the values are presented as means of these three independent measurements.

*Metabolic activity.* The metabolic activity measurements were applied to evaluate the antibacterial activity of the functional nanocomposite coatings against gram-negative bacteria *Escherichia coli* (*E.coli*). Initially, the bacteria culture was diluted in PBS with 1% Luria Broth to a concentration of 10<sup>4</sup> bacteria per ml. Then the triplicates of bare viscose fabric and viscose treated with superhydrophobic and superamphiphilic nanocomposites (1×1cm) were placed into a 12-well plate, where the aliquots (1ml) of suspension were added and incubated at 37°C. After 0, 1, 3 and 24 h of the incubation period, 100 µl of bacterial suspension was transferred and analyzed by alamarBlue (Thermo Fisher Scientific) – a viability cell indicator. Upon the interaction with living bacteria, the reagent with active component resazurin reduced to the fluorescent molecule resorufin. Thus the intensity of the produced fluorescent signal is quantitatively proportional to the number of metabolically active bacteria.

### 3.3. Oil/water separation

#### 3.3.1. Materials

Non-woven viscose fabric (PERVIN/PERLAN, weight 80 gm-2) was purchased from VYROUBAL TEXTILES s.r.o. (Czech Republic). Carbon cloth (45356 Toray Carbon Paper, TGP-H-60) was received from Alfa Aesar. The samples with size of 20 × 70 mm were used. Mixture of deionized water with different oils was used in all experiments. For simplicity, the term ‘oil’ will be used further in the text with respect to all non-polar organic liquids used in the separation experiments.

Diiodomethane, Oil Red O, methylene blue, sodium dodecyl sulfate, n-hexane, hexamethyldisiloxane (HMDSO) were obtained from Sigma-Aldrich. Silicone oil (705CA) was purchased from Kurt J. Lesker Company. Sunflower oil and benzene were received from local suppliers.

#### 3.3.2. Selective absorption

Collection of the oil spills from water was performed by the immersion of the superhydrophobic (C:H)SiO<sub>x</sub>/C:H/Cu membrane into the vessel with immiscible water/oil mixture. For better visualization, oil was dyed red (Oil Red O) and water was colored in blue (methylene blue). After the absorption process, the oils were collected from the membrane by a mechanical squeezing process. Between all separation cycles, membranes were washed with ethanol and dry for 60 minutes in air under room temperature. The absorption capacity of the membranes was defined through the equation:

$$\frac{m_{saturated} - m_{initial}}{m_{initial}} \quad (19)$$

where  $m_{initial}$  and  $m_{saturated}$  is the weight of the membrane before and after the collection process.

Weighing of the samples was done by Sartorius CP225D microbalance. FTIR-ATR using ZnSe crystal with single reflection was utilized to determine water content in the collected oil. Absorbance spectra were acquired in the range of 4000 – 600 cm<sup>-1</sup> with 64 scans and resolution 4 cm<sup>-1</sup>.

### 3.3.3. Separation of water/oil mixture

The mixture of water and oil (sunflower oil, benzene, n-hexane, diiodomethane) with a weight ratio 1:1 was used in separation experiments. The filtration was performed using a simple separation setup consisting of a glass tube connected to the membrane and was completely driven by gravity. Prior to the separation, Carbon/SiO<sub>x</sub> membrane was pre-wetted with water or heavy oil for separation of light oil/water and heavy oil/water mixture respectively. Thus in the case of water removal, oil was dyed in red (Oil Red O) and during heavy oil removal, water was colored in blue (Methylene Blue). The filtration was started by pouring the mixture into the separation setup. Since Oil Red O and Methylene Blue dye have characteristic absorbance peak in the visible range of spectra, the concentration of the residual oil or water in the collected liquids was determined using UV-Vis spectrophotometer (Hitachi U-2900) according to Beer's law. Prior to the measurements, 0.5 mg of sodium dodecyl sulfate (SDS) per 1 ml of filtrate was added as an emulsifier. Subsequently, advanced vortex mixer (VELP Scientifica) was applied for 1min (3000 rpm) to ensure uniform distribution of the contaminant in the collected filtrate. Subsequently, the separation efficiency was calculated as follows:

$$\left(1 - \frac{C_f}{C_m}\right) 100\% \quad (20)$$

where  $C_m$  is the initial concentration of the oil in the mixture and  $C_f$  is the oil concentration in the filtered water. The average value was calculated on the bases of 10 separation cycles.

## 4. Results and Discussion

The Result and Discussion chapter of the thesis is organized in the following manner: first, optimization of the deposition process of metallic nanoparticles in GAS and the effect of magnetic field on the formation and growth mechanisms of Cu NPs were investigated; then, metal/polymer nanocomposites were fabricated and the effect of three different plasmas on the chemical composition, morphology and antibacterial properties of one was studied; finally, superhydrophobic and amphiphilic nanocomposite coatings were introduced on the porous textiles and were used as filtration membranes for the water purification needs.

### 4.1. Optimization of the deposition process of Cu NPs.

This chapter of the thesis is based on the scientific results that were already published in the paper entitled “*Effect of magnetic field on the formation of Cu nanoparticles during magnetron sputtering in the gas aggregation cluster source*”, cited as M. Vaidulych, J. Hanuš, J. Kousal, S. Kadlec, A. Marek, I. Khalakhan, A. Shelemin, P. Solař, A. Choukourov, O. Kylián, H. Biederman, *Plasma Process Polym.*, **2019**, e1900133, <https://doi.org/10.1002/ppap.201900133>.

Fabrication of the functional nanocomposite coatings by the combination of GAS and plasma polymerization process requires a well-established and stable in the time deposition process of nanoparticles. To meet these criteria, the formation and growth mechanisms of Cu NPs were studied in dependence on the working parameters in the aggregation source. In-depth investigation of the influence of the adjustable magnetic field (MF) on the deposition process of NPs is presented as well.

#### 4.1.1. Magnetic field optimization.

In this study, a gas aggregation source (the similar one as described in the Experimental section 3.1.3) was used with the specially constructed magnetron that allows adjustment of the magnetic field above the target surface. Variation in the MF was realized through the mechanical displacement of the magnetic circuit from 0 to 6 mm position that corresponds to the intensities of the magnetic field in the range of 83 – 35 mT above the target surface (see Figure 19).

The configuration of magnetic circuit made of permanent magnets was developed to provide the invariable shape of the magnetic force lines for given positions of the magnetic circuit. Thus the design by HVM Plasma ltd. was optimized to keep a constant position of the racetrack while varying the magnet-to-target distance (intensity).  $B_x$  (parallel) and  $B_z$  (perpendicular) components of the magnetic field across the target surface were evaluated experimentally by means of magnetometer Elimag MP-1 (Figure 32). Left graph represents  $B_x$  component for selected distances of the magnetic circuit from the target. It passes through the maximum at radius 22 mm from the magnetron center (0 mm position). The normal component  $B_z$  in Figure 32b for all positions of the magnetic circuit changes its orientation at the radial position of 23 mm. This corresponds to the region where the magnetic field lines are nearly parallel to the magnetron surface. This is the region with the highest electron confinement which defines a position of the circular erosion track on the target.

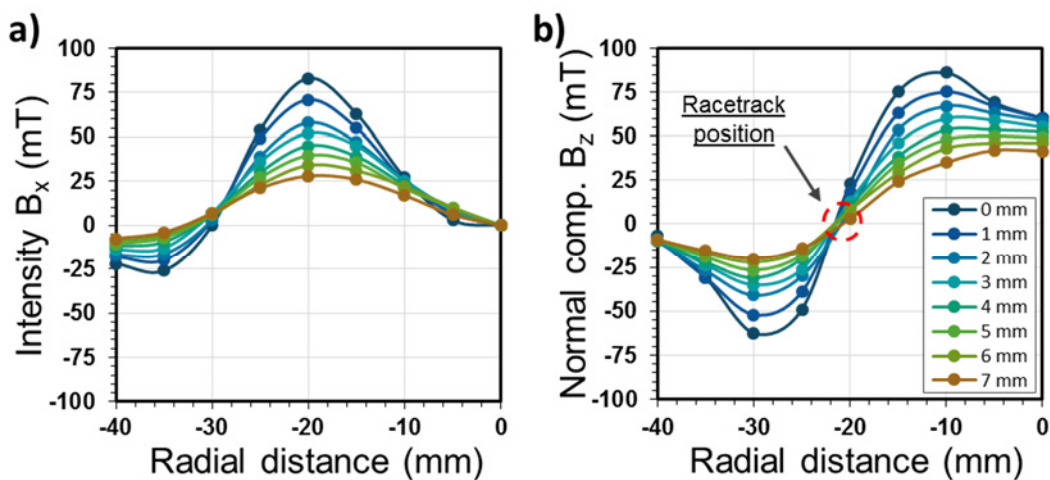


**Figure 32.**  $B_x$  (a) and  $B_z$  (b) components of the magnetic field as a function of the probe position on the magnetron surface.

Photographs of the magnetron discharge (Figure 33a) show that the employed magnetron is well balanced and the shape of the plasma is well-defined and does not change with increasing magnet-to-target distance while the intensity of the discharge is decreasing. To minimize the effect of the erosion track on the deposition parameters in GAS, experiments for a given position of the magnetic field was starting with a new Cu target.

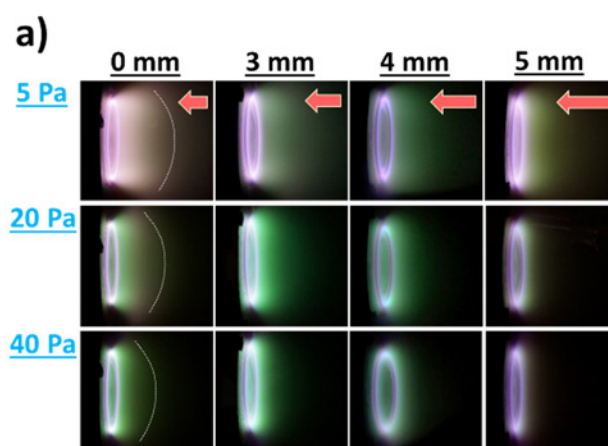


**Figure 33.** Photographs of the magnetron discharge operated at magnetron current 50 mA at different Ar pressures and distances of the magnetic circuit form the target.

#### 4.1.2. Deposition rate and size distribution of nanoparticles

The deposition rate of Cu NPs is presented in Figure 34 as a function of the magnetron current and pressure in the GAS for the strongest MF of 83 mT (0 mm magnet-to-target distance). The deposition rate of the NPs increases monotonously with the current, whereas it passes through a maximum with pressure (see the insert graphs in Figure 34). The maximum value of the deposition rate was reached at the pressure of 40 Pa and the magnetron current of 500 mA. The NPs with a relatively narrow log-normal size distribution were obtained over the entire range of the deposition conditions used in this study. The size of NPs remains invariable with the current (under the constant pressure) and size averages were  $21 \pm 5$  nm (Figure 35a). However, the variation of the pressure affects the NPs size so that larger NPs were synthesized at a lower pressure (Figure 35b). These results are in good agreement with our previous studies [50,116].

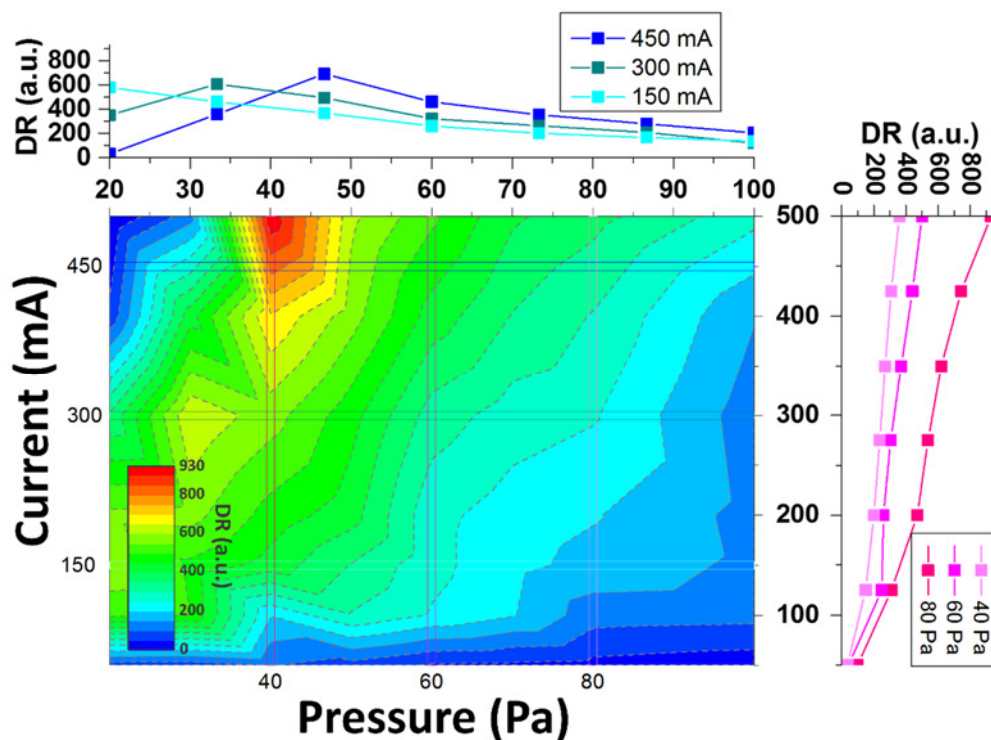


**Figure 34.** Dependence of the deposition rate on the pressure and current in the GAS for 0 mm position of the magnetic field (MF 83 mT).

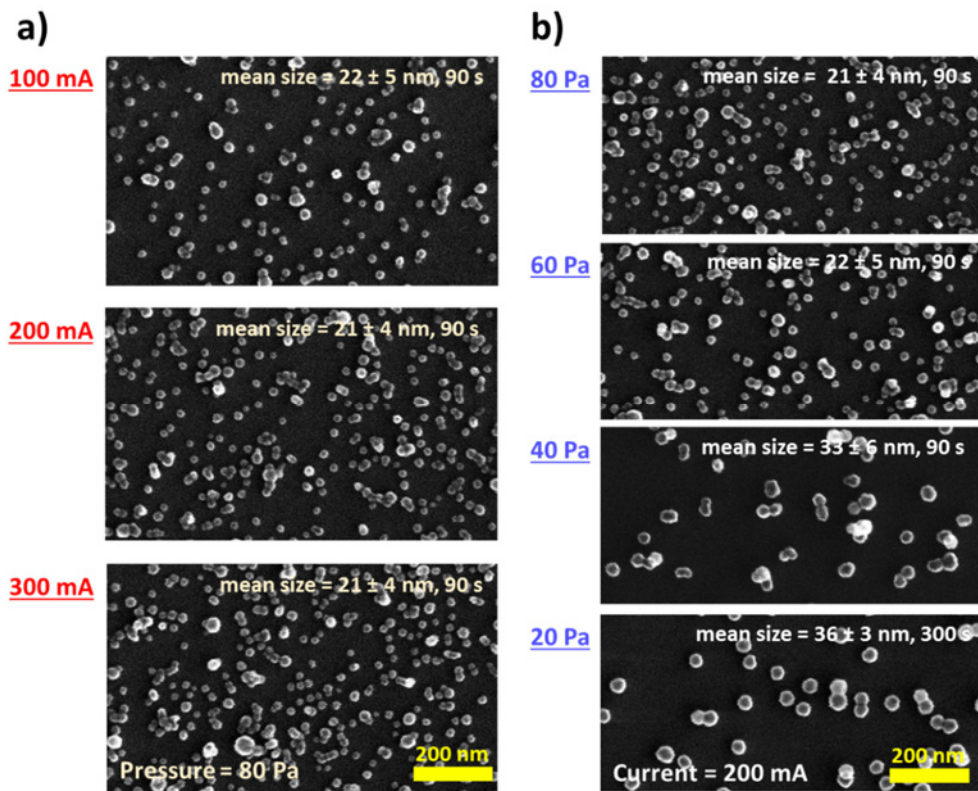


**Figure 35.** SEM images of the Cu NPs prepared at different: (a) currents and (b) pressures.

The influence of the intensity of the magnetic field on the formation of the NPs was studied by changing the magnet-to-target distance from 0 to 6 mm. According to Figure 36, DR is strongly dependent on the magnitude of the magnetic field. The maximum of DR is at smaller magnetic circuit displacement reached at the highest studied magnetron current – 500 mA. A decrease of magnetic field shifts the maximum of DR to higher pressures. The total maximum of the DR was reached at the position of 4.0 mm (45 mT) but in this case the magnetron current had to be decreased to 400 mA. Further displacement of the magnetic circuit (decrease of the intensity of the magnetic field) results in the reduction of DR. At 4.5 mm displacement the maximum was found similarly to the previous case at 100 Pa but at the magnetron current 300 mA. From Figure 36 is obvious that at this magnetic circuit position another region exists at lower pressures and magnetron currents where the deposition takes place. In this region the NPs deposition was observed in case of 5 mm displacement and the maximum was reached at 40 Pa and 100 mA. The formation of NPs completely stops with the magnet-to-target distance of 6 mm. For better representation, in Figure 37 the deposition rate for the conditions marked in Figure 36 by black squares (maximal deposition rate for the given magnet-to-target distance) and red circles (40 Pa, 200 mA) is presented as a function of the position of the magnetic circuit.

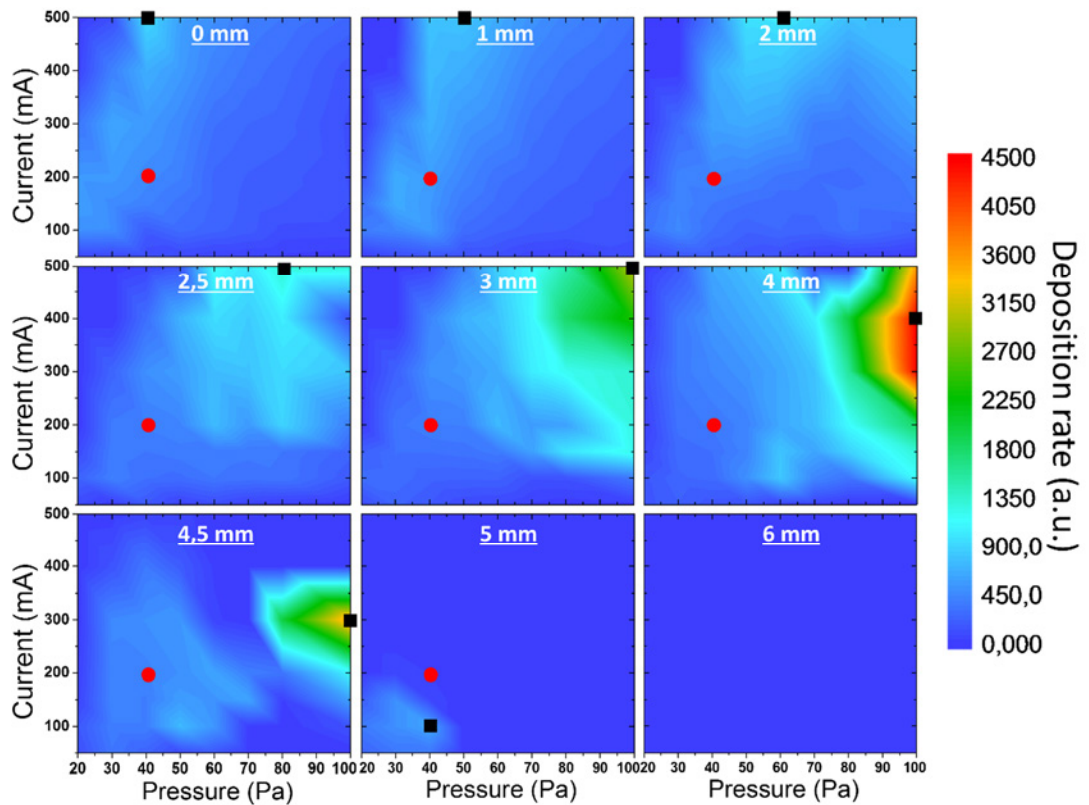


**Figure 36.** Dependence of the DR of Cu NPs on the magnetron current and pressure for the given positions of the MC. Round and square designations correspond to two sets of the deposition condition under which SEM images were taken: constant pressure and current (round), and in the region of the maximum DR (square).

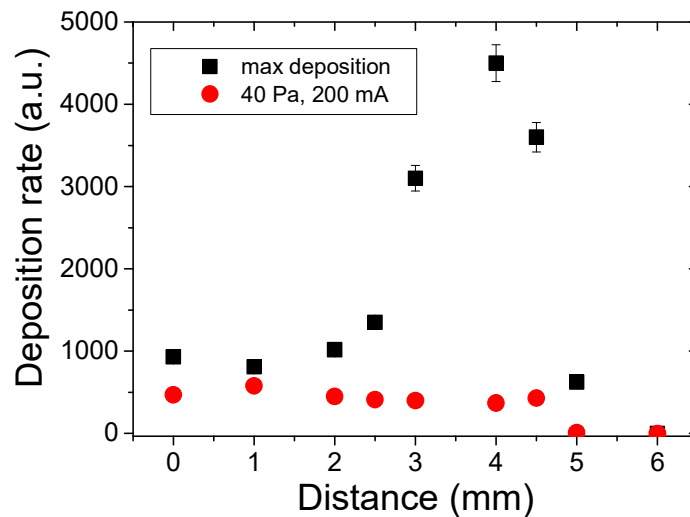


**Figure 37.** Deposition rate in dependence on the magnets displacement for two set of deposition conditions as shown in Figure 36.

The intensity of the magnetic field determines the efficiency of the electron confinement in the plasma tunnel and, hence, the efficiency of sputtering. The optical emission spectra were acquired for three positions of the magnetic circuit corresponding to the highest intensity of the magnetic field (0 mm), the highest DR (4.0 mm) and the highest displacement at which the deposition was still possible (5.0 mm). Figure 38 shows the color maps of the intensity of the Cu line at  $\lambda = 353.03$  nm normalized to the emission line of Ar at  $\lambda = 826.45$  nm. As expected, the emission from copper atoms decreases with decreasing strength of the magnetic field, reflecting the worse electron confinement in the plasma tunnel and, as a consequence, the less intensive sputtering. It can be also noted that the maximum of the atomic Cu emission is shifted to lower pressure as opposed to the DR which is maximized at higher pressures (Figure 36). The phenomenon is readily explained by the inefficient NPs formation at reduced pressures given by the insufficient gas cooling and low probability of 3-body collisions necessary for the formation of NPs seeds. Thus, most of the copper in the gas phase at lower pressures remains in the atomic form and the relaxation of the excited Cu atoms contributes to the intensive optical emission. In contrast, the nucleation of the atomic Cu vapors starts to dominate at higher pressures leading to an increase of the nanoparticle deposition rate concomitant with an attenuation of optical emission.

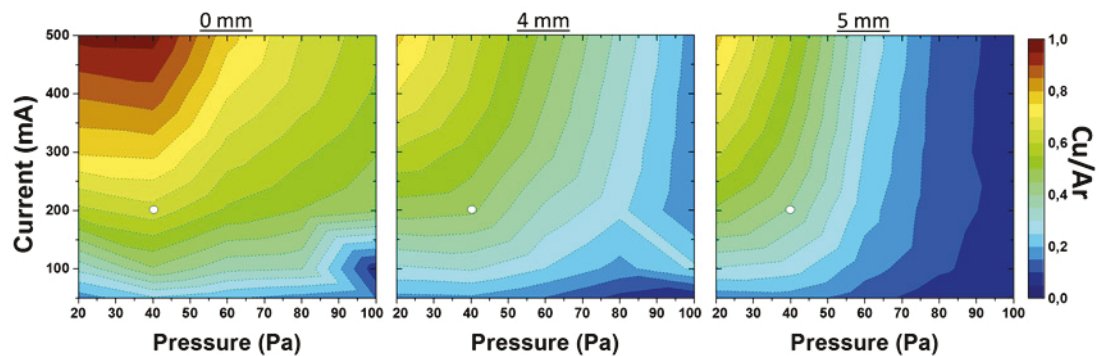


**Figure 38.** The relative density of Cu atoms in plasma as a function of the current and pressure for given positions of the magnetic circuit.

In Figure 39, SEM images of Cu NPs prepared at different positions of the magnetic circuit are presented for two sets of the deposition conditions: under constant pressure (40 Pa) and current (200 mA), and for the conditions that for given magnetic field intensity provided the maximum deposition rate (different pressures and currents, marked by the black squares in Figure 36). The pressure 40 Pa and current 200 mA were chosen as the common conditions for the stable production of NPs of noble metals in the configuration of our GAS.

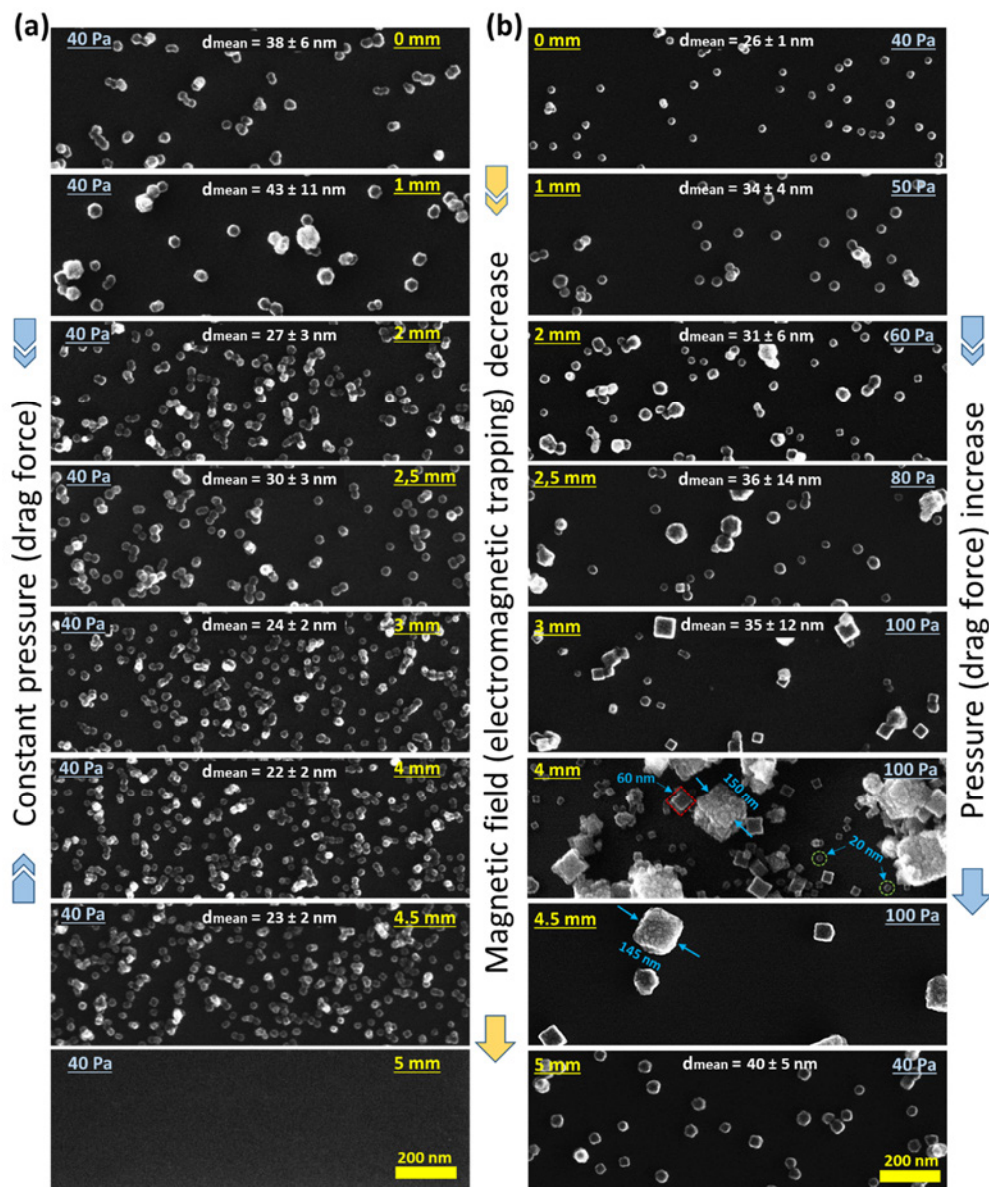


**Figure 39.** SEM images of Cu NPs prepared for two sets of the deposition condition in GAS: (a) under constant pressure and current, and (b) in the region of the max. DR (see corresponding designations in Figure 36) for given positions of the mag. circuit.

In the case of the constant pressure and current, spherical NPs are obtained for all the positions of the magnetic circuit (Figure 39a). The average size of the NPs varies in the range of 20-30 nm with slightly larger particles for the magnet-to-target distances 0 and 1 mm.

In turn, under the conditions where the maximum of the DR took place, SEM images revealed a strong correlation in the size and shape of NPs with alteration in the intensity of the MF (Figure 39b). We obtained spherical, cubic and more complex agglomerated NPs in a wide range of sizes (10 - 150 nm), while the size distribution was changed from the unimodal to bimodal and even multimodal. In the positions of 0 and 1 mm, nanospheres with narrow size distribution were obtained similarly to our previous results. Further displacement to 2 and 2.5 mm resulted in bimodal size distribution with the majority of nanoparticles having the size of  $26\pm 1$  nm together with a small amount of larger (about 50 nm in diameter) spherical NPs. A rather multimodal size distribution with large cubic and small spherical NPs was obtained in the 3 mm position. In 4 mm position nanospheres and nanocubes were accompanied by huge agglomerated NPs up to 150 nm in diameter. The biggest agglomerates seem to be large cubes decorated by small spherical NPs. The deposition rate of the NPs was observed to be the highest at this magnetic circuit position. It was about 5 times higher than the maximum deposition rate at the strongest magnetic field, i.e. at 0 mm position (Figure 39b). Further displacement of the magnetic circuit to 4.5 mm and a decrease of magnetron current to 300 mA led to the deposition of quite large cubic nanoparticles without the presence of smaller spherical NPs. As already written, further displacement to 5 mm led to the strong decrease of maximum DR (40 Pa, 100 mA) and only spherical NPs were found.

The changes in the shape of the NPs can be explained according to Zhao et al. by the different energetic conditions and atomic deposition rate in the GAS [117]. Spherical nanoparticles are formed in the so-called high deposition or high mobility regime. The mobility of the ad-atoms in the high deposition regime is negligible as compared to their deposition rate on the surface of the growing NP. If the growth of the NP is isotropic, which can be expected at the pressure of tens of Pa, then spherical nanoparticles are formed. On the contrary, high mobility regime means that the mobility of ad-atoms is high enough on all atomic planes with respect to their deposition rate that again results in the formation of spherical NPs. It is beyond our

ambitions to rigorously distinguish if the spherical NPs were formed in high deposition or high mobility regime. However, our recent study performed using the similar configuration of the magnetic circuit showed that the overall energy flux on the NP surface increases nearly exponentially with a pressure decrease [118]. If we take into account the low deposition rate of the ad-atoms, at least for the highest magnetic circuit displacement, it can be concluded that the NPs were formed in a high mobility regime. In contrast, the cubic nanoparticles are formed under energetic conditions that represent the optimum ratio between the deposition rate on the growing surface of NP and ad-atoms mobility (their diffusion rate). In this situation, the dominant role is played by differences in the mobility of ad-atoms on different atomic plains that leads to the formation of the cubic NPs [117].

Another question arising from the SEM images is the enormous size of the cubic nanoparticles. The presence of big nanoparticles in the deposit is usually explained by the coalescence of small nanoparticles. Here, it is necessary to distinguish two different scenarios. First, the coalescence at low temperature leads to the formation of aggregates where both the size and shape of individual nanoparticles are preserved. Second, at high temperature the individual NPs are melted and a larger spherical nanoparticle is formed. It is thus obvious that none of those cases can explain the formation of large cubic nanoparticles. The origin of the big cubic NPs can be, however, explained by another phenomenon: trapping of the NPs close to the magnetron.

The phenomenon of NPs trapping was experimentally demonstrated in our recent study of in-situ growth of the Cu NPs by Small Angle X-ray Scattering (SAXS) [119]. The in-situ SAXS measurements were conducted in the GAS where the formation and growth of Cu NPs took place [119]. It was found that two main populations of NPs could be distinguished in the close vicinity to magnetron target. Small NPs 10 - 20 nm in diameter, actually those that were deposited onto the substrate, and the second population of NPs around 90 nm in diameter that were preferentially accumulated in the plasma region. Although the exact mechanism of the NPs trapping is not yet well understood, it is well known that such a big NPs could easily gain a negative charge in a plasma close to the magnetron [120]. As it was shown in the previous study of plasma potential close to the target of the magnetron operated in GAS, the region with positive potential with the respect to the plasma is formed

above the center of the magnetron target. Such positive potential can attract the negatively charged NPs [121]. Hence, an electrostatic force acting on the charged NPs was suggested to be a major factor responsible for the formation of the trapping region where the cloud of the NPs is present. Trapped NPs can subsequently grow in size and if this happens in the high mobility region of the energetic conditions, big NPs with cubical shape are formed. The growth of trapped NPs continues until they reach some critical size that allows them to escape from the trap (either by the gravity force or by neutral drag force). In some cases, the growing cubic nanoparticles can also collide with small spherical NPs, which leads to the formation of a big cubic nanoparticle decorated by small spheres as described earlier (Figure 39). Although the trapping can satisfactorily explain the origin of large cubic NPs, it still does not explain why the big NPs can more easily escape the aggregation source in case of a weaker magnetic field.

Herein, we assume that the intensity of the magnetic field has to significantly influence the motion of NPs. Since the magnetic field lines at the center of the magnetron are nearly perpendicular to the surface, the movement of charged species in such a field has a component governed also by the magnetic part of the Lorentz force, which leads to the rotation of the cloud of trapped NPs above the magnetron.

The magnitude of the Lorentz acceleration  $a_{Lorentz}$  on the particle is given by

$$a_{Lorentz} = \frac{q_{NP} v_{tr} B_v}{m_{NP}} \quad (21)$$

where  $q_{NP}$  is the charge of nanoparticle,  $v_{tr}$  is the tangential velocity of the particle cloud,  $B_v$  is the vertical magnetic field and  $m_{NP}$  is the mass of the nanoparticle. It was already mentioned that nanoparticles are easily charged in an active plasma. For simplicity, we will use the phenomenological model of charging of particles by Bonitz et al. [122].

$$q_{NP} = K_q e r_{NP} T_{e[eV]} \quad (22)$$

where  $K_q$  is the coefficient of charging on NPs ( $1.4 \times 10^9 \text{ nm}^{-1} \text{ eV}^{-1}$ ),  $e$  is the elementary charge,  $r_{NP}$  is the radius of NPs and  $T_{e[eV]}$  is the electron temperature in eV (estimated to be 8 eV from the trend observed with  $T_e$  values under similar conditions in [121]).

If we express the mass of NPs by their radii and density, we obtain:

$$a_{Lorentz} = \frac{3}{4\pi} K_q e T_{e[eV]} \frac{v_{tr} B_v}{r_{NP}^2 \rho_{NP}} \quad (23)$$

Let's simplify the situation by the assumption that the force holding radially the particles is only the Lorentz force. By equating the Lorentz acceleration with centripetal acceleration on the particle moving on the outer edge of the trapped rotating cloud of NPs, we obtain the circumferential velocity attainable by the nanoparticle cloud

$$v_{tr} = \frac{3}{4\pi} K_q e T_{e[eV]} \frac{R_{tr} B_v}{r_{NP}^2 \rho_{NP}} \quad (24)$$

where  $R_{tr}$  is the outer diameter of the trapped cloud.

For the particles of the diameter  $r_{NP} = 100 \text{ nm}$  we obtain  $v_{tr} = 0.03 \text{ m. s}^{-1}$ . Such velocity is comparable with the velocity of the neutral gas in the aggregation chamber and corresponds with the period of the rotational motion of NPs of about 3 seconds for a 3 cm diameter of the NPs cloud. Actually, some oscillations of a similar period ( $\sim 2 \text{ s}$ ) can be seen in the beginning of the time-resolved record of the X-ray scattering on NPs in GAS in the paper by Kousal et al. [119].

The real situation is obviously more complicated since there is the influence of the local electric fields in the plasma in the presence of NPs [121]. The interactions with the neutral gas and ions will affect the observed behavior of the system in dependence on pressure. However, the simple calculations above show that already the magnetic field itself is an important player in the dynamics of the trapped cloud and its alteration may thus influence the trapping/release of nanoparticles.

At a sufficiently high magnetic field, trapped NPs are partially re-deposited within the central area of the target. On reducing the MF the trapping efficiency is weakened in the radial direction and NPs could escape the trap region with the flow of buffer gas. It should be noted that the transport capability of the carrier gas to deliver NPs onto the substrate located in the main deposition chamber increases with increasing cross-section of the nanoparticle. Nevertheless, a sufficiently high flow rate of Ar (drag force) and hence the pressure in GAS must also be provided. As it could

be seen in Figure 6a, at the pressure of 40 Pa the drag force of buffer gas is low and we did not observe big NPs in the deposit. This, however, doesn't mean that such NPs are not produced – they can be deposited onto the bottom wall of the deposition chamber due to the gravity force. With the pressure increase, the drag force acting on the NP surface increases and bigger NPs could escape the trapping region and the aggregation chamber. This effect is enhanced when the intensity of MF and, hence, efficiency of electromagnetic trapping is lowered. As a result, bigger NPs approximately  $150\pm 20$  nm in diameter could be detected (Figure 39b). In that case, an abrupt increase in DR at the low intensity of MF could be explained by increasing the number of massive cubic and agglomerated NPs that are more easily leaving the aggregation source. The above considerations show that not only the formation of the NPs inside the GAS but also the transport of those NPs from the trapping region is an important issue for the deposition rate of the NPs.

Production of the Cu NPs was characterized by the stable in time deposition process (Figure 40). We investigated the deposition rate of NPs and discharge voltage for three different positions of the magnetic field. It was found that above-mentioned parameters remain almost unchanged for 60 min. The slight decrease in discharge voltage is observed due to more diligent target cleaning during the magnetron operation period.

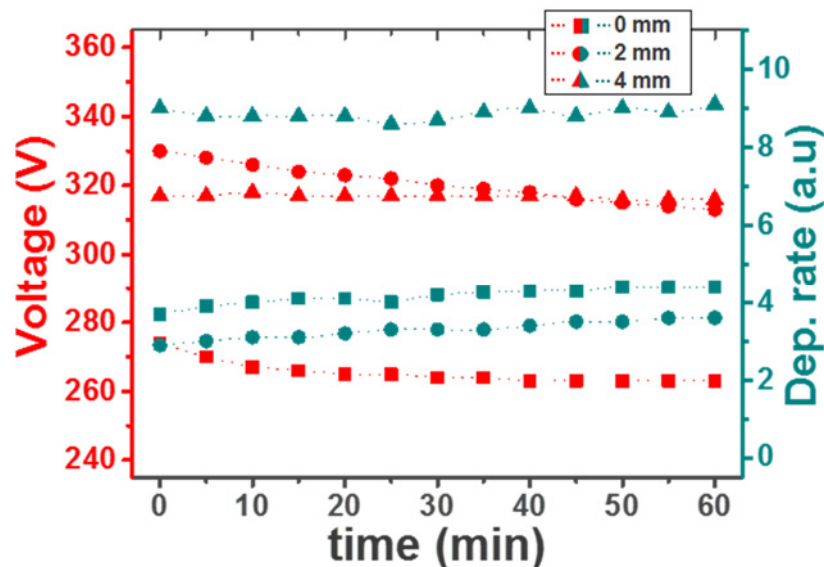


**Figure 40.** The time evolution of the discharge voltage and deposition rate of Cu NPs for 0, 2 and 4 mm positions of the magnetic circuit (at constant pressure 60 Pa and current 200 mA).

### 4.1.3. Shape of the nanoparticles

As it is well known from the thermodynamic considerations, the most favorable shape of NP is spherical due to the surface energy minimization [123]. Nevertheless, a number of various forms of NPs fabricated by means of GAS were reported in the literature [124]. It follows, there are preferential conditions in aggregation source which contribute to the formation of nanospherical NPs. The probability to obtain nanoparticle with the shape different from spherical is higher for larger NP because in this case, the potential energy difference for all shapes becomes increasingly negligible [117].

In position 0 mm we have the highest number density of sputtered copper atoms under all range of deposition conditions (Figure 38). High Cu atoms concentration contributes also to the heating in the aggregation region through the thermalization process and therefore provides high mobility of Cu atoms on the growing surface of NP [125]. As a result, spherical or near-spherical shape of NPs was obtained at such a high-deposition or high-temperature environment. The same is true for all other positions of the MC and pressures below 50 Pa where the number density of copper atoms in plasma remains sufficiently high. Also, as it was already mentioned, the overall energy flux on the growing NP is much more prominent under low pressures contributing to the temperature increase.

Continuing to increase pressure under low intensities of the MF, we gradually transfer into the regime where the optimum ratio between the ad-atoms mobility and deposition was reached. It is because of more efficient cooling of growing NPs by Ar and hence decrease of Cu atoms surface mobility and decrease of Cu deposition rate onto the NPs due to decrease of amount of sputtered Cu atoms. This is caused by decrease of energy of Ar ions with increasing pressure. Such a combination results in the formation of nanocubes and more complex agglomerated NPs as could be seen in Figure 39b. These statements are in good agreement with a recently published study by Zhao et.al when studying the formation mechanism of Fe nanocubes as already mentioned earlier [117].

Moreover, an interesting result was obtained at the magnetic field of 45 mT (4 mm position). By adjusting only Ar pressure in the aggregation chamber, it is possible to tailor the shape of the produced NPs. Hence, spherical, spherical/cubic and cubic

NPs were obtained at 40, 60 and 80 Pa respectively (Figure 41). Here, the simultaneous presence of spherical and cubic NPs at 60 Pa corresponds to the transition mode between the above mentioned deposition regimes. High-resolution TEM images revealed polycrystalline structure, for both spherical and cubic NPs (Figure 42).

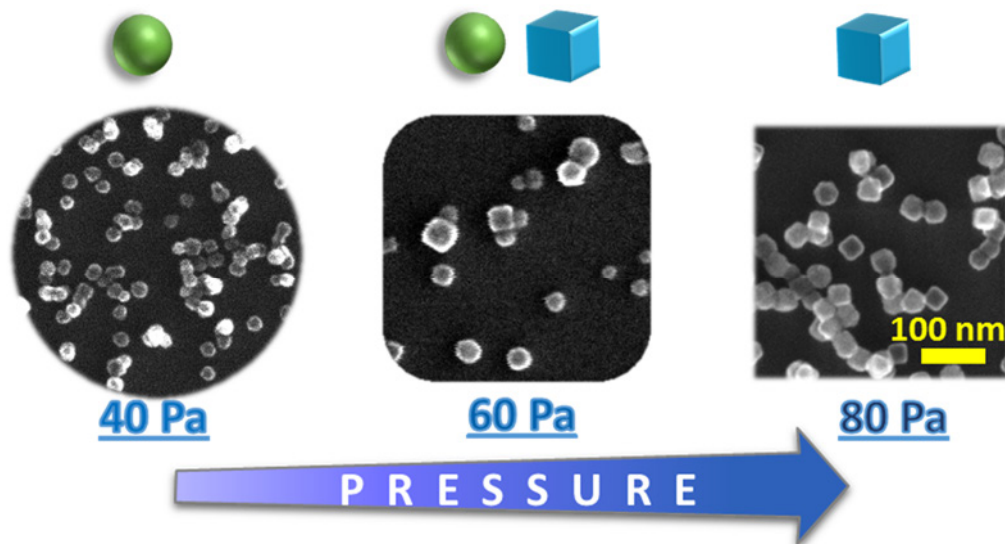


**Figure 41.** Schematic representation of the transition mode of Cu NPs from a spherical shape to cubic in dependence on the pressure in GAS (current - 200 mA; MF - 45 mT).

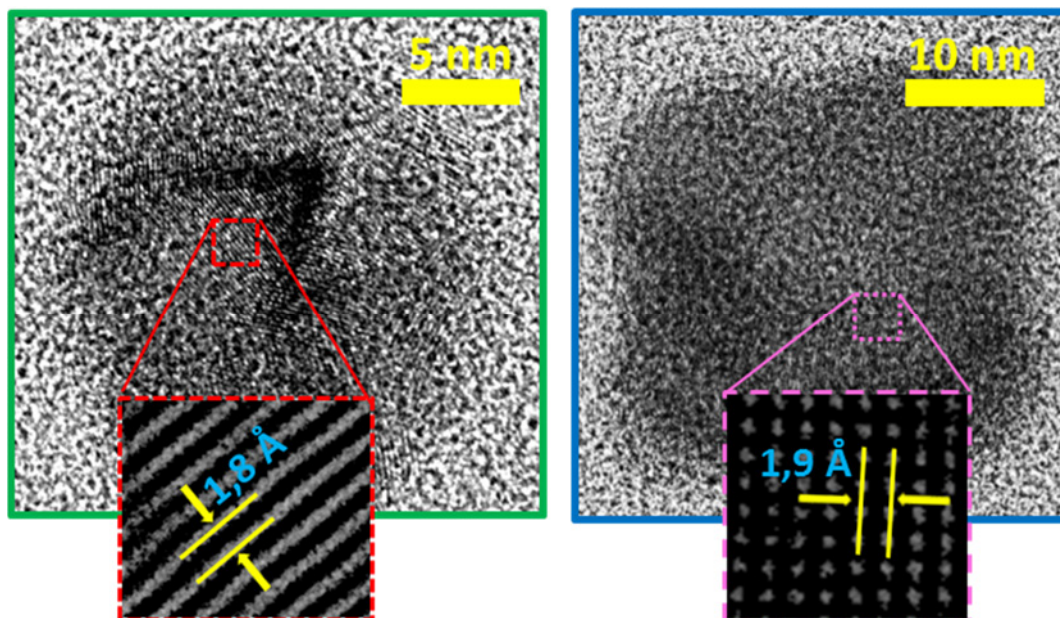


**Figure 42.** HRTEM images of the spherical and cubic NPs and inverse FFT patterns of the selected areas (inset).

## 4.2. Deposition of Ag/a-C:H nanocomposite coatings with surface enrichment

This chapter of the thesis is based on the scientific results that were already published in the paper entitled “*Deposition of Ag/a-C:H nanocomposite films with Ag surface enrichment*”, cited as M. Vaidulych, J. Hanuš, T. Steinhartová, O. Kylián, A. Choukourov, J. Beranová, I. Khalakhan, H. Biederman, *Plasma Process. Polym.*, **2017**, 14, 1600256, <https://doi.org/10.1002/ppap.201600256>.

Ag/a-C:H nanocomposite coatings were fabricated by simultaneous deposition of Ag nanoparticles and hard a-C:H matrix (see experimental part 3.1.4). This approach allows decoupling formation of NPs from the matrix deposition and thus provides almost independent control of the matrix properties and amount and size of embedded Ag NPs. Subsequently, selected samples were exposed to three types of plasma in order to be functionalized. The influence of the plasma processing on the surface morphology, chemical composition and antibacterial properties of the coatings was studied.

### 4.2.1. Ag/a-C:H nanocomposites

*Deposition of the a-C:H.* The thin films deposition of hard a-C:H plasma polymers (sometimes called “hard amorphous hydrogenated carbon”) was conducted in the mixture of Ar/n-hexane in the experimental arrangement described in 3.1.1. The ratio of partial pressures was chosen 7:1 and the total pressure in the deposition chamber was set to 5.5 Pa. Samples were placed directly onto the RF electrode. The RF power was varied in the range of 30 to 90W with corresponding negative self-bias 210 - 410 V respectively. The deposition rate was found to be 24 nm/min at the lowest power and reached its maximum of 52 nm/min at 90 W. Changes in the power resulted also in the variation in the optical characteristics of the prepared films. The transmittance of 200 nm thick films at a wavelength of 550 nm decreases from 62% down to 40% with the RF power increase from 30 to 90 W (Figure 43).

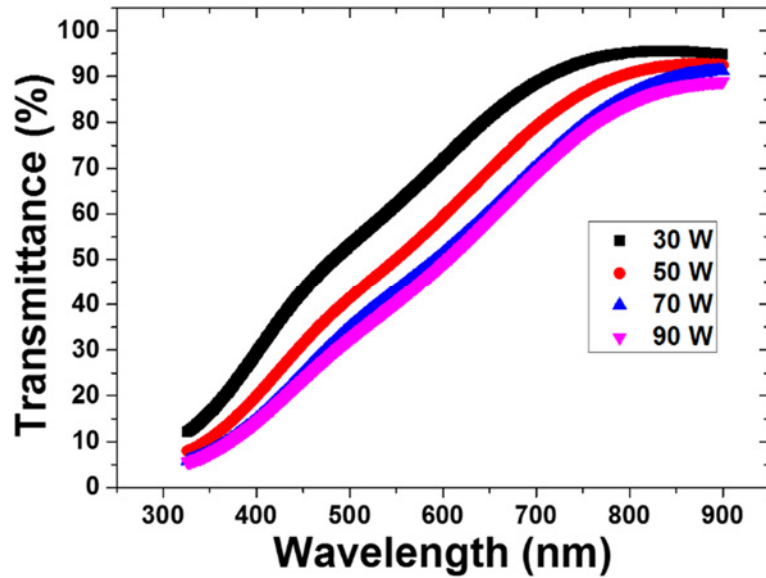


**Figure 43.** UV-Vis spectra of 200 nm a-C:H films prepared at different RF powers.

The films prepared at the power of 90 W revealed poor adhesion to the glass or Silicon substrates due to the high compressive stress of hard coatings, as it was already reported elsewhere [116]. Therefore, the power of 30 and 70W was chosen for the matrix deposition during the fabrication of functional nanocomposite coatings. According to the nanoindentation measurements, the hardness of a-C:H films for given powers was  $8 \pm 0,6$  and  $16 \pm 1$  GPa, and the complex modulus was  $50 \pm 2$  and  $120 \pm 9$  GPa respectively. The chemical composition measured by XPS did not depend on the RF power and was  $\sim 95$  at.% of C and  $\sim 5$  at.% of O. The AFM measurements revealed very smooth and pin-hole free surface of the a-C:H films with the RMS roughness below 1 nm (Figure 44).

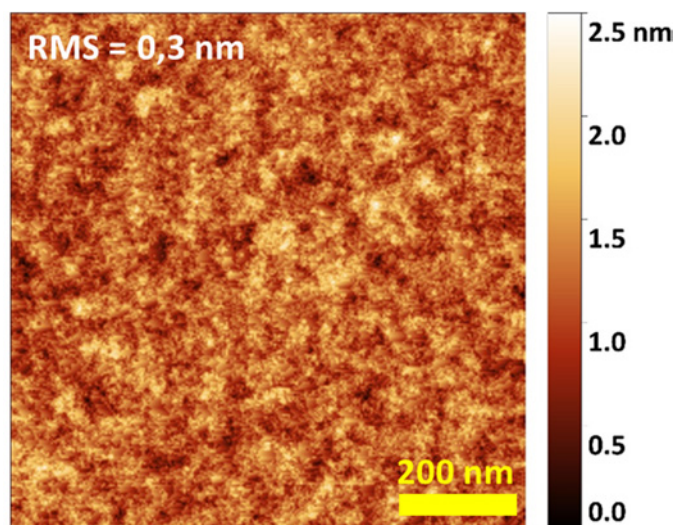


**Figure 44.** AFM image of a-C:H thin film deposited at RF power 30 W.

*Ag nanoparticles deposition.* Nanocomposite fabrication requires a well-established and temporally stable deposition process of nanoparticles. For this reason, deposition conditions inside the GAS were optimized as follow: the pressure – 100 Pa (Ar flow 15.7 sccm), the aggregation length – 8 cm and the DC magnetron current was varied from 100 to 300 mA. In Figure 45, SEM images of Ag NPs are present as a function of current. It could be seen that the size distribution of Ag NPs remains near the same when increasing current from 100 to 300 mA. The mean diameter of NPs was around 25 nm whereas the number of produced NPs increases from  $57 \text{ NPs} \cdot \text{min}^{-1} \cdot \mu\text{m}^{-2}$  to  $336 \text{ NPs} \cdot \text{min}^{-1} \cdot \mu\text{m}^{-2}$  respectively. It gives a useful tool for the fabrication of nanocomposite coatings with a similar size distribution of NPs and different filling factor.

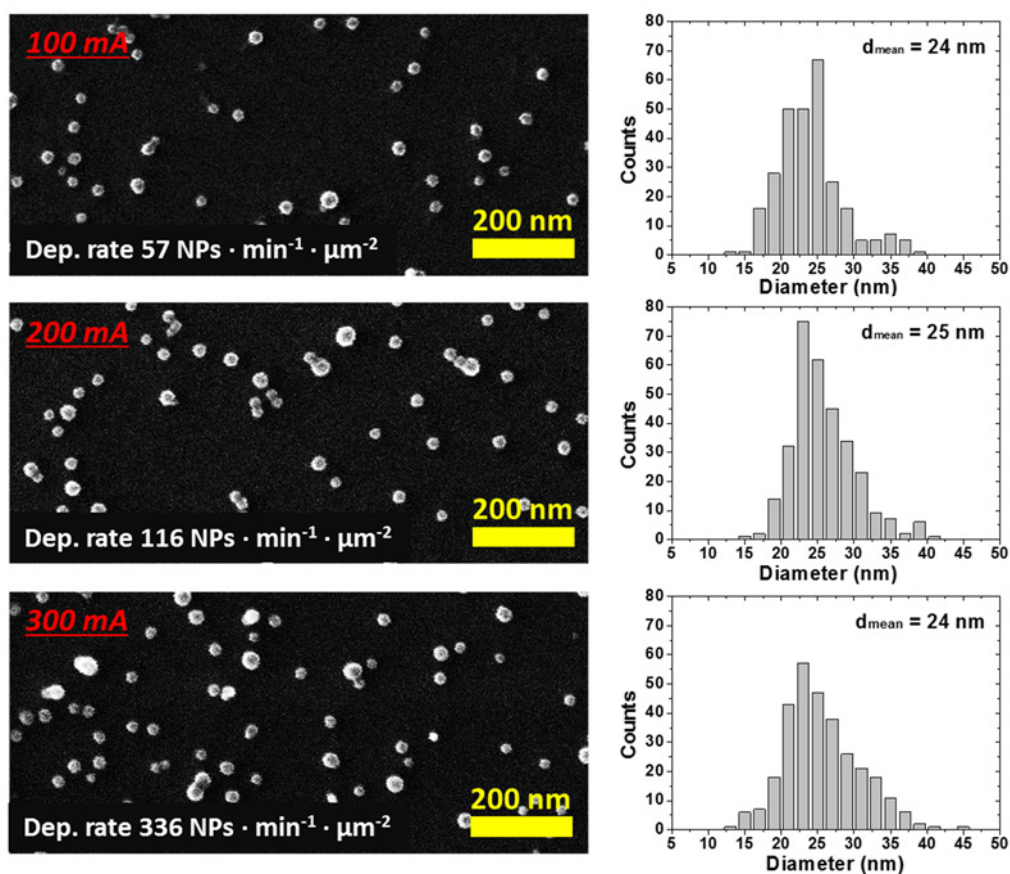


**Figure 45.** SEM images of silver NPs prepared at different currents with corresponding size distribution.

*Ag/a-C:H nanocomposites*. During simultaneous deposition of Ag NPs and a-C:H matrix was found that the NPs cannot reach the substrate when RF discharge is operated in continuous regime. Therefore RF discharge was operated in the pulsed regime with the frequency of 1 Hz and duty cycle of 50%.

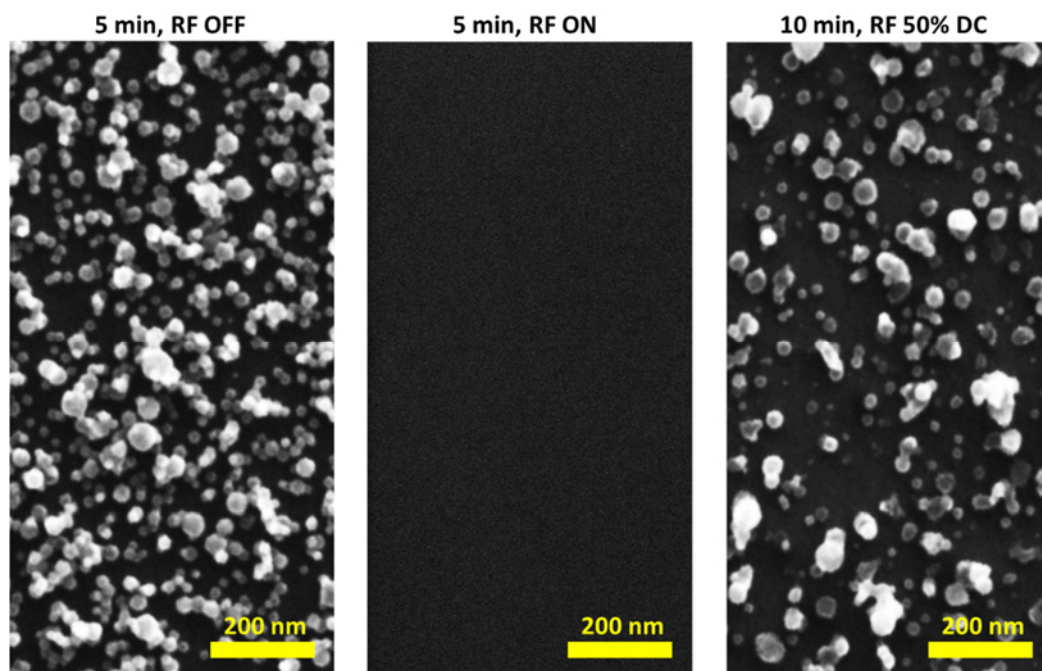


**Figure 46.** SEM images of Ag NPs in dependence on RF regime in the deposition chamber (magnetron current 200 mA, RF power 70W)

In Figure 46 are shown SEM images of Ag NPs deposited without RF discharge, with RF discharge operated in continuous mode and NPs deposited at the same RF power (peak value) but in the pulsed mode as mentioned above. Such an effect was already reported and could be explained as follow [116]. When Ag NP enter the RF discharge, one gain negative charge in the environment of very mobile plasma electrons. Then repulsion mechanism is realized through the electrostatic forces acting between the negatively charged NP and negatively self-biased RF electrode. In the pulsing regime, the NP reach the substrate only during  $T_{off}$ . On the contrary the polymer matrix is deposited only during  $T_{on}$ . One should keep in mind, that in this case the overall number of deposited NPs decrease as compared with the deposition without the RF discharge.

Also, it should be mentioned that Ar plasma itself has an influence on the size of Ag NPs. Long exposure of NPs to the highly energetic bombardment leads to the

physical etching of the material of the particle and thus decrease in the size. UV-Vis spectra in Figure 47 also confirm this fact. Since Ag NPs exhibit a surface plasmon resonance in the UV and visible range of spectra, the size distribution and relative amount of NPs can be verified by the position and width of the characteristic absorbance peak. In the case of Ag NPs deposited for 10 minutes with RF ON (duty cycle 50%, power 70 W) broadening in the absorbance peak corresponds to the increase in the size distribution of the NPs.

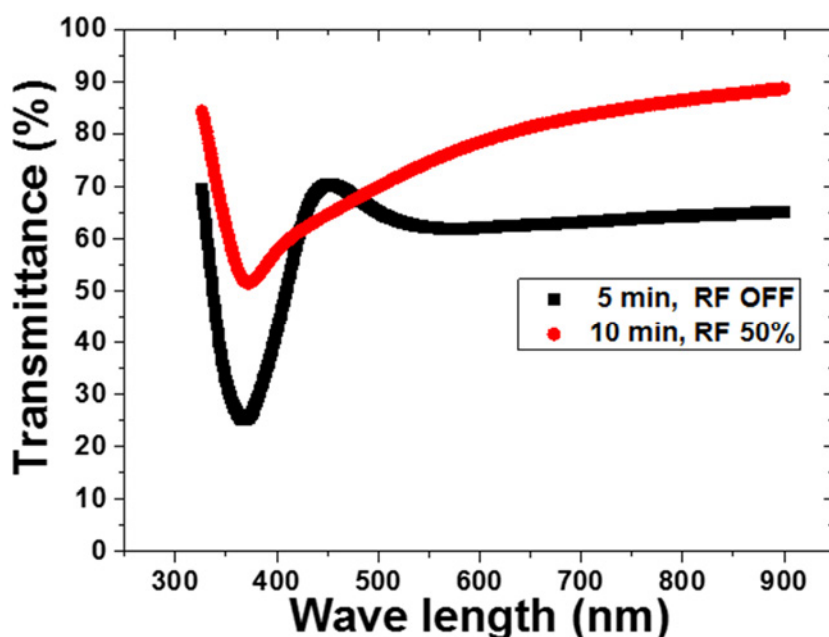


**Figure 47.** UV-Vis spectra of Ag NPs deposited for 5 min with RF OFF and 10 min with RF 50 % duty cycle at 70 W.

Based on the above described results, deposition conditions were kept constant in all experiments (Ar:n-hexane = 7:1, total pressure 5.5 Pa, pulse frequency 1 Hz, and duty cycle 50%) and two types of nanocomposites were prepared. Those deposited at RF power 30W (negative self-bias 210 V) and those prepared at 70W (negative self-bias 370 V). For simplicity, further in the text are such nanocomposites referred as soft and hard. The number of embedded NPs into the polymer matrix was controlled independently by changing the DC magnetron current in the GAS. The deposition rate of Ag NPs was verified by the QCM before each nanocomposite deposition. In Figure 48, a series of soft nanocomposites are presented as a function of the magnetron current. As it could be seen in Figure 49, all nanocomposites were endowed with a

characteristic absorbance peak with a position around 460 nm. The peak of plasmon resonance enhances with the increase in the number of Ag NPs. Such a feature allows utilize UV-Vis spectroscopy for fast and reliable control of the NPs content in nanocomposite coatings straight away after the deposition process.

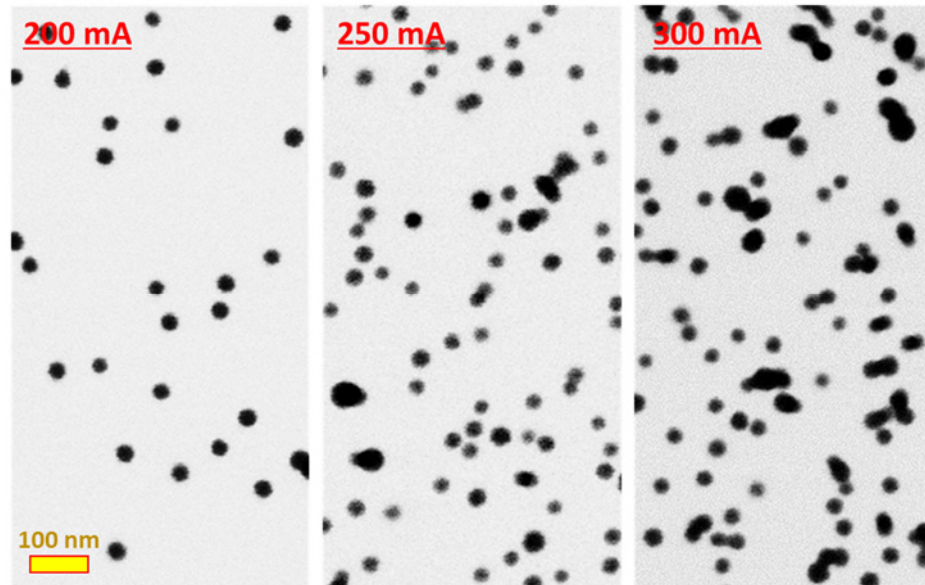


**Figure 48.** SEM images from BSE detector of Ag/a-C:H coatings prepared at the RF power of 30W and different magnetron currents: 200, 250 and 300 mA.

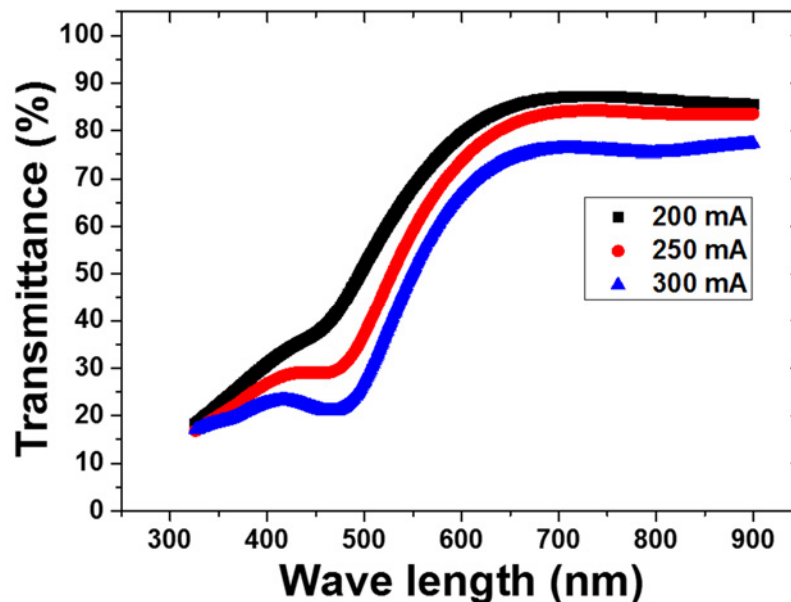


**Figure 49.** UV-Vis spectra of Ag/a-C:H nanocomposites prepared at the RF power of 30 W and the magnetron current of 200, 250 and 300 mA.

Abovementioned nanocomposite coatings revealed XPS surface concentration of Ag below 0.2 at%. However, as it was shown by Hanuš et.al when studied Cu/a-C:H nanocomposites, the bulk and surface concentration may differ significantly [116]. In their study, Rutherford backscattering measurements revealed near 10 times higher Cu concentration in the bulk, as compared to the Cu surface concentration measured by XPS. It was also found that an increase in the content of NPs leads to the worsening in the mechanical properties of nanocomposites. It could be explained by the increase in structural defects and poor bond formation between the metallic NPs and the polymeric matrix. Thus, low filling factor of NPs is preferable to keep excellent mechanical properties of the metal/polymer nanocomposites.

The indentation measurements of hard Ag/a-C:H nanocomposites with the Ag surface concentration around 1 at% revealed near identical mechanical properties in comparison with pure a-C:H films. The hardness and complex modulus were  $14 \pm 3$  GPa and  $110 \pm 19$  GPa for nanocomposite and  $16 \pm 1$  GPa and  $120 \pm 9$  GPa for bare a-C:H film. In Figure 50, SEM images of such nanocomposites revealed uniform distributed of Ag NPs in the volume of the polymeric matrix.

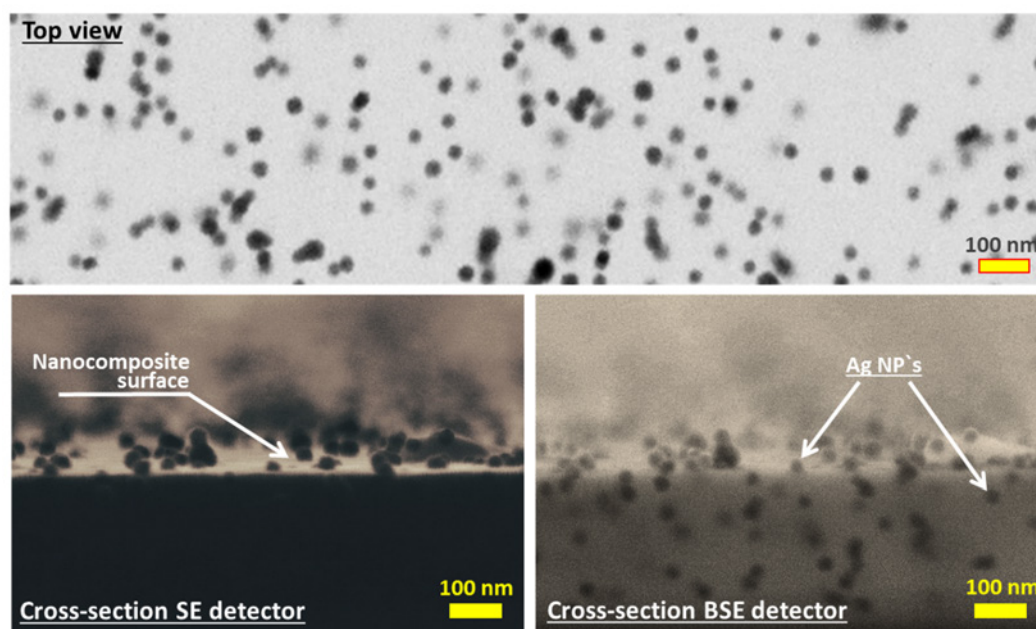


**Figure 50.** SEM images of Ag/a-C:H nanocomposites and corresponding cross-section images from SE and BSE detectors.

The AFM image for soft (30 W) and hard (70 W) nanocomposites are shown in Figure 51. The RMS roughness was around 6.5 nm in both cases (scan size  $2.5 \times 2.5 \mu\text{m}^2$ , resolution 256). However, the surface of hard Ag/a-C:H nanocomposite was covered with small well-defined holes. According to the surface profile, the diameter of the holes was close to the size of NP and the depth extends up to 10 nm. The origin of such holes could be attributed to the loss of some NPs during the nanocomposite fabrication. It is well known that hard a-C:H films could accumulate high compressive stress during the growth period. When NP landed onto the substrate, one would experience compressive stress of the growing film. This leads to the compressive force acting to the bottom part of the nanoparticle. Thus NP tends to be ejected from the matrix before it is sufficiently fixed by the growing polymer film (Figure 51). The decrease in the number of holes for the nanocomposites prepared at lower power and thus lower compressive stress confirms this statement. Taking into account the aforementioned, Ag/a-C:H nanocomposites prepared at RF power 30 W were chosen for experiments with plasma etching(see below).

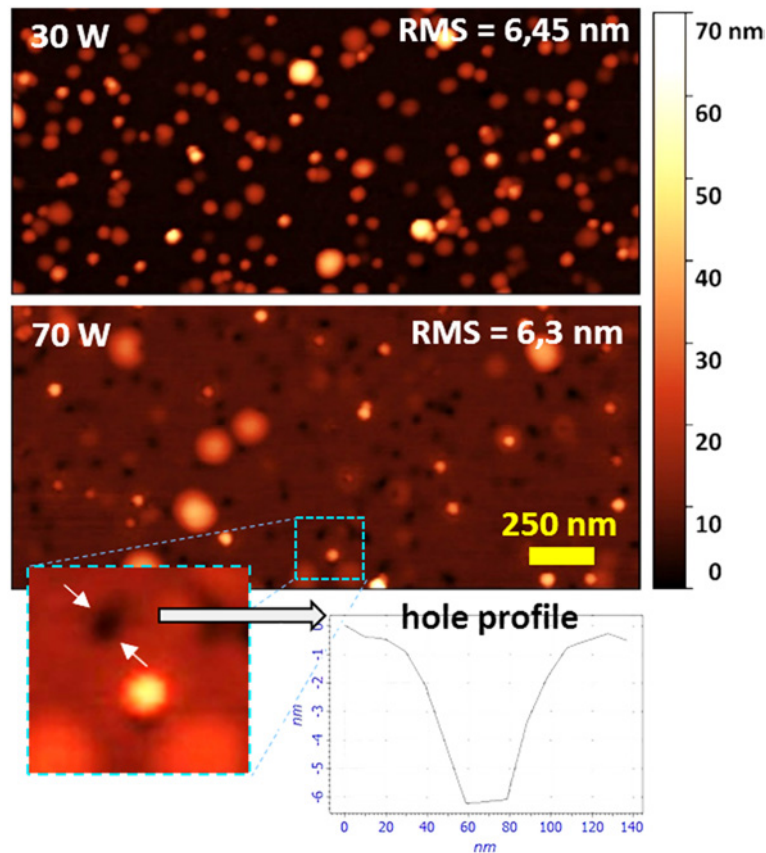


**Figure 51.** AFM images of Ag/a-C:H nanocomposites deposited at the RF power of 30 W (top) and 70 W (bottom).

#### 4.2.2. Plasma etching for Ag surface enrichment of nanocomposites

As it was discussed above, silver content in the Ag/a-C:H nanocomposites was kept low enough to preserve good mechanical properties. However, to obtain sufficient antibacterial properties of the nanocomposites, higher Ag surface concentration is necessary. The possible route is to remove the outermost layer of the matrix material, and thus exposed more Ag NPs. Such Ag surface enrichment could be realized using a plasma processing, namely plasma etching. Herein, three types of plasma were utilized: N<sub>2</sub> plasma etching with the samples placed directly on the RF electrode; O<sub>2</sub> plasma etching (the same configuration); and O<sub>2</sub> plasma etching with samples placed on the grounded substrate holder. For this needs, nanocomposite samples with Ag surface concentration of 0.2 at% (DC magnetron current 100 mA, RF power 30 W) were prepared and then used for etching. It should be mentioned, that plasma etching in first two cases was operated in the reactive ion etching (RIE) regime. This means that the chemical etching of reactive species was enhanced by the bombardment of positive ions accelerated in the electric field of negative self-biased electrode (see, Chapter 2.2).

*Nitrogen plasma etching.* Nitrogen was chosen because plasma activated nitrogen species may induce the release of low-molar-mass volatile compounds upon their chemical interactions with the organic matrix [10]. However, the kinetics of chemical reactions with silver is much slower at room temperature [126].

Samples were placed onto the RF electrode where the nitrogen etching takes place. The treatment conditions were kept constant in all experiments as follows: N<sub>2</sub> pressure 2.5 Pa, RF power 16W, negative self-bias 150 V. Under the given conditions, the etching rate of the bare a-C:H matrix was found to be 5 nm/min and the etching time was varied from 30 s up to 8 min. The chemical composition of nanocomposites before and after etching was determined by means of XPS (Figure 52). After the first 30 s of etching, significant changes in the elemental composition occur, basically due to the increase of the nitrogen content from 0.1 to 12.7 at%. With further increase in the etching time, no significant changes in the chemical composition were observed. After 8 min of the nitrogen etching, Ag surface concentration reached steady state value of 2.3 at% as compared with 0.2 at% for the untreated sample. This confirms the

preferential loss of the polymeric matrix. However, the selectivity of the etching process under the given conditions is not optimal (see more details below). The Ag surface concentration is still low for a sufficient antibacterial activity.

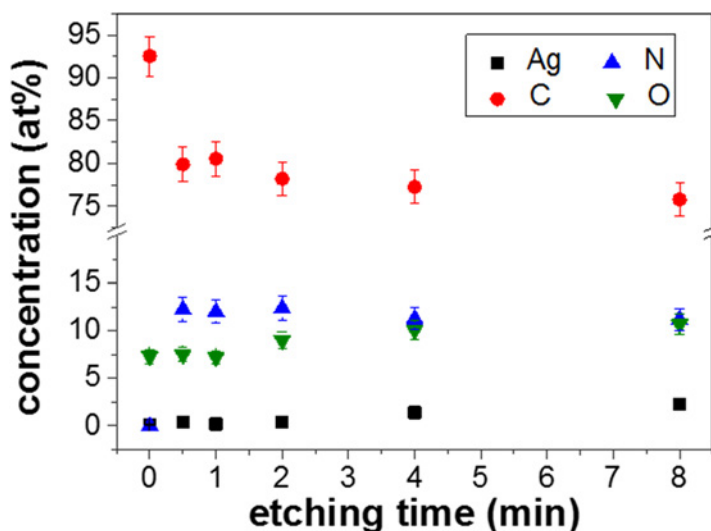


**Figure 52.** Elemental composition obtained from XPS of the Ag/a-C:H nanocomposites etched in the RF nitrogen plasma.

*Oxygen plasma etching.* Oxygen was used because it is a well-known etching gas for polymeric coatings. Moreover, the additional oxidation of the Ag NPs is expected upon the interaction with plasma activated oxygen species. This could potentially improve the antibacterial properties of the nanocomposites.

Working conditions for oxygen etching were chosen similar to those during the nitrogen etching. However the negative self-bias, in this case, was 160 V and the etching rate of the matrix increased to 8 nm/min. XPS showed a rapid increase in the oxygen surface concentration from ~7 at% to ~17 at% in the first 30 s of etching which remained the same for longer etching time. Ag surface concentration gradually increased with etching time and reached its saturation level of around 6 at% after 4 min treatment (Figure 53). Further increase in the etching time has a negligible effect on the chemical composition and Ag surface concentration remains almost the same after 8 min treatment. These results correlate well with the data obtained for nitrogen treatment. In the case of oxygen plasma, the etching rate of the matrix was almost twice as compared to nitrogen. Thus, Ag content on the surface may be doubled under the same etching conditions.

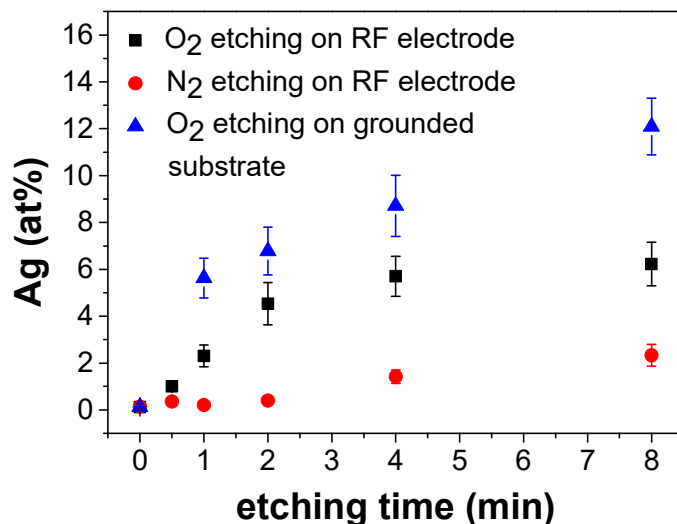


**Figure 53.** Comparison of surface Ag concentration measured by XPS as a function of etching time in case of etching in oxygen and nitrogen plasma. Samples were placed on the RF electrode or on the grounded substrate holder.

In Figure 54, cross-section SEM images of the nanocomposites before and after 4 min oxygen etching are presented. It could be seen, that plasma exposure leads to the decrease in the thickness of the nanocomposite, whereas the presence of Ag NPs on the nanocomposite surface become more prominent. However, such an increase in the number of NPs was accompanied by a decrease in their size. The effect is dedicated to the partial sputtering of nanoparticles in the oxygen discharge. With RF negative self-bias of 160V, oxygen ions can gain enough energy to sputter of Ag atoms. AFM measurements of bare Ag NPs also confirm this fact (Figure 55). For this needs, NPs were deposited on Si substrate and oxygen etching was applied under similar conditions as for nanocomposite coating. The size distribution of nanoparticles revealed a decrease in the size of Ag NPs from 25 nm for untreated sample down to 7 nm after the 4 min oxygen etching.

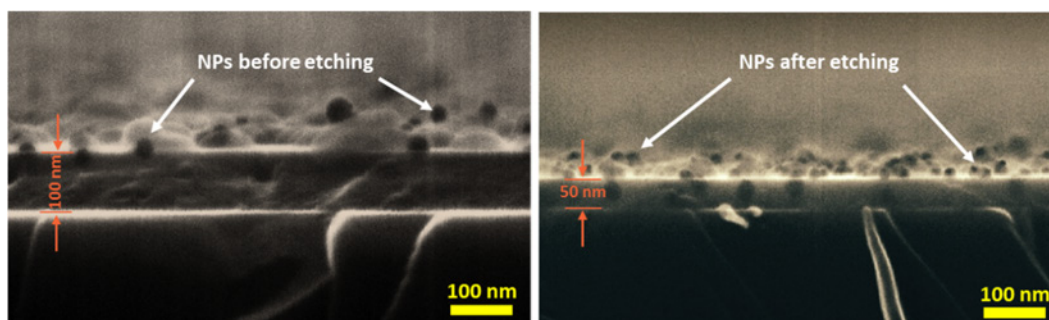


**Figure 54.** SEM images of a cross-section of Ag/a-C:H nanocomposite as deposited (left) and after 4 min etching in the O<sub>2</sub> plasma (right).

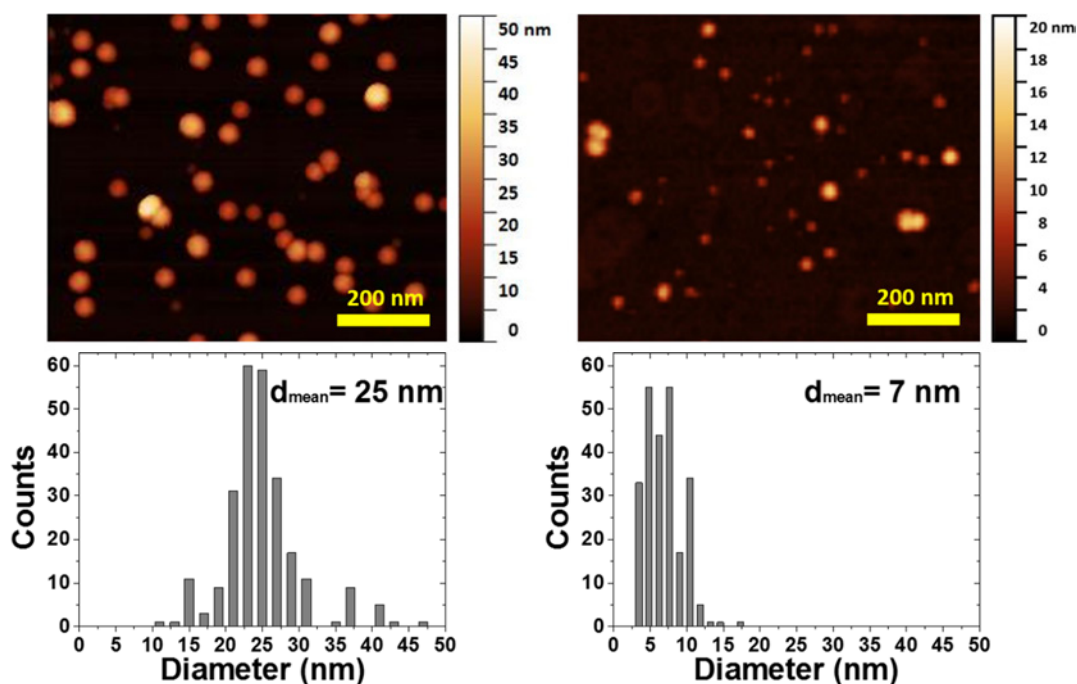


**Figure 55.** AFM images of Ag NPs before (left), after 4 min treatment in  $O_2$  atmosphere (right) and corresponding histograms of NPs size distribution.

*O<sub>2</sub> etching out of the electrode.* The third type of plasma etching was treatment in the oxygen atmosphere when the nanocomposites are placed on the grounded substrate holder 5 cm apart from the RF electrode. The plasma conditions were similar to previous experiments. In this configuration, the energy of incident species on the grounded substrate was much lower compared to previous cases. Thus the etching rate of the a-C:H matrix was 1.9 nm/min.

According to Figure 53, Ag surface concentration reached 12 at% after 8 min of etching. SEM analysis of the etched coatings did not show any significant changes in the size distribution of the Ag NPs during the nanocomposite etching. These confirm high selectivity of the etching process and a nearly two-fold increase in the Ag surface concentration as compared to the oxygen etching on the RF electrode. This is because the energy of bombarding species is low to cause significant Ag sputtering.

### 4.2.3. Antibacterial activity of Ag/a-C:H nanocomposites

A colony forming unit method was utilized to investigate the antibacterial properties of the produced nanocomposites against the gram-negative bacteria *Escherichia coli*. For this need, a series of soft Ag/a-C:H nanocomposites prepared at the magnetron current of 100, 200 and 300 mA were used. As a negative control, a set of a-C:H films was prepared as well.

According to Figure 56, after 3 h incubation period bare a-C:H films do not show any activity against *E.coli* and the number of CFU remains high. In turn, nanocomposites prepared under the DC current of 100, 200 and 300 mA and thus different content of Ag NPs revealed an antibacterial activity. The highest reduction in CFU was obtained for the samples prepared at 300 mA, when the Ag NPs content in the nanocomposite was the highest.

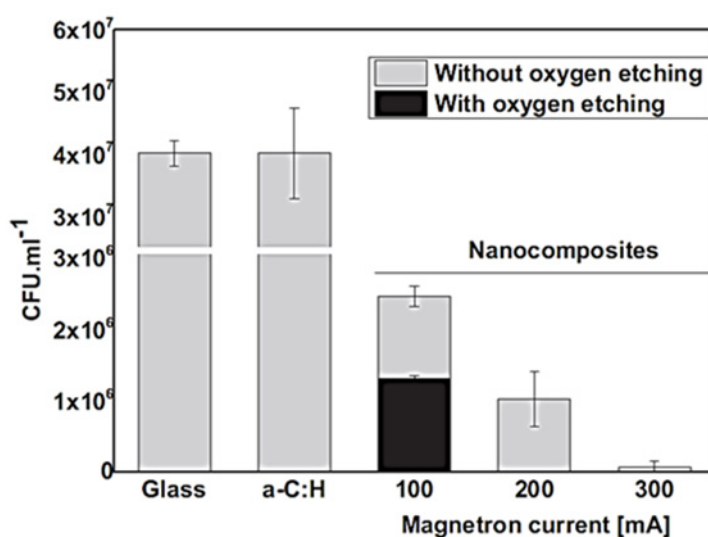


**Figure 56.** Reduction in number of *E. coli* bacteria after 3 h of incubation with samples prepared with different magnetron currents and with additional oxygen plasma etching (adopted from [49]).

In addition, a set of Ag/a-C:H nanocomposites deposited at the magnetron current of 100 mA was prepared to investigate the effect of the plasma etching on the antibacterial activity. The nanocomposites were placed on the grounded substrate holder and exposed to O<sub>2</sub> plasma discharge for 4 min (pressure 2.5 Pa, power 16 W). It was found that such oxygen etching leads to a further increase in the antibacterial

activity of the nanocomposites. As it is shown in Figure 56, samples after 4 min oxygen etching exhibit near two-fold decrease in CFU as compared to the samples without any oxygen etching. Such a plasma processing is an effective solution to adjust the surface properties of nanocomposites to enhance antibacterial activity.

### **4.3. Functional nanocomposite coatings for facile oil/water separation and biomedical applications.**

Most of the experimental work and results presented in this chapter of the thesis are based on the article entitled “*Super-wettable antibacterial textiles for versatile oil/water separation*”, published in the journal *Plasma Processes and Polymers*: M. Vaidulych, A. Shelemin, J. Hanuš, I. Khalakhan, I. Krakovsky, P. Kočová, H. Mašková, J. Kratochvíl, P. Pleskunov, J. Štěřba, O. Kylián, A. Choukourov, H. Biederman, *Plasma Process Polym.*, **2019**, e1900003, DOI: 10.1002/ppap.201900003.

Herein, a step-by-step modification process based on the combination of PECVD and NPs deposition by GAS is utilized to prepare functional nanocomposite coatings on filtration membranes. Such an environmentally friendly approach allows functionalizing a wide range of porous substrates to satisfy the vast majority of needs for oily water purification. Superhydrophobic membranes prepared by treatment of non-woven viscose fabric demonstrate a high ability for selective absorption of non-polar organic solvents from water volume. Superamphiphilic membranes based on the carbon paper are suitable for smart separation of the mixture of water with either light or heavy oil with efficiency above 99.97%. Both types of membranes exhibit antibacterial properties against *Escherichia coli* that was realized through the monolayer of Cu NPs embedded into the polymeric matrix of the functional nanocomposite coatings.

#### 4.3.1. Thin film deposition and nanoparticles fabrication

*Organosilicon thin films.* PECVD deposition process in the working gas mixture containing hexamethyldisiloxane (HMDSO) was used to obtain two types of thin film coatings: hydrophobic (C:H)SiO<sub>x</sub> and amphiphilic SiO<sub>x</sub>. Hydrophobic films were obtained in the mixture of Ar and HMDSO with the ratio of partial pressures 7:1 and the total pressure in the deposition chamber of 2.5 Pa. With the predominant breakage of Si—O and Si—CH<sub>3</sub> bonds in the RF discharge, the resulting elemental composition of the (C:H)SiO<sub>x</sub> coating was 53 at.% of carbon, 18 at.% of oxygen and 29 at.% of silicon (see XPS spectra in Figure 57). High atomic concentration of the carbon corresponds to the abundant presence of the non-polar methyl groups in the coatings [34,127]. This determines the hydrophobicity of the (C:H)SiO<sub>x</sub> films with the static WCA of 105°.

In the case of amphiphilic coatings, XPS measurements revealed near silica-like structure with atomic concentration, as follows: 5 at.% of carbon, 62 at.% of oxygen and 33 at.% of silicon. Here, the mixture of O<sub>2</sub> and HMDSO with the ratio of partial pressures 30:1 (P<sub>total</sub> 1 Pa) was used. Presence of the oxygen in the working gas mixture leads to the significant reduction of the carbon in the resulted coatings through the formation of CO<sub>x</sub> gaseous species. They have a low affinity to the surface and they are simply pumped out from the deposition system [128]. Consequently, SiO<sub>x</sub> films with high surface energy and the static WCA of 25° were obtained.

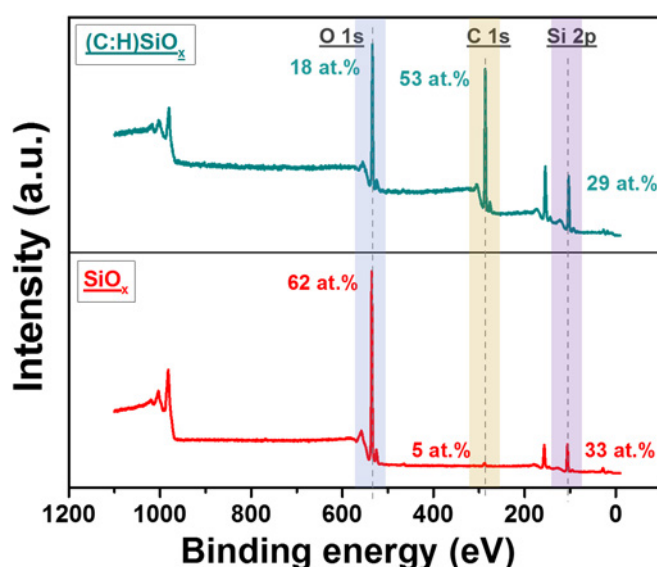


**Figure 57.** XPS wide spectra of the hydrophobic ((C:H)SiO<sub>x</sub>) and hydrophilic (SiO<sub>x</sub>) thin films.

*Nanoparticles.* Plasma polymerization of n-hexane in its mixture with Ar (the ratio of partial pressures 1:27) was employed to synthesize hydrocarbon NPs by GAS. The total pressure was 54 Pa and RF power was set to 70W. SEM images of C:H NPs are presented in Figure 58a. Such polymeric NPs demonstrate well-defined surface structure (see insert) with a NPs mean diameter of  $320\pm 43$  nm. A more detail description of the deposition processes of the polymeric NPs could be found in our previous publications [119,129,130].

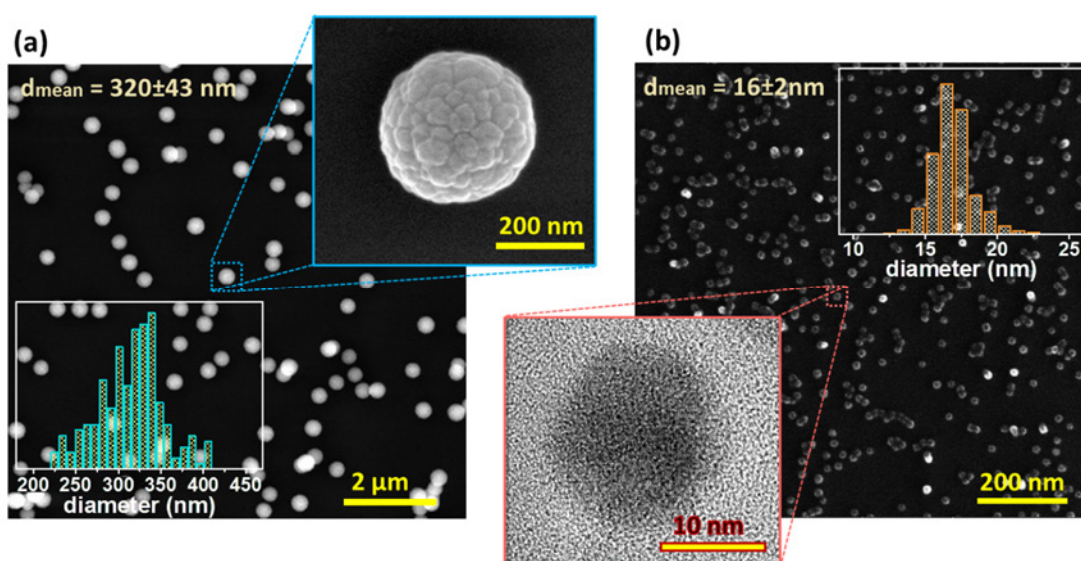


**Figure 58.** SEM images of (a) C:H NPs and (b) Cu NPs with corresponding size distribution and high magnification images (inserts).

In the case of DC-driven magnetron equipped with the copper target, gas aggregation source was utilized for the deposition of Cu NPs. NPs were prepared under the Argon pressure of 48 Pa (flow rate 15,7 sccm) and the current was set to 500 mA. Under given conditions, flux of 370 particles per  $\mu\text{m}^2$  was produced for 1 minute of deposition. The average diameter of the nanoparticles was  $16\pm 2$  nm with relatively narrow size distribution (Figure 58b).

### 4.3.2. Fabrication of the super- hydrophobic/amphiphilic membranes

Surfaces with the water (in air) or oil (under water) CA above  $150^\circ$  and low contact angle hysteresis are considered as the most suitable candidates for water/oil separation. In practice, to fabricate highly efficient membrane both surface roughness and its chemical composition must be properly adjusted.

The transition between wetting regimes could be well explained on the basis of a series of C:H nanoparticles deposited on a flat Si substrate and overcoated with 12 nm of the hydrophobic (C:H)SiO<sub>x</sub> film. According to AFM images in Figure 59, increase of the number of C:H NPs leads to increase of the RMS roughness of the resulted coatings from 21 nm up to 241 nm. Such variation in the roughness of the surface leads to the significant changes in the wetting behavior of the nanocomposites.

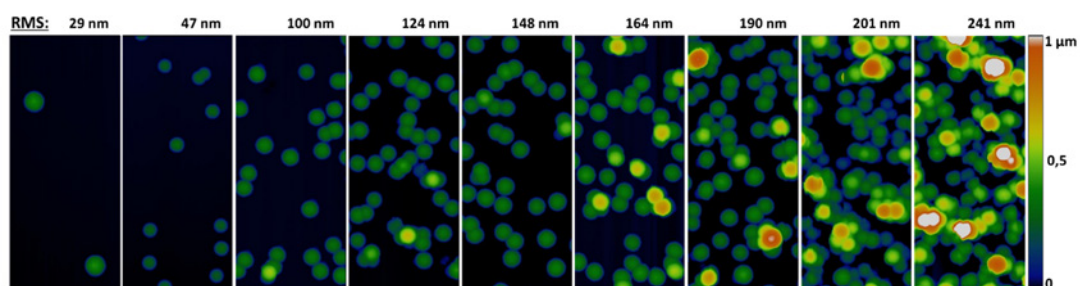


**Figure 59.** AFM images of the C:H particles deposited on Si substrates and overcoated by 12 nm of (C:H)SiO<sub>x</sub> thin film.

In Figure 60 the static and dynamic WCA are presented as a function of the RMS roughness. The static WCA gradually increases from  $105^\circ$  for a nearly flat surface and reaches the maximum of  $162^\circ$  at the maximum of the RMS roughness. The dynamic WCA show more complex dependence on the surface morphology. For surfaces with RMS roughness below 200 nm the difference between the advancing and receding contact angles was significant and so-called high contact angle hysteresis was observed. Such wetting behavior corresponds to Wenzel regime. In this regime water could penetrate inter-particles voids and wet the surface of the coating. In turn, surfaces with RMS roughness above 200 nm are characterized by low contact angle hysteresis, i.e. the difference between the advancing and receding contact angles is negligible and so called Cassie-Baxter regime is achieved. In this case, the inter-

particle voids are small enough to trap air so that water droplets cannot penetrate inside and easily slide away (please, see graphical representation in Figure 30 in experimental section paragraph 3.2.10).

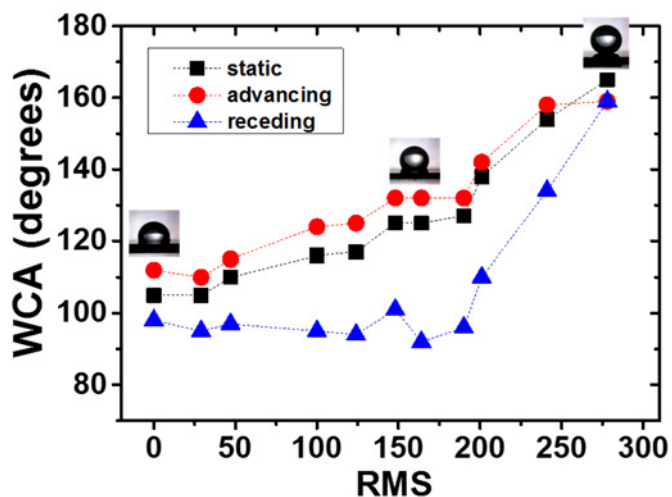


**Figure 60.** Dependence of the static and dynamic WCA on the RMS roughness of the (C:H)SiO<sub>x</sub> thin film.

The opposite wetting scenario is fulfilled if SiO<sub>x</sub> coatings are deposited over the C:H particles. The WCA drops down abruptly from 25° for flat SiO<sub>x</sub> coating to the unmeasurable values even for the smallest amount of the particles used.

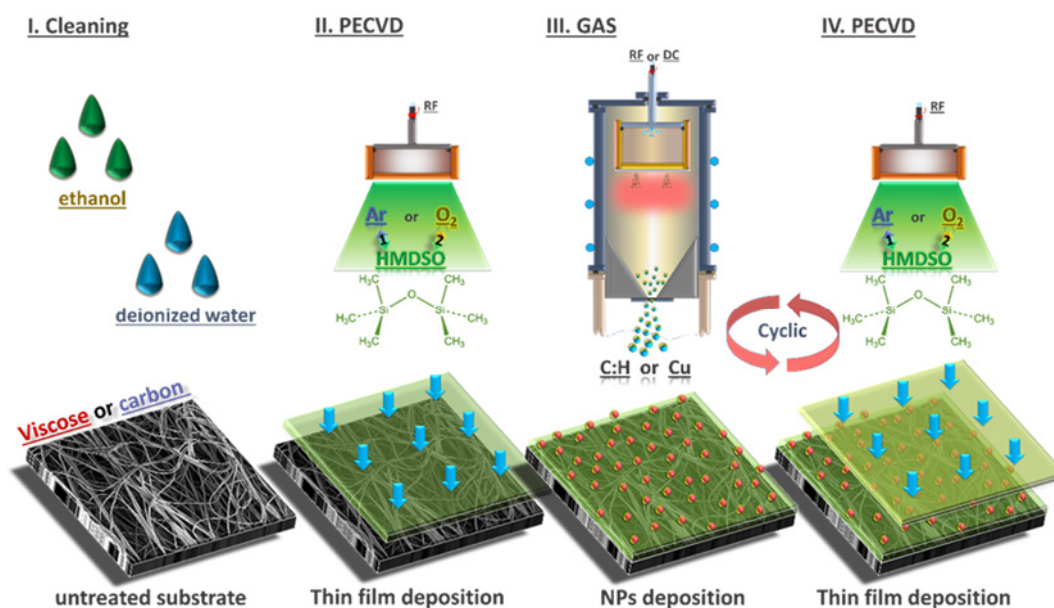


**Figure 61.** Schematic representation of the modification process for selected textiles to obtain membranes with superhydrophobic or superamphiphilic wetting behavior.

In the next step, the nanocomposite coatings were deposited onto textile membranes. Schematic illustration of the modification process is depicted in Figure 61. At first, viscose fabric was ultrasonically cleaned to eliminate possible impurities and properly dry. Such untreated fabric contains a lot of the hydrophilic polar groups, that determine its affinity to water with WCA  $< 1^\circ$ . After covering the entire surface of the viscose fibers with 100 nm (C:H)SiO<sub>x</sub> thin film, wettability is determined by the hydrophobicity of the coating with WCA around  $139 \pm 3^\circ$ . The Wenzel wetting behavior is realized in this case with the WCA hysteresis reaching  $30^\circ$  (advancing and receding WCA are  $146^\circ$  and  $116^\circ$ , respectively). SEM images revealed a well-defined and smooth surface structure for the bare viscose fabric as well as viscose fabric with (C:H)SiO<sub>x</sub> films (see Figure 62 a and b, respectively).

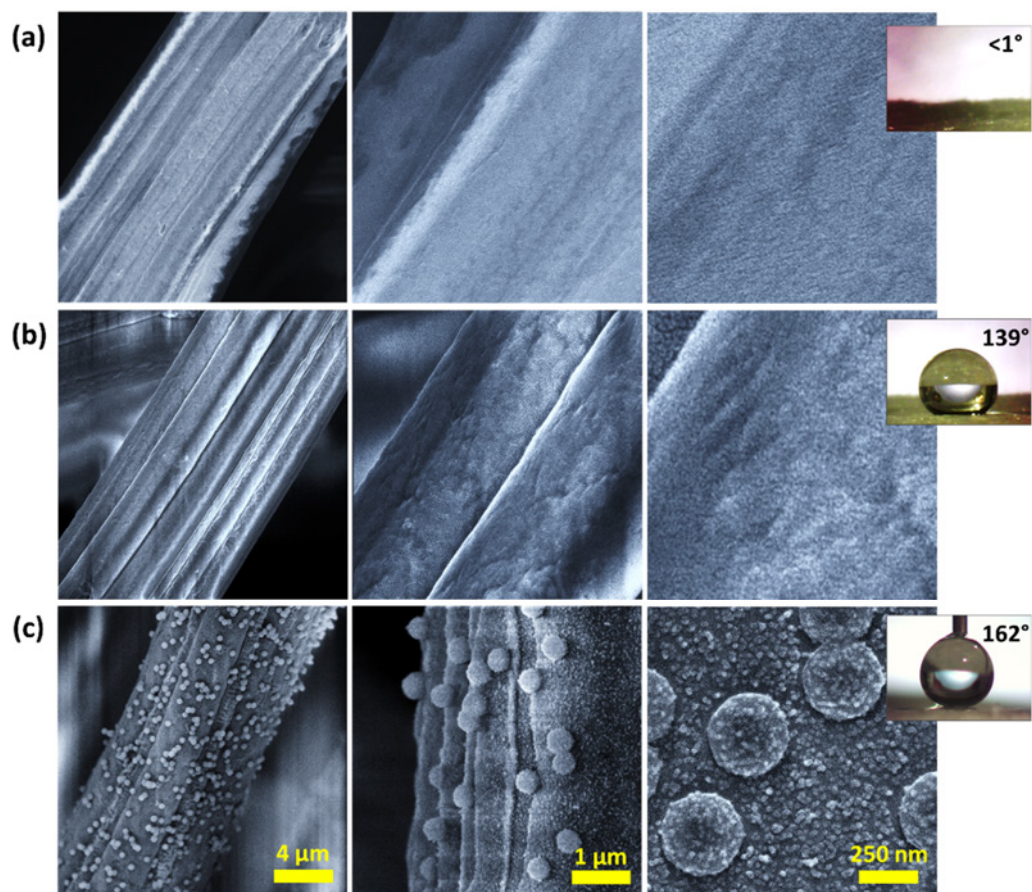


**Figure 62.** SEM images of the viscose fibers: (a) untreated, (b) covered with 100 nm (C:H)SiO<sub>x</sub> thin film, and (c) functionalized with nanocomposite coating.

Further increase in CA assumes an increase in the surface roughness. For this needs, a sufficient amount of CH NPs by GAS was introduced to adjust the surface morphology. Then, the second layer of (C:H)SiO<sub>x</sub> coating (50 nm thick) was deposited to provide a reliable fixation of the NPs. In addition, monolayer of Cu NPs followed by the deposition of the 10 nm (C:H)SiO<sub>x</sub> film was used to introduce antibacterial properties. In this case, SEM images revealed a well-organized nanostructured surface with the uniform distribution of the C:H and Cu NPs on the surface of the viscose fibers (Figure 62c). For such hierarchical membranes, the WCA reached  $162\pm 3^\circ$  with Cassie-Baxter wetting regime (near zero contact angle hysteresis).

The cross-section of the single viscose fiber covered with (C:H)SiO<sub>x</sub>/C:H/Cu film is presented in Figure 63 and show the formation of the 150 nm thick coating on a single fiber.

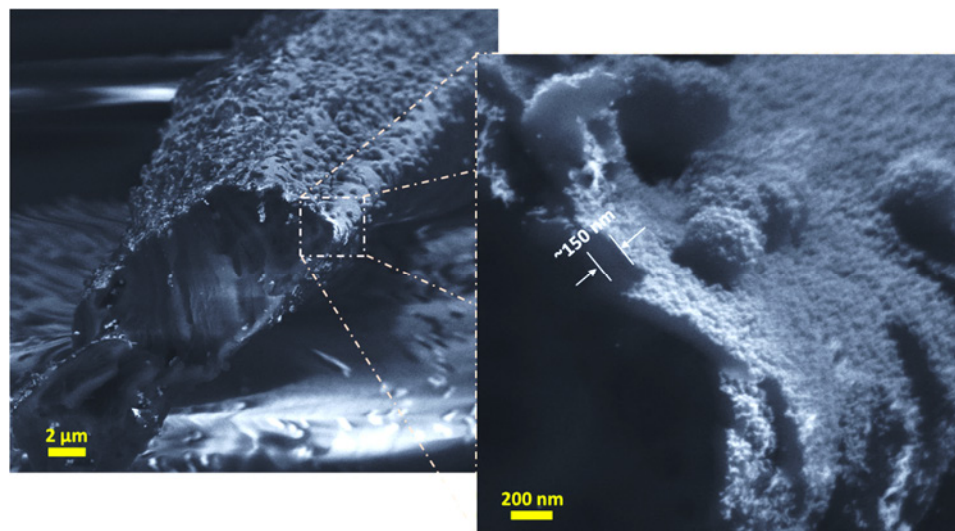


**Figure 63.** Cross-section image of the single viscose fiber covered with (C:H)SiO<sub>x</sub>/C:H/Cu nanocomposite coating.

On the contrary to superhydrophobic Viscose/(C:H)SiO<sub>x</sub>/C:H/Cu membranes, the natural microstructure of carbon cloth with the 100 nm layer of SiO<sub>x</sub> already possess superamphiphilic properties. Such Carbon/SiO<sub>x</sub>/Cu membranes could be completely wetted with water or with oil with the equilibrium contact angle below 1<sup>0</sup>. Similar to the superhydrophobic membrane, an additional layer of Cu NPs was deposited and overcoated with 10 nm SiO<sub>x</sub> film to introduce antibacterial properties. In Figure 64, SEM images of the untreated carbon cloth, as well as carbon cloth functionalized with SiO<sub>x</sub>/Cu coatings, are presented.

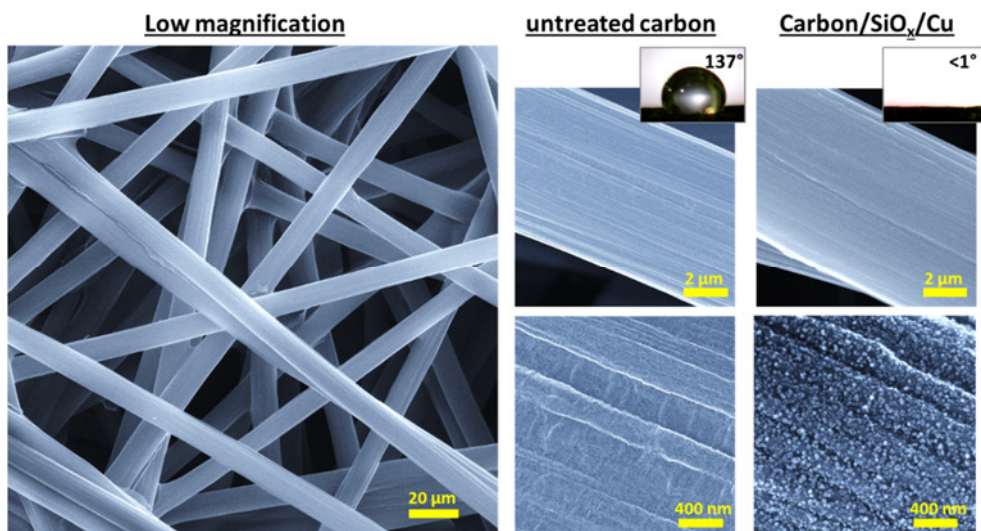


**Figure 64.** SEM images of the carbon cloth (from left to right): low magnification image, untreated carbon cloth, Carbon/ SiO<sub>x</sub>/Cu membrane.

It is worth noting that PECVD allowed the modification of the fibers even in the bulk of the membranes. For example, a stack of ten viscose fabric membranes was treated by the same PECVD in Ar and HMDSO mixture. Figure 65 shows the WCA measured on the surface of each membrane after the deposition of the (C:H)SiO<sub>x</sub> film with layer 1 corresponding to the outermost membrane exposed to the plasma and layer 10 corresponding to the bottom membrane. Obviously, only a slight changes in WCA can be observed with the increasing number of layers.

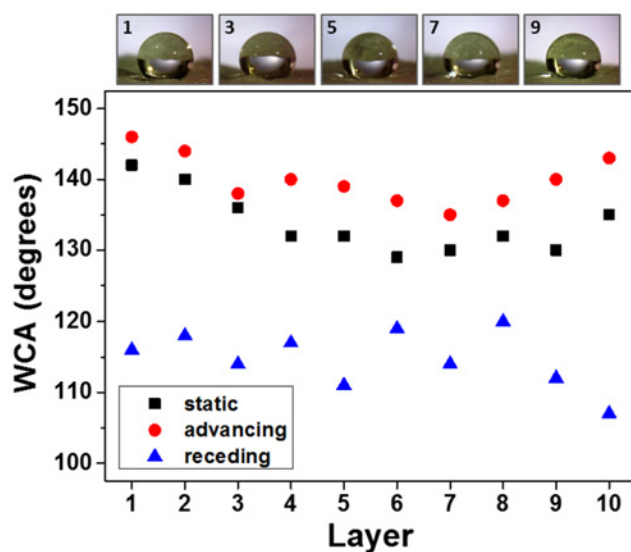


**Figure 65.** Penetration ability of (C:H)SiO<sub>x</sub> coating as a function of WCA and layer of viscose fabric.

### 4.3.3. Selective absorption

Collection of the oil spills from the water was realized through the immersion of the superhydrophobic Viscose/(C:H)SiO<sub>x</sub>/C:H/Cu membrane into the vessel with immiscible water/oil mixture. The absorption process for untreated and functionalized viscose fabric is depicted in Figure 66. For a better representation, water was colored in blue (methylene blue) and oil in red (Oil Red-O). In the case of untreated viscose fabric, the first contact with oil initiates the absorption process and oil starts penetrating into the viscose structure. Subsequently, when the fabric meets water, hydrophilic viscose absorbs water as well. As a result, the simultaneous presence of water and oil phase in the structure of untreated fabric could be observed. In turn, functionalized fabric placed into the water/oil mixture effectively repels water from its surface, whereas silicone oil easily penetrates into the structure. As a consequence, after the collection process, superhydrophobic Viscose/(C:H)SiO<sub>x</sub>/C:H/Cu membrane is completely soaked with oil without any water – selective absorption is obtained.

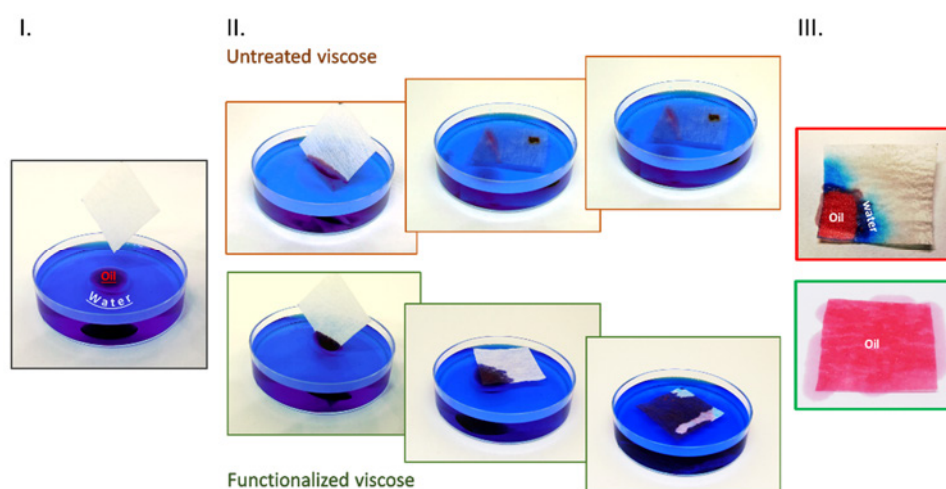


**Figure 66.** The representation of the absorption process of silicone oil from water surface for untreated and functionalized viscose fabric.

The absorption capacity  $k$  was defined as  $(m_{\text{saturated}} - m_{\text{initial}})/m_{\text{initial}}$  to quantitatively evaluate the capability of the Viscose/(C:H)SiO<sub>x</sub>/C:H/Cu membranes to collect oil. Corresponding results for various oils and organic solvents after 7 separation cycles are shown in Figure 67. Herein, one separation cycle corresponds to the absorption process when the membrane is immersed into the water/oil mixture until

it completely soaked with oil than weighed and afterward cleaned in ethanol and dried (at room temperature in the air) so that the clean membrane can be used in the next separation cycle. The absorption capacity  $k$  strongly depends on the nature of organic compounds and after the first separation cycle was 16, 11, 6 and 4 for silicone oil, sunflower oil, benzene and n-hexane respectively. Such a huge difference in the weight gain could be explained by a significant divergence in the viscosity and density of the given organic compounds (Table 1). Simply, liquids with high viscosity tend to retain on the membrane surface more easily. This result is in good agreement with other studies [77].

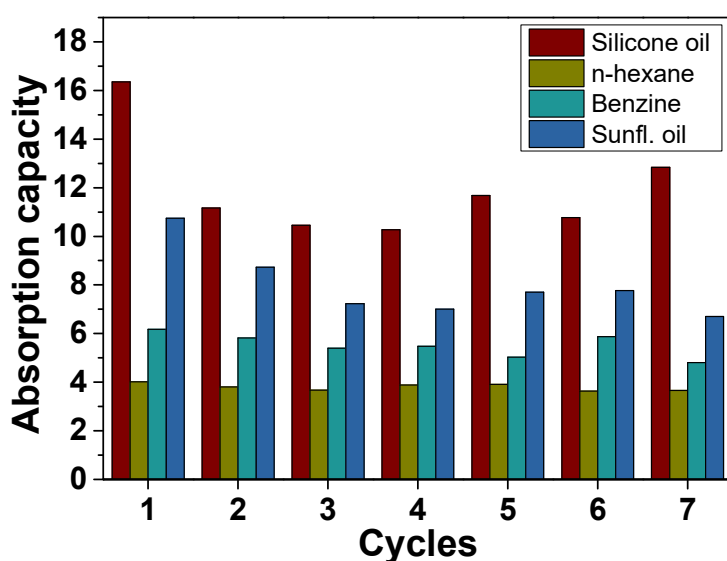


**Figure 67.** Absorption capacity of the membrane for selected organic solvents.

Selected oils	viscosity, Pa*s	density, kg/m <sup>3</sup>	abs. capacity k
<i>silicone oil</i>	0,0965	960	16
<i>sunflower oil</i>	0.0491	919	11
<i>benzine</i>	0.0006	720	6
<i>n-hexane</i>	0.0003	655	4

**Table 1.** Viscosity and density values with respect to absorption capacity  $k$  for selected non-polar compounds.

Also, viscose/(C:H)SiO<sub>x</sub>/C:H/Cu membrane exhibit good recyclability and the absorption capacity  $k$  remains sufficient with increasing separation cycles. This is especially true for compounds with lower viscosity (or density) where adsorption capability is nearly steady with separation cycles. Nevertheless, CA measurements reveal a decrease in the WCA with repeating cycles (Figure 68). Such reduction in the WCA could be attributed to the NPs loss and deterioration of the (C:H)SiO<sub>x</sub> thin film during the mechanical squeezing of the membrane.

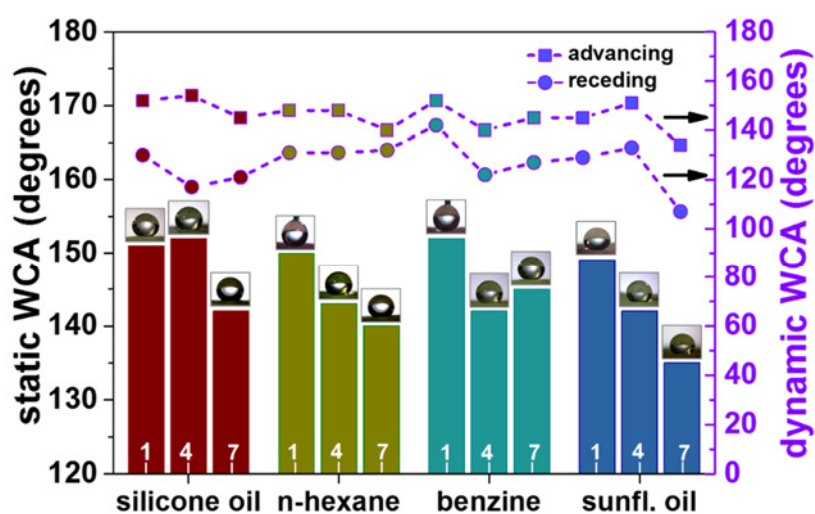


**Figure 68.** Changes in WCA of viscose/(C:H)SiO<sub>x</sub>/C:H/Cu membranes after 1, 4, 7 separation cycles for different oils.

After the 7th circle of separation, ATR-IR spectroscopy was applied to verify collected oil on the presence of the residual water. The absorption spectra for silicone and sunflower oil are shown in Figure 69. Detail analyses revealed that all absorption peaks belong to characteristic vibration bands of the given oils and no bands attributed to water could be identified. As a reference, the absorption spectrum of sunflower oil with 5 wt.% of water is presented as well. In this case, it is easy to distinguish a broad peak with position around 3450 cm<sup>-1</sup>, which corresponds to the vibration bands of O-H groups. It confirms the detection capability of the instrument and the efficacy of the separation process with no water uptake.

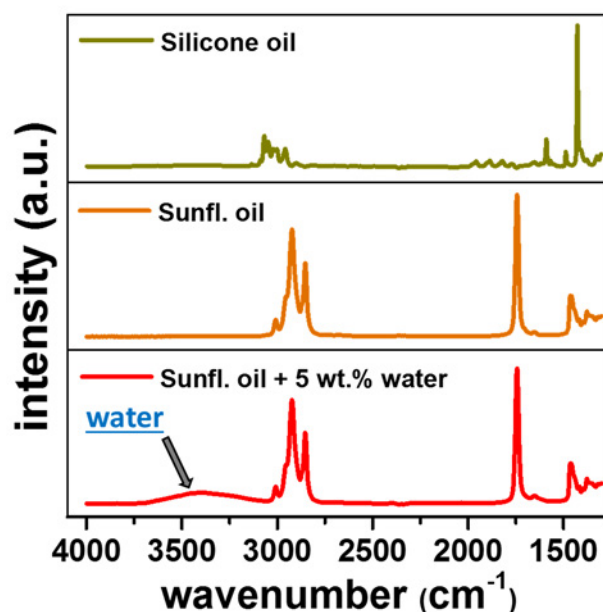


**Figure 69.** ATR spectra of silicone and sunflower oils collected after the 7th cycle of water-oil separation and the corresponding reference spectrum of the sunflower oil with 5 wt% water addition.

#### 4.3.4. Switchable separation.

Schematic illustration of the separation mechanism involving superamphiphilic Carbon/SiO<sub>x</sub>/Cu membranes is shown in Figure 71 (a) and (b). Depending on the prewetting with water or heavy oil, switchable separation of the membrane could be realized. With water prewetting, Carbon/SiO<sub>x</sub>/Cu membrane exhibit underwater superoleophobic behavior and is suitable for the separation of light oil/water mixture, whereas prewetting with heavy oil provides the efficient separation of the heavy oil/water mixture. The contact angles for different oils underwater, as well as water droplet under heavy oil, were above 150° with nearly zero adhesion to membrane surface (Figure 70). Such an underwater superoleophobic or underoil superhydrophobic wetting regimes are described by the Cassie-Baxter equation for three-phase solid-liquid<sub>1</sub>-liquid<sub>2</sub> interface as it was discussed in the experimental section [115].

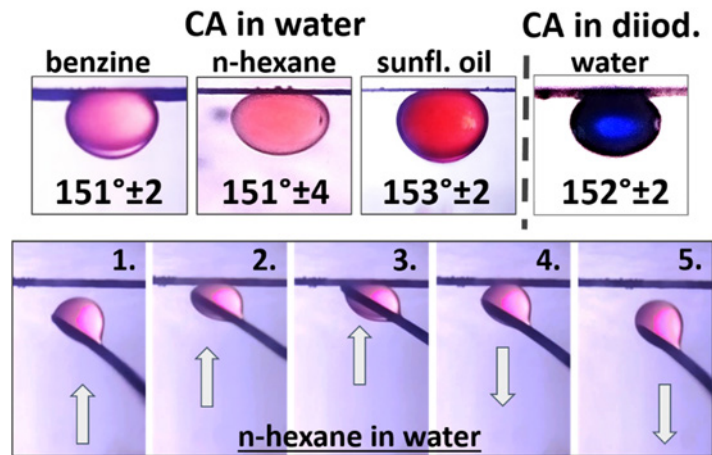


**Figure 70.** The contact angle of the selected oils (benzine, n-hexane, sunflower oil) in water and water in diiodomethane (top), and the slippery effect demonstrated by the n-hexane droplet on the surface of Carbon/SiO<sub>x</sub>/Cu membrane immersed into the water (bottom).

The separation process was started by pouring the mixture of water with light or heavy oil (1:1 wt.%) into the separation setup as it is depicted in Figure 71 (c) and (d) respectively. For better representation oil was dyed red (Oil Red O) and prior to the separation Carbon/SiO<sub>x</sub>/Cu membrane was prewetted with water ( $\rho_{oil} < \rho_{water}$ ) or oil ( $\rho_{oil} < \rho_{water}$ ). In the case of  $\rho_{oil} < \rho_{water}$ , oil segregates on the top layer of the mixture due to water/oil phase separation and water could easily pass through the membrane. In this case, trapped water in the porous structure of the membrane makes efficient support for oil and prevents it from entering the membrane [131]. Consequently, the membrane effectively separates water, whereas light oil remains in the separation tube. It is easy to continue the separation process simply pouring the additional portion of water to the remaining oil.

After the cleaning in ethanol and drying, the same membrane was employed for the separation of heavy oil/water mixture. In this case, prewetting with heavy oil allows diiodomethane penetrate through membrane whereas water was effectively repelled from the membrane surface. It is noteworthy that the separation process was completely gravity driven for both separation regimes. Also, the original carbon paper was tested for the separation of oil/water mixture as a control. At the initial stages of the separation, small amount of oil could pass through the untreated carbon paper. However, due to oil/water phase separation, the water settles beneath the oil preventing

oil contact with the membrane and thus leads to the stoppage of the segregation process.

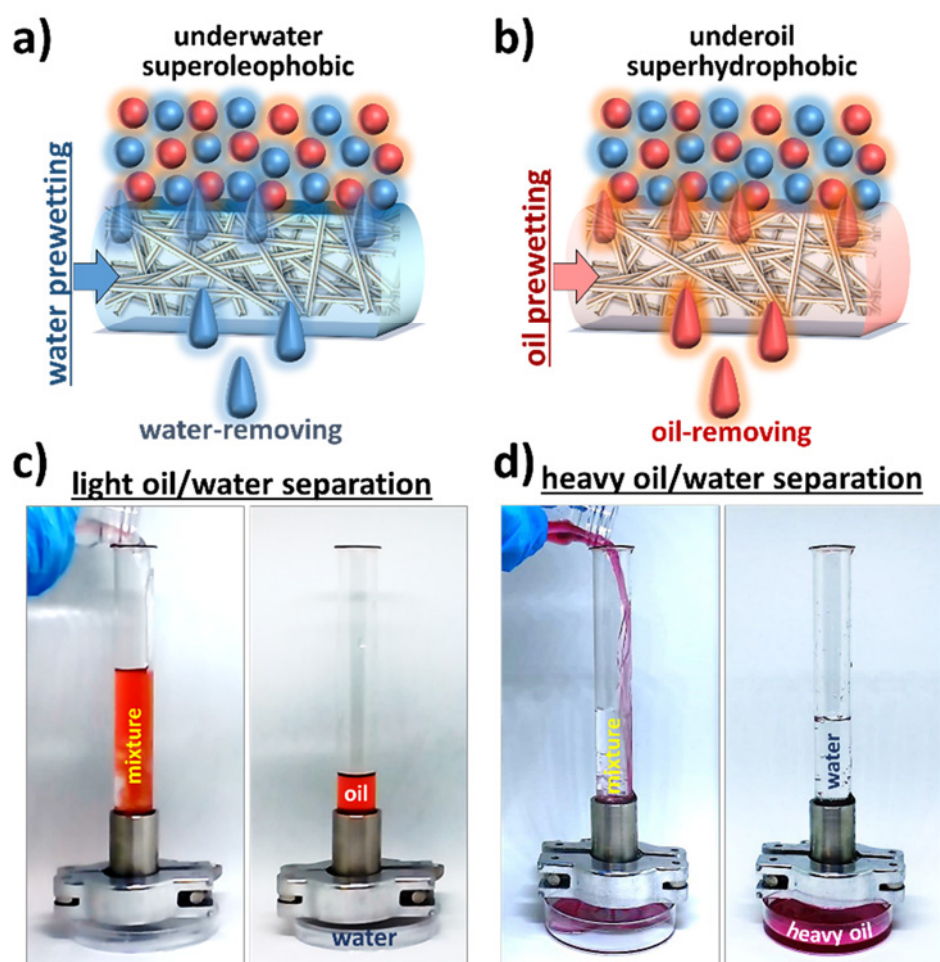


**Figure 71.** Schematic illustration of the separation mechanism with: (a) underwater superoleophobicity and (b) underoil superhydrophobicity, and the corresponding images of the separation process for (c) water-removing and (d) oil-removing regimes.

The concentration of the residual oil or water in the collected liquids was determined using UV-Vis spectrophotometry as it is discussed in the experimental section. The calculated efficiency of the separation process is presented in Figure 72a. It was found that SiO<sub>x</sub>/Cu membrane exhibit high separation ability with efficiency above 99.97% for both water mixtures with either light or heavy oil. To evaluate the recyclability of the Carbon/SiO<sub>x</sub>/Cu membranes, the same membrane was used for the filtration of benzene, n-hexane, sunflower oil/water mixtures for 10 separation cycles

each (after each cycle of separation, the membrane was cleaned in ethanol and dried). According to Figure 72b, efficiency greater than 99.99% was obtained for light oils in all separation cycles.

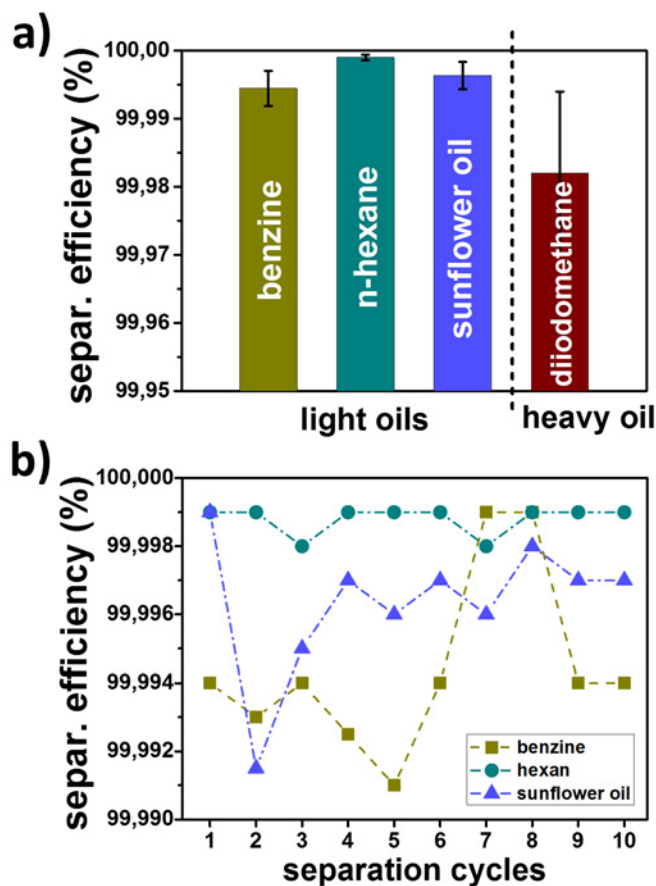


**Figure 72.** (a) Separation efficiency for selected oil/water mixtures. (b) The separation efficiency of light oil/water mixtures as a function of separation cycles.

In order to evaluate the practical potential of the superamphiphilic membranes, the speed of separation and intrusion pressure were determined experimentally. The flux of the water or oil through Carbon/SiO<sub>x</sub>/Cu membrane was calculated through the equation:

$$F = V/St \quad (25)$$

where  $V$  is the volume of the filtrate permeates through the membrane,  $S$  - area of the effective surface of the membrane,  $t$  is time for which liquid pass through the Carbon/SiO<sub>x</sub>/Cu.

In the case of the water-removing regime, water permeates membrane with flux  $81900 \text{ Lm}^{-2} \text{ h}^{-1}$ . Whereas the flux of heavy oil (diiodomethane) was estimated to be similar or higher than that of water. Subsequently, the intrusion pressure ( $P$ ) was calculated as a function of maximum height ( $h_{max}$ ) of the oil or water which membrane could support before breakthrough as follows:

$$P = \rho g h_{max} \quad (26)$$

where  $\rho$  is the density of filtrate liquid,  $g$  is the gravitational acceleration.

It was found that the intrusion pressure for water-removing and oil-removing regimes were 2.43 kPa and 1.7 kPa respectively. In other words,  $h_{max}$  of 27 cm and 17 cm for sunflower oil and diiodomethane correspond to the maximum column of the liquid in the separation vessel before oil or water permeates the membrane. In our opinion, such a combination of the flux and intrusion pressure is optimal for fast fail-free separation process with perspective to be used in industrial applications.

#### 4.3.5. Antibacterial activity of filtration membranes

In Figure 73 the fluorescent signal produced by alamarBlue viable reagent is represented as a proven indicator of the metabolic activity of *E. coli* bacteria incubated with the untreated and functionalized viscose fabric. For bare fabric, the signal remains relatively constant during the 24 h period of incubation indicating good viability and health of the bacteria. In the case of Viscose/(C:H)SiO<sub>x</sub>/C:H/Cu, a little decrease in metabolic activity was observed, whereas superamphiphilic Viscose/SiO<sub>x</sub>/Cu shows nearly 50% reduction in viability after 24 h. Since the fluorescent signal is proportional to the number of living *E. coli* bacteria, such reduction in produced signal corresponds to a growing number of the damaged and nonviable bacteria. The XPS measurements reveal nearly identical copper content of 0.6 and 0.7 at.% for Viscose/SiO<sub>x</sub>/Cu and Viscose/(C:H)SiO<sub>x</sub>/C:H/Cu samples respectively. Thus, the difference in antibacterial activity between superamphiphilic and superhydrophobic membranes could be explained by poor ion release of the latter. In other words, the (C:H)SiO<sub>x</sub> hydrophobic

film serve as a barrier layer restricting the interaction of Cu NPs with an aqueous medium. Hence much lower ion release is achieved and a smaller number of copper ions could reach bacteria [109].

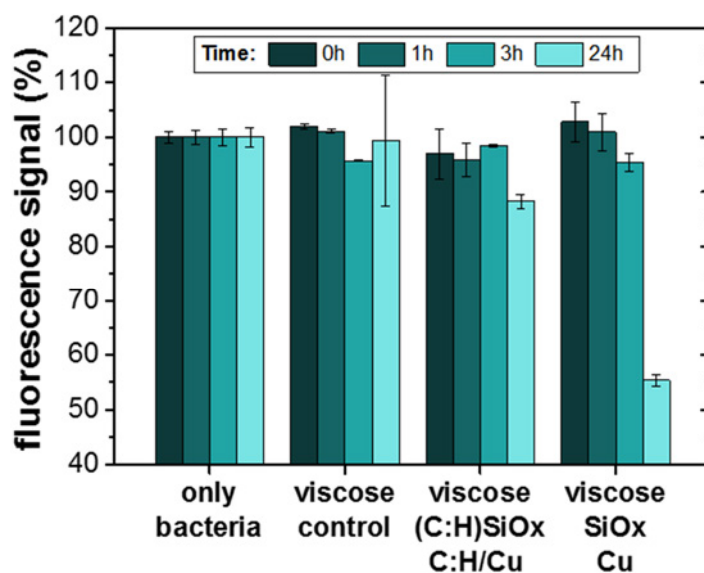


**Figure 73.** Metabolic activity of *E. coli* bacteria incubated on superhydrophobic Viscose/(C:H)SiO<sub>x</sub>/C:H/Cu and superamphiphilic Viscose/SiO<sub>x</sub>/Cu membranes.

The necessary antibacterial activity and the biocompatibility of the prepared membranes could be adjusted by tailoring the number of Cu NPs embedded into the functional nanocomposite coating or varying the thickness of the diffusion barrier layer, as it was shown in our previous studies [108,109,132].

## 4.4. Interlanthanide perovskites

In this chapter of the thesis, I would like to present the experimental results obtained during my stay in the Ceramics Processing Group (National Institute for Materials Science (NIMS), Japan) under the “Charles University - NIMS Cooperative Graduate School Program”. The synthesis of the ceramics and the majority of the related measurements were conducted on the equipment available at the Ceramics Processing Group. In addition, XRD measurements were conducted at the Research Network and Facility Services Division. Whereas access to the SEM instrument was provided at the Materials Analysis Station.

### 4.4.1. LSYO perovskites

Sr-doped  $\text{LaYO}_3$  (LSYO) perovskite considered to be a promising candidate for implementation as an electrolyte material in an intermediate temperature solid oxide fuel cells (SOFCs) [133–135]. Along with satisfactory proton conductivity, such an interlanthanide perovskite exhibit high stability to carbon dioxide during the operation in SOFC. In general, the substitution of Sr for La in  $\text{LaYO}_3$  leads to the formation of oxygen vacancies in perovskite structure that contributes to proton transfer by so-called hopping mechanism. Hence, a single phase orthorhombic structure of  $\text{LaYO}_3$  is preferable to obtain electrolytes with high conductivity. However, the synthesis of such materials is rather limited to some combustion methods that are harmful to the environment (release  $\text{NO}_x$  gasses). In this study, highly sinterable  $\text{La}_{0.9}\text{Sr}_{0.1}\text{YO}_3$  perovskites were obtained by a solid-state reaction method – an environmentally friendly technique.

LSYO was synthesized by mixing high purity (99.9 %) Lanthanum (III) hydroxide ( $\text{La}(\text{OH})_3$ ), Yttrium (III) oxide ( $\text{Y}_2\text{O}_3$ ) and Strontium carbonate ( $\text{SrCO}_3$ ). The weighed powders were mixed with ethanol for 6 hours, dried, pressed (40 MPa) and calcined at 1400 °C for 8 hours in the air. Prior to the sintering process samples were subjected to planetary ball milling for 10 hours at 200 rpm. SEM images revealed a decrease in the particle size after milling as it is shown in Figure 74. Powder mixtures were then molded under the pressure of 40 MPa and hydrostatically pressed at 392

MPa for 10 min. Subsequently, sintering of the samples took place at 1350 °C for 10 hours. The heating and cooling rates were 10 °C/min.

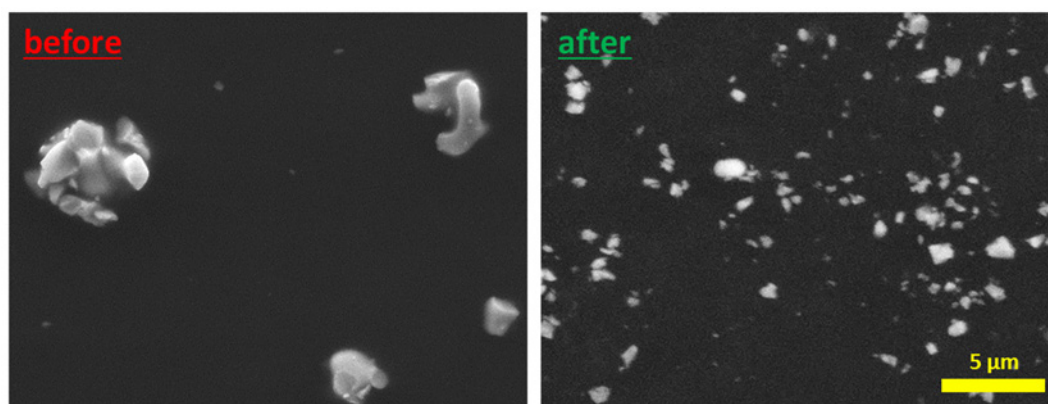


**Figure 74.** SEM images of particles before and after 8 hours planetary ball milling.

It is well known that  $\text{LaYO}_3$  form orthorhombic perovskite-type structure at the temperature below 1500 °C and monoclinic B-type rare earth structure at elevated temperatures [135,136]. Thus, the temperature regimes for calcination and sintering were chosen in such a way to obtain LSYO with orthorhombic structure and at the same time achieve high sinterability of the powder mixtures.

MiniFlex X-ray diffraction (XRD, Rigaku) with monochromatic  $\text{CuK}\alpha$  radiation was used to determine the crystal structure of the LSYO samples. XRD patterns for LSYO after calcination and sintering are presented in Figure 75. It could be seen that after 10 hours of calcination at 1400 °C small tracks of impurity phases can be detected for LSYO samples. However, after 10 hours sintering at 1350 °C a single-phase perovskite structure was obtained.

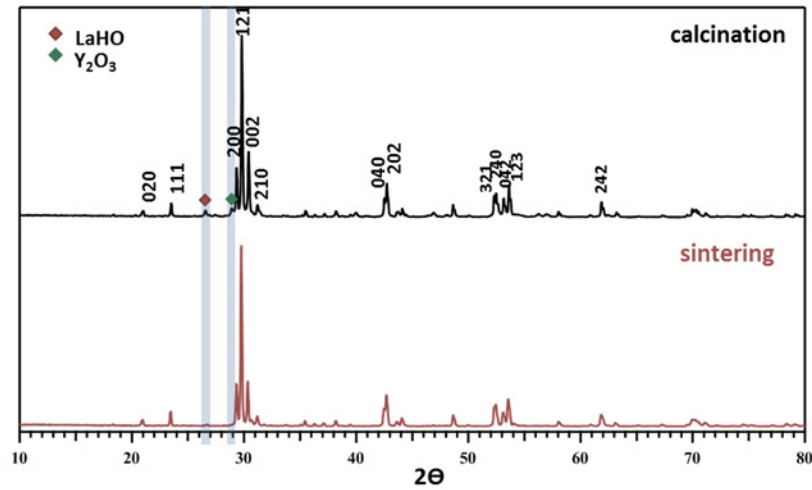


**Figure 75.** XRD pattern of LSYO after calcination at 1400 °C for 10 hours and sintering at 1350 °C for 10 hours.

In Figure 76, SEM image of the LSYO compact after sintering and polishing. Ceramics exhibit well-textured structure with the average grain size of 635 nm. The density of the selected samples was determined by the Archimedes method and was around 96% of the theoretical value. To conclude, highly sinterable ceramic was successfully synthesized by a solid-state reaction method.

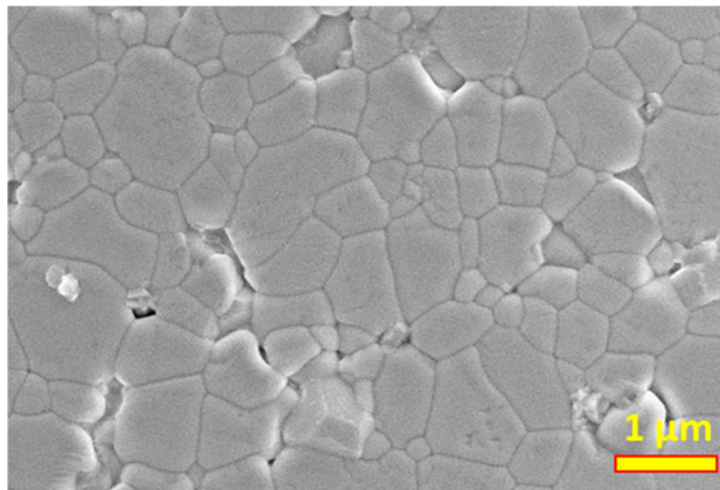


**Figure 76.** SEM image of the LSYO fabricated ceramics after the polishing process.

## 5. Conclusions

In this thesis, non-equilibrium low-pressure plasma was utilized for the treatment of porous materials to introduce new properties and/or improve those already existing. The study opens new insights into the field of NPs deposition, functional nanocomposite coatings and plasma interaction with porous structures.

The work can be summarized as follows:

- *Deposition of metallic NPs by GAS.*

The fabrication of Ag and Cu nanoparticles was studied in dependence on the deposition parameters in the GAS. Special attention was given to the effect of the adjustable magnetic field on the formation of Cu nanoparticles. It was found, that changes in the magnetic field intensity above the target strongly affects the size and shape of produced NPs as well as their deposition rate. Maximum of the deposition rate was reached for magnetic field 45 mT at magnetron current 400 mA and pressure 100 Pa. Presence of large complex agglomerated NPs with sizes up to 150 nm was observed at these conditions. The electromagnetic trapping in the close vicinity to the magnetron is proposed to be responsible for the formation of such large NPs.

- *Hard Ag/a-C:H nanocomposites.*

An original approach was developed for the fabrication of hard Ag/a-C:H nanocomposite coatings. The deposition process is based on the simultaneous deposition of Ag NPs by GAS and thin film deposition by PECVD. The strategy allows independent control of the matrix properties and the amount of embedded NPs so that mechanical and antibacterial properties of the coatings can be properly tuned.

- *Surface enrichment by plasma etching.*

Three types of low-pressure plasma etching were tested to increase surface silver concentration on hard Ag/a-C:H nanocomposites. The best results for biomedical applications were reached in case of the etching in oxygen plasma with grounded samples. This process showed the best selectivity of the etching and thus the highest Ag concentration on the surface was reached. Furthermore, oxygen etching was shown to be capable to improve antibacterial activity of produced nanocomposites due to Ag

surface enrichment. This is highly important result as it shows that it is possible to lower the amount of Ag NPs in the bulk of nanocomposites, which is needed to assure good mechanical properties of produced films, but maintain their sufficiently high initial antibacterial activity.

- *Nanostructured composite coatings with adjustable wettability.*

A gas-phase step-by-step deposition process was used for the fabrication of nanostructured coatings with the wettability ranging from superhydrophilic to superamphiphilic. PECVD from hexamethyldisiloxane was used for the deposition of thin films of either organosilicon plasma polymer or silicon dioxide by mixing the precursor with argon or oxygen. The films were combined with particles of C:H plasma polymer and/or with Cu nanoparticles. This approach allows the independent control of the surface roughness and the chemical composition of the functional nanocomposite coatings. As a result, functional coatings with a wide range of wettability were fabricated.

- *Super-wettable filtration membranes.*

Fabricated super-wettable nanostructured coatings were successfully utilized for the modification of porous non-woven viscose fabric and carbon cloth to be used for water purification. Super-hydrophobic membranes were prepared by depositing organosilicon plasma polymer with C:H and Cu NPs onto viscose fabric. The membranes were utilized for the selective absorption of non-polar organic solvents from water. The absorption capability was shown to depend strongly on the nature of organic compounds.

Super-amphiphilic membranes were prepared by deposition of silicon dioxide layers and Cu NPs onto carbon cloth. Such membranes could be used for the gravity-driven separation of water from light oil/water mixtures as well as for the separation of oil from heavy oil/water mixtures depending on the liquid used for prewetting of the membranes. The separation efficiency 99.99% and 99.97% was achieved for the water-removing and oil-removing regimes and the intrusion pressure of 2.43 kPa for water and 1.70 kPa for oil was found out.

Super-amphiphilic viscose membranes exhibit antibacterial properties due to the release of Cu ions. A two-fold reduction in the metabolic activity of *E.coli* bacteria was observed after 24 h of the incubation period.

The proposed modification mechanism is presented as a proof of concept that offers a flexible approach enabling fabrication of various functional nanocomposite materials. We believe that such bacteria non-fouling filtration membranes have a potential to be used in industrial applications and could bring new possibilities in the field of water purification. For example, superamphiphilic membranes could be used as an effective and flexible solution for dual-membrane systems where water and oil are separated simultaneously.

## Bibliography

- [1] P. S. Liu, G. F. Chen, *Porous Materials: Processing and Applications*, Elsevier, 2014.
- [2] A. D. Mc Naught, A. Wilkinson, *IUPAC. Compendium of Chemical Terminology, 2nd Ed. (the "Gold Book")*, Scientific Publications, Oxford, 1997.
- [3] M.-H. Sun, S.-Z. Huang, L.-H. Chen, Y. Li, X.-Y. Yang, Z.-Y. Yuan, B.-L. Su, *Chem. Soc. Rev.* 2016, 45, 3479.
- [4] A. Zille, F. R. Oliveira, A. P. Souto, *Plasma Process. Polym.* 2015, 12, 98.
- [5] M. Petr, O. Kylián, J. Hanuš, A. Kuzminova, M. Vaidulych, I. Khalakhan, A. Choukourov, D. Slavínská, H. Biederman, *Plasma Process. Polym.* 2016, 663.
- [6] H. Biederman, O. Kylian, M. Drabik, A. Choukourov, O. Polonskyi, P. Solar, *Surf. Coatings Technol.* 2012, 211, 127.
- [7] J. Hanus, M. Drabik, P. Hlidek, H. Biederman, G. Radnoczi, D. Slavinska, *Vacuum* 2008, 83, 454.
- [8] A. Kuzminova, A. Shelemin, O. Kylián, M. Petr, J. Kratochvíl, P. Solař, H. Biederman, *Vacuum* 2014, 110, 58.
- [9] O. Polonskyi, P. Solař, O. Kylián, M. Drábik, A. Artemenko, J. Kousal, J. Hanuš, J. Pešička, I. Matolínová, E. Kolíbalová, D. Slavínská, H. Biederman, *Thin Solid Films* 2012, 520, 4155.
- [10] J. Hanus, J. Kousal, A. Choukourov, H. Biederman, D. Slavinska, *Plasma Process. Polym.* 2007, 4, 806.
- [11] Y. Pihosh, H. Biederman, D. Slavinska, J. Kousal, A. Choukourov, M. Trchova, A. Mackova, A. Boldryeva, *Vacuum* 2006, 81, 38.
- [12] A. Shelemin, D. Nikitin, A. Choukourov, O. Kylián, J. Kousal, I. Khalakhan, I. Melnichuk, D. Slavínská, H. Biederman, *J. Phys. D Appl. Phys.* 2016, 49, 254001 (10pp).
- [13] A. Choukourov, P. Pleskunov, D. Nikitin, V. Titov, A. Shelemin, M. Vaidulych, A. Kuzminova, P. Solar, J. Hanuš, J. Kousal, O. Kylián, D. Slavínská, H. Biederman, *Beilstein J. Nanotechnol.* 2017, 8, DOI 10.3762/bjnano.8.200.
- [14] I. Langmuir, *Proc. Natl. Acad. Sci. U.S.A.* 1928, 14, 627.
- [15] A. Fridman, *Plasma Chemistry*, Cambridge University Press, Cambridge, 2008.
- [16] H. Biederman, *Plasma Polymer Films*, Imperial College Press, London, 2004.

- [17] F. Paschen, *Ann. Phys.* 1889, 273, 69.
- [18] H. Biederman, Y. Osada, *Plasma Polymerization Processes*, Elsevier, Amsterdam, 1992.
- [19] J. A. Thornton, R. F. Bunshan, *Deposition Technologies for Films and Coatings*, Noyes Publications (USA), 1982.
- [20] H. S. Butler, G. S. Kino, *Phys. Fluids* 1963, 6, 1346.
- [21] H. Carchano, *J. Chem. Phys.* 1974, 61, 3634.
- [22] M. Ataefard, S. Moradian, M. Mirabedini, M. Ebrahimi, S. Asiaban, *Prog. Org. Coatings* 2009, 64, 482.
- [23] E. Wohlfart, J. P. Fernández-Blázquez, E. Knoche, A. Bello, E. Pérez, E. Arzt, A. Del Campo, *Macromolecules* 2010, 43, 9908.
- [24] J. A. Thornton, *Annu. Rev. Mater. Sci.* 1977, 7, 239.
- [25] Yves Huttel, *Gas-Phase Synthesis of Nanoparticles Edited by Yves Huttel*, Wiley-VCH, Weinheim, Germany, 2017.
- [26] P. J. Kelly, R. D. Arnell, *Vacuum* 2000, 56, 159.
- [27] D. W. Hoffman, *J. Vac. Sci. Technol. A* 1994, 12, 953.
- [28] M. L. Escrivão, P. J. S. Pereira, M. H. Cabral, M. R. Teixeira, M. J. P. Maneira, *J. Vac. Sci. Technol. A* 2003, 21, 375.
- [29] E. Bultinck, A. Bogaerts, *J. Phys. D Appl. Phys.* 2008, 41, 202007.
- [30] J. Li, Q.-M. Chen, W. Zhang, Z.-G. Li, J. J. Pan, *J. Phys. D Appl. Phys.* 1996, 29, 1624.
- [31] W. D. Westwood, S. Maniv, P. J. Scanlon, *J. Appl. Phys.* 54 1983, 54, 6841.
- [32] M. Keidar, S. Member, I. I. Beilis, S. Member, *IEEE Trans. Plasma Sci.* 2006, 34, 804.
- [33] A. V Rogov, Y. V Kapustin, Y. V Martynenko, *Tech. Phys.* 2015, 60, 283.
- [34] E. Blanchard, B. Hanselmann, J. Drost, M. Heuberger, D. Hegemann, *Plasma Process. Polym.* 2015, 12, 32.
- [35] B. Cortese, D. Caschera, F. Federici, M. Ingo, G. Gigli, *J. Mater. Chem. A* 2014, 2, 6781.
- [36] S. Kwon, T. Ko, E. Yu, J. Kim, M. Moon, C. H. Park, *RSC Adv.* 2014, 4, 45442.
- [37] T. Williams, M. W. Hayes, *Nature* 1966, 209, 769.
- [38] A. R. Westwood, *Eur. Polym. J.* 1971, 7, 363.
- [39] J. M. Tibbitt, R. Jensen, A. T. Bell, M. Shen, *Macromolecules* 1977, 10, 647.

- [40] D. K. Lam, R. F. Baddour, A. F. Stancell, *Plasma Chemistry of Polymers*, Marcel. Dekker Inc., New York, 1976.
- [41] H. Yasuda, *Plasma Polymerization*, Academic Press, Orlando, Florida, 1985.
- [42] H. Yasuda, C. E. Lamaze, *J. Appl. Polym. Sci.* 1971, 15, 2277.
- [43] M. Gazicki, H. Yasuda, *Plasma Chem. Plasma Process.* 1983, 3, 279.
- [44] A. C. Ferrari, J. Robertson, *Philos. Trans. R. Soc. A Math. Phys. Eng. Sci.* 2004, 362, 2477.
- [45] P. Grammatikopoulos, S. Steinhauer, J. Vernieres, V. Singh, M. Sowwan, *Adv. Phys. X* 2016, 1, 81.
- [46] A. D. Kramar, B. M. Obradovi, A. Vesel, M. M. Kuraica, M. M. Kosti, *Plasma Process. Polym.* 2015, 12, 1095.
- [47] L. Martínez, M. Díaz, E. Román, M. Ruano, D. L. P., Y. Huttel, *Langmuir* 2012, 28, 11241–11249.
- [48] J. Hanuš, M. Vaidulych, O. Kylián, A. Choukourov, J. Kousal, I. Khalakhan, M. Cieslar, P. Solař, H. Biederman, *J. Phys. D. Appl. Phys.* 2017, 50, 475307.
- [49] M. Vaidulych, J. Hanuš, T. Steinhartová, O. Kylián, A. Choukourov, J. Beranová, I. Khalakhan, H. Biederman, *Plasma Process. Polym.* 2017, 14, 1600256.
- [50] O. Kylián, J. Kratochvíl, J. Hanuš, O. Polonskyi, P. Solař, H. Biederman, *Thin Solid Films* 2014, 550, 46.
- [51] J. Wedekind, A.-P. Hyvärinen, D. Brus, D. Reguera, *PRL* 2008, 101, 125703.
- [52] P. V Kashtanov, B. M. Smirnov, R. Hippler, *Phys. - Uspekhi* 2007, 50, 455.
- [53] K. Wegner, P. Piseri, H. V. Tafreshi, P. Milani, *J. Phys. D Appl. Phys.* 2006, 39, R439.
- [54] W. A. De Heer, *Rev. Mod. Phys.* 1993, 65, 612.
- [55] C. Binns, *Surf. Sci. Rep.* 2001, 44, 1.
- [56] H. Haberland, M. Karrais, M. Mall, Y. Thurner, *J. Vac. Sci. Technol. A* 1992, 10, 3266.
- [57] S. D. Ekpe, F. J. Jimenez, D. J. Field, M. J. Davis, S. K. Dew, *J. Vac. Sci. Technol. A* 2009, 27, 1275.
- [58] J. Goree, T. E. Sheridan, *Appl. Phys. Lett.* 1991, 59, 1052.
- [59] H. Biederman, *Vacuum* 1984, 34, 405.
- [60] E. Kay, A. Dilks, U. Hetzler, *J. Macromol. Sci. Part A - Chem.* 1978, 12, 1393.

- [61] N. Boonthanom, M. White, *Thin Solid Films* 1974, 24, 295.
- [62] A. Choukourov, O. Kylián, M. Petr, M. Vaidulych, D. Nikitin, J. Hanuš, A. Artemenko, A. Shelemin, I. Gordeev, Z. Kolská, P. Solař, I. Khalakhan, A. Ryabov, J. Májek, D. Slavínská, H. Biederman, *Nanoscale* 2017, 9, 2616.
- [63] D. Hegemann, M. M. Hossain, E. Ko, D. J. Balazs, *Plasma Process. Polym.* 2007, 4, 229.
- [64] J. Michel, E. H. Owens, S. Zengel, A. Graham, Z. Nixon, T. Allard, W. Holton, P. D. Reimer, A. Lamarche, M. White, N. Rutherford, C. Childs, G. Mauseth, G. Challenger, E. Taylor, *PLoS One* 2013, 8, 1.
- [65] B. Dubansky, A. Whitehead, T. Miller, C. D. Rice, F. Galvez, *Environ. Sci. Technol.* 2013, 47, 5074.
- [66] B. Wang, W. Liang, W. Liu, *Chem. Soc. Rev.* 2014, 44, 336.
- [67] Z. Xue, Y. Cao, N. Liu, L. Feng, L. Jiang, *J. Mater. Chem. A* 2014, 2, 2445.
- [68] Z. Chu, Y. Feng, S. Seeger, *Angew. Chem. Int. Ed.* 2015, 54, 2328.
- [69] L. Feng, Z. Zhang, Z. Mai, Y. Ma, B. Liu, L. Jiang, D. Zhu, *Angew. Chem. Int. Ed.* 2014, 43, 2012.
- [70] X. Zhang, Z. Li, K. Liu, L. Jiang, *Adv. Funct. Mater.* 2013, 23, 2881.
- [71] W. Zhang, Z. Shi, F. Zhang, X. Liu, J. Jin, L. Jiang, *Adv. Mater.* 2013, 25, 2071.
- [72] S. Gao, J. Sun, P. Liu, F. Zhang, W. Zhang, S. Yuan, *Adv. Mater.* 2016, 28, 5307.
- [73] S. K. Hong, S. Bae, H. Jeon, M. Kim, S. J. Cho, G. Lim, *Nanoscale* 2018, 10, 3037.
- [74] J. Yong, F. Chen, Q. Yang, J. Huoa, X. Houa, *Chem. Soc. Rev.* 2017, 46, 4168.
- [75] Y. Wang, X. Gong, *J. Mater. Chem. A* 2017, 5, 3759.
- [76] L. Zhang, Z. Zhang, P. Wang, *NPG Asia Mater.* 2012, 4, e8.
- [77] C. Zhou, Z. Chen, H. Yang, K. Hou, X. Zeng, Y. Zheng, J. Cheng, *ACS Appl. Mater. Interfaces* 2017, 9, 9184–9194.
- [78] J. Gu, P. Xiao, P. Chen, L. Zhang, H. Wang, L. Dai, L. Song, Y. Huang, J. Zhang, T. Chen, *ACS Appl. Mater. Interfaces* 2017, 9, 5968–5973.
- [79] Z. Xu, K. Miyazaki, T. Hori, *Appl. Surf. Sci.* 2016, 370, 243.
- [80] Z. Wang, G. Liu, S. Huang, *Angew. Chem. Int. Ed.* 2016, 6, 14610.
- [81] J. Li, L. Yan, Y. Zhao, F. Zha, Q. Wang, Z. Lei, *Phys. Chem. Chem. Phys.* 2015, 17, 6451.

- [82] K. Li, X. Zeng, H. Li, X. Lai, H. Xie, *Mater. Lett.* 2014, *120*, 255.
- [83] F. Liu, M. Ma, D. Zang, Z. Gao, C. Wang, *Carbohydr. Polym.* 2014, *103*, 480.
- [84] W. Liang, Z. Guo, *RSC Adv.* 2013, *3*, 16469.
- [85] C.-H. Xue, P.-T. Ji, P. Zhang, Y.-R. Li, S.-T. Jia, *Appl. Surf. Sci.* 2013, *284*, 464.
- [86] X. Tang, Y. Si, J. Ge, B. Ding, L. Liu, G. Zheng, W. Luo, J. Yu, *Nanoscale* 2013, *5*, 11657.
- [87] K. Chen, S. Zhou, L. Wu, *ACS Nano* 2016, *10*, 1386–1394.
- [88] C. Teng, D. Xie, J. Wang, Y. Zhu, L. Jiang, *J. Mater. Chem. A* 2016, *4*, 12884.
- [89] W. Zhang, Y. Zhu, X. Liu, D. Wang, J. Li, L. Jiang, J. Jin, *Angew. Chem. Int. Ed.* 2014, *53*, 856.
- [90] L. Zhang, Y. Zhong, D. Cha, P. Wang, *Sci. Rep.* 2013, *3*:2326, 1.
- [91] Z. Xue, S. Wang, L. Lin, L. Chen, M. Liu, L. Feng, L. Jiang, *Adv. Mater.* 2011, *23*, 4270.
- [92] J. Feng, M. Sun, Y. Ye, *J. Mater. Chem. A* 2017, *5*, 14990.
- [93] X. Wei, F. Chen, H. Wang, H. Zhou, Z. Ji, T. Lin, *J. Mater. Chem. A* 2018, *6*, 871.
- [94] P. S. Brown, B. Bhushan, *Sci. Rep.* 2015, *5*:14030, 1.
- [95] B. Li, J. Zhang, Z. Gao, Q. Wei, *J. Mater. Chem. A* 2015, *4*, 953.
- [96] K. Rohrbach, Y. Li, H. Zhu, Z. Liu, J. Dai, J. Andreasen, L. Hu, *Chem. Commun.* 2014, *50*, 13296.
- [97] A. K. Kota, G. Kwon, W. Choi, J. M. Mabry, A. Tuteja, *Nat. Commun.* 2012, *3*, 1025.
- [98] J. Yang, Z. Zhang, X. Xu, X. Zhu, X. Men, X. Zhou, *J. Mater. Chem.* 2012, *22*, 2834.
- [99] Q. Zhu, Q. Pan, *ACS Nano* 2014, *8*, 1402.
- [100] G. Kwon, A. K. Kota, Y. Li, A. Sohani, J. M. Mabry, A. Tuteja, *Adv. Mater.* 2012, *24*, 3666.
- [101] Z. Lei, Y. Deng, C. Wang, *J. Mater. Chem. A* 2018, *00*, 1.
- [102] L. Lv, T. Cui, B. Zhang, H. Wang, X. Li, J. Chen, *Angew. Chem.* 2015, *127*, 15380.
- [103] L. Zhang, J. Gu, L. Song, L. Chen, Y. Huang, J. Zhang, T. Chen, *J. Mater. Chem. A* 2016, *4*, 10810.

- [104] M. J. Hajipour, K. M. Fromm, A. Akbar Ashkarran, D. Jimenez de Aberasturi, I. R. de Larramendi, T. Rojo, V. Serpooshan, W. J. Parak, M. Mahmoudi, *Trends Biotechnol.* 2012, 30, 499.
- [105] L. Tamayo, M. Azócar, M. Kogan, A. Riveros, M. Páez, *Mater. Sci. Eng. C* 2016, 69, 1391.
- [106] X. Deng, A. Yu Nikiforov, T. Coenye, P. Cools, G. Aziz, R. Morent, N. De Geyter, C. Leys, *Sci. Rep.* 2015, 5, 10138.
- [107] J. P. Ruparelia, A. K. Chatterjee, S. P. Dutttagupta, S. Mukherji, *Acta Biomater.* 2008, 4, 707.
- [108] O. Kylian, J. Kratochvíl, M. Petr, A. Kuzminova, D. Slavinska, H. Biederman, J. Beranová, *Funct. Mater. Lett.* 2017, 10, 1750029.
- [109] A. Kuzminova, J. Beranová, O. Polonskyi, A. Shelemin, O. Kylián, A. Choukourov, D. Slavínská, H. Biederman, *Surf. Coat. Technol.* 2016, 294, 225.
- [110] H. Haberland, M. Karrais, M. Mall, *Molecules* 1991, 415, 413.
- [111] N. Tomczak, K. E. J. Goh, *Scanning Probe Microscopy*, World Scientific, 2010.
- [112] K. Siegbahn, K. Edvarson, *Nucl. Phys.* 1956, 1, 137.
- [113] R. N. Wenzel, *Ind. Eng. Chem.* 1936, 28, 988.
- [114] A. B. D. Cassie, S. Baxte, *Trans. Faraday Soc.* 1944, 40, 546.
- [115] B. M. Liu, S. Wang, Z. Wei, Y. Song, L. Jiang, *Adv. Mater.* 2009, 21, 665.
- [116] J. Hanuš, T. Steinhartová, O. Kylián, J. Kousal, P. Malinský, A. Choukourov, A. Macková, H. Biederman, *Plasma Process. Polym.* 2016, 13, 879.
- [117] J. Zhao, E. Baibuz, J. Vernieres, P. Grammatikopoulos, V. Jansson, M. Nagel, S. Steinhauer, M. Sowwan, A. Kuronen, K. Nordlund, F. Djurabekova, *ACS Nano* 2016, 10, 4684–4694.
- [118] S. Gauter, F. Haase, P. Solař, O. Kylián, P. Kúš, A. Choukourov, H. Biederman, H. Kersten, *J. Appl. Phys.* 2018, 124, 073301.
- [119] J. Kousal, A. Shelemin, M. Schwartzkopf, O. Polonskyi, J. Hanuš, P. Solař, M. Vaidulych, D. Nikitin, P. Pleskunov, Z. Krtouš, T. Strunskus, F. Faupel, S. V. Roth, H. Biederman, A. Choukourov, *Nanoscale* 2018, 10, 18275.
- [120] J. Blažek, J. Kousal, H. Biederman, O. Kylián, J. Hanuš, D. Slavínská, *J. Phys. D. Appl. Phys.* 2015, 48.
- [121] J. Kousal, A. Kolpaková, A. Shelemin, P. Kudrna, M. Tichý, O. Kylián, J. Hanuš, A. Choukourov, H. Biederman, *Plasma Sources Sci. Technol.* 2017, 26,

0.

- [122] M. Bonitz, N. Horing, P. Ludwig, *Introduction to Complex Plasmas, Springer Series on Atomic, Optical, and Plasma Physics*, Springer Verlag GmbH, Heidelberg, Germany, 2010.
- [123] F. Baletto, R. Ferrando, *Rev. Mod. Phys.* 2005, 77, 371.
- [124] R. Werner, T. Höche, S. G. Mayr, *CrystEngComm* 2011, 13, 3046.
- [125] A. L. Itkin, E. G. Kolesnichenko, *Microscopic Theory of Condensation in Gases and Plasma*, World Scientific Publishing, Farrer Road, Singapore, 1997.
- [126] R. Andok, A. Benčurová, P. Hrkút, A. Konečnicková, L. Matay, P. Nemeč, J. Škriniarová, *J. Electr. Eng.* 2013, 64, 371.
- [127] D. Hegemann, U. Vohrer, C. Oehr, R. Riedel, *Surf. Coatings Technol.* 1999, 116–119, 1033.
- [128] M. R. Alexander, R. D. Short, F. R. Jones, W. Michaeli, C. J. Blomfield, *Appl. Surf. Sci.* 1999, 137, 179.
- [129] P. Solař, O. Polonskyi, A. Choukourov, A. Artemenko, J. Hanuš, H. Biederman, D. Slavínská, *Surf. Coat. Technol.* 2011, 205, 42.
- [130] A. Choukourov, P. Pleskunov, D. Nikitin, V. Titov, A. Shelemin, M. Vaidulych, A. Kuzminova, P. Solař, J. Hanuš, J. Kousal, O. Kylián, D. Slavínská, H. Biederman, *Beilstein J. Nanotechnol.* 2017, 8, 2002.
- [131] J. Li, D. Li, Y. Yang, J. Li, F. Zha, Z. Lei, *Green Chem.* 2016, 18, 541.
- [132] J. Kratochvíl, J. Štěrba, J. Lieskovská, H. Langhansová, A. Kuzminova, I. Khalakhan, O. Kylián, V. Straňák, *Mater. Lett.* 2018, 230, 96.
- [133] E. Ruiz-Trejo, *Solid State Ionics* 2002, 130, 313.
- [134] D. Medvedev, A. Demin, G. Vdovin, P. Tsiakaras, N. Danilov, O. Reznitskikh, *J. Eur. Ceram. Soc.* 2016, 36, 2795.
- [135] C. Artini, *J. Eur. Ceram. Soc.* 2017, 37, 427.
- [136] N. Okita, A. Higashide, M. Saito, H. Yamamura, *Procedia Eng.* 2012, 36, 2.

## List of Abbreviations

<b>AC</b>	Alternating current
<b>AFM</b>	Atomic Force Microscopy
<b>ATR</b>	Attenuated total reflectance
<b>BE</b>	Binding energy
<b>BSE</b>	Back-scattered electrons
<b>CFU</b>	Colony forming unit
<b>DC</b>	Direct current
<b>DLC</b>	Diamond-like carbon
<b>DR</b>	Deposition rate
<b>FAT</b>	Fixed analyzer transmission mode
<b>FTIR</b>	Fourier Transform Infra-Red Spectroscopy
<b>GAS</b>	Gas Aggregation Cluster Source
<b>HAS</b>	Hemispherical analyzer
<b>HMDSO</b>	Hexamethyldisiloxane
<b>IR</b>	Infra-Red Spectroscopy
<b>MF</b>	Magnetic field
<b>NPs</b>	Nanoparticles
<b>OES</b>	Optical emission spectroscopy
<b>PECVD</b>	Plasma enhanced chemical vapor deposition
<b>PP</b>	Plasma polymerization
<b>PTFE</b>	Polytetrafluoroethylene
<b>QCM</b>	Quartz crystal microbalance
<b>RF</b>	Radio frequency
<b>RIE</b>	Reactive ion etching
<b>RMS</b>	Root mean square
<b>SE</b>	Secondary electrons
<b>SEM</b>	Scanning electron microscopy
<b>TEM</b>	Transmission electron microscopy
<b>UHV</b>	Ultra-high vacuum
<b>UV-Vis</b>	Ultraviolet-visible spectroscopy
<b>WCA</b>	Water contact angle
<b>XPS</b>	X-ray photoelectron spectroscopy

## List of Publications

### *Reviewed international journals*

1. **M. Vaidulych**, J. Hanuš, J. Kousal, S. Kadlec, A. Marek, I. Khalakhan, A. Shelemin, P. Solař, A. Choukourov, O. Kylián, H. Biederman, *Effect of magnetic field on the formation of Cu nanoparticles during magnetron sputtering in the gas aggregation cluster source*, Plasma Process Polym., 2019, e1900133, <https://doi.org/10.1002/ppap.20190013310>
2. A. Shelemin, D. Nikitin, P. Pleskunov, **M. Vaidulych**, R. Tafiichuk, A. Choukourov, P. Kúš, P. Solař, A. Kuzminova, O. Kylián, H. Biederman, *Wetting on a-C:H coatings decorated with sub-micron structures*, Surface & Coatings Technology, 2019, 367, 165–172.
3. **M. Vaidulych**, A. Shelemin, J. Hanuš, I. Khalakhan, I. Krakovsky, P. Kočová, H. Mašková, J. Kratochvíl, P. Pleskunov, J. Štěrbá, O. Kylián, A. Choukourov, H. Biederman, *Superwetable antibacterial textiles for versatile oil/water separation*, Plasma Process Polym., 2019, 6:e1900003, [doi.org/10.1002/ppap.201900003](https://doi.org/10.1002/ppap.201900003).
4. J. Kousal, A. Shelemin, M. Schwartzkopf, O. Polonskyi, J. Hanuš, P. Solař, **M. Vaidulych**, D. Nikitin, P. Pleskunov, Z. Krtous, T. Strunskus, F. Faupel, S. V. Roth, H. Biederman, A. Choukourov, *Magnetron-sputtered copper nanoparticles: lost in gas aggregation and found by in situ X-ray scattering*, Nanoscale, 2018, 10, 18275.
5. O. Kylián, A. Kuzminova, **M. Vaidulych**, M. Cieslar, I. Khalakhan, J. Hanuš, A. Choukourov, D. Slavínská, H. Biederman, *Core@shell Cu/hydrocarbon plasma polymer nanoparticles prepared by gas aggregation cluster source followed by in-flight plasma polymer coating*, Plasma Process Pol., 2018, 15:e1700109.

6. R. Štefaníková, T. Kretková, A. Kuzminova, J. Hanuš, **M. Vaidulych**, O. Kylián, H. Biederman, *Influence of atmospheric pressure dielectric barrier discharge on wettability and drying of poly(ether-ether-ketone) foils*, Polym. Degrad. Stab., 2018, 150, 114-121.
7. J. Hanuš, **M. Vaidulych**, O. Kylián, A. Choukourov, J. Kousal, I. Khalakhan, M. Cieslar, P. Solar, H. Biederman, *Fabrication of Ni@Ti core-shell nanoparticles by modified gas aggregation source*, J. Phys. D. Appl. Phys., 2017, 50, 475307.
8. **M. Vaidulych**, J. Hanuš, T. Steinhartová, O. Kylián, A. Choukourov, J. Beranová, I. Khalakhan, H. Biederman, *Deposition of Ag/a-C:H nanocomposite films with Ag surface enrichment*, Plasma Process Pol., 2017, 14, e1600256, <https://doi.org/10.1002/ppap.201600256>.
9. A. Choukourov, P. Pleskunov, D. Nikitin, V. Titov, A. Shelemin, **M. Vaidulych**, A. Kuzminova, P. Solar, J. Hanuš, J. Kousal, O. Kylián, D. Slavinska, H. Biederman, *Advances and challenges in the field of plasma polymer nanoparticles*, Beilstein J. Nanotechnol., 2017, 8, 2002-2014
10. O. Kylián, A. Shelemin, P. Solar, A. Choukourov, J. Hanus, **M. Vaidulych**, A. Kuzminova, H. Biederman, *Plasma polymers: From thin films to nanocolumnar coatings*, Thin Solid Films, 2017, 630, 86-91.
11. A. Choukourov, O. Kylián, M. Petr, **M. Vaidulych**, D. Nikitin, J. Hanuš, A. Artemenko, A. Shelemin, I. Gordeev, Z. Kolska, P. Solar, I. Khalakhan, A. Ryabov, J. Majek, D. Slavinska, H. Biederman, *RMS roughness-independent tuning of surface wettability by tailoring silver nanoparticles with a fluorocarbon plasma polymer*, NANOSCALE, 2017, 9, 2616-2625.
12. M. Petr, O. Kylian, J. Hanus, A. Kuzminova, **M. Vaidulych**, I. Khalakhan, A. Choukourov, D. Slavinska, H. Biederman, *Surfaces with roughness gradient and invariant surface chemistry produced by means of gas aggregation source and magnetron sputtering*, Plasma Process Pol., 2016, 13, 663–671.

13. A. Choukourov, I. Gordeev, J. Ponti, C. Uboldi, I. Melnichuk, **M. Vaidulych**, J. Kousal, D. Nikitin, L. Hanykova, I. Krakovsky, D. Slavinska, H. Biederman, Microphase-separated PE/ PEO thin films prepared by plasma-assisted vapor phase deposition, ACS Appl. Mater. Interfaces, 2016, 8, 8201-8212.

### ***Conference proceedings and other publications***

1. A. Shelemin, R. Perekrestov, **M. Vaidulych**, D. Nikitin, A. Choukourov, D. Slavinska, H. Biederman, *Formation of organosilicon nanoparticles in a gas aggregation source as witnessed by in situ light scattering*, NANOCON 2017 - Conference Proceedings, 2018, 937-941.
2. A. Shelemin, D. Nikitin, J. Kousal, **M. Vaidulych**, P. Pleskunov, A. Choukourov, D. Slavinska, H. Biederman, *Cycling instabilities in a gas aggregation cluster source used for plasma polymer nanoparticle fabrication*, NANOCON 2017 - Conference Proceedings, 2018, 765-770.
3. P. Solar, D. Nikitin, J. Hanus, O. Kylián, **M. Vaidulych**, M. Cieslar, H. Valentova, H. Biederman, *Production of heterogeneous copper-tungsten particles*, NANOCON 2017 - Conference Proceedings, 2018, 16-20.

### ***Conference contributions presented by author***

1. **M. Vaidulych**, A. Shelemin, J. Hanuš, I. Khalakhan, I. Krakovsky, P. Pleskunov, O. Kylián, A. Choukourov, H. Biederman, *Hydrocarbon plasma polymer particles for versatile oil/water separation*, MultiComp, Prague, Czech Republic, September 12-13, 2019.
2. **M. Vaidulych**, A. Shelemin, R. Perekrestov, D. Nikitin, A. Choukourov, D. Slavinska, H. Biederman, *Formation of Organosilicon Nanoparticles in a Gas Aggregation Source as Witnessed by In-situ Light Scattering*, NANOCON, Brno, Czech Republic, October 18-20, 2017.

3. **M. Vaidulych**, D. Nikitin, A. Choukourov, O. Kylián, J. Hanuš, P. Pleskunov, A. Shelemin, D. Slavinska, H. Biederman, *Hydrocarbon nanoparticle-based composite films with tailored morphology and wettability*, Baltic Polymer Symposium, Tallinn, Estonia, September 20-22, 2017.
4. **M. Vaidulych**, J. Hanuš, S. Kadlec, A. Marek, I. Khalakhan, P. Solař, O. Kylián, A. Choukourov, H. Biederman, *Magnetic field as an important parameter for the fabrication of Cu nanoparticles in a gas aggregation source*, 8th International Workshop on Polymer Metal Nanocomposites, Prague, Czech Republic, September 12-15, 2017.
5. **M. Vaidulych**, J. Hanuš, S. Kadlec, A. Marek, I. Khalakhan, O. Kylián, A. Choukourov, H. Biederman, *Effect of the magnetic field on formation of Cu nanoparticles during the magnetron sputtering in a gas aggregation source*, The International Conference on Phenomena in Ionized Gases, Estoril, Portugal, July 9-14, 2017.
6. **M. Vaidulych**, J. Hanuš, O. Kylián, A. Choukourov, I. Melnichuk, T. Steinhartová, H. Biederman, *Oxygen plasma etching of hard Ag/a-C:H nanocomposite coatings*, 15th International Conference on Plasma Surface Engineering, Garmisch-Partenkirchen, Germany, September 12-16, 2016.
7. **M. Vaidulych**, J. Hanuš, O. Kylián, A. Choukourov, T. Steinhartová, H. Biederman, *Investigation of hard Ag/a-C:H nanocomposite coatings produced by PECVD and gas aggregation source of nanoparticles*, 27th Symposium on Plasma Physics and Technology, Prague, Czech Republic, June 20-23, 2016.
8. **M. Vaidulych**, J. Hanus, O. Kylian, A. Choukourov and H. Biederman, *Production of metal/a-C:H nanocomposites*, 3rd Czech-German Workshop, Lübeck, Germany, May 19-20, 2016.